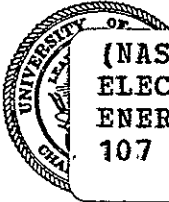


NGR-14-005-181



(NASA-CR-158646) A ROCKET-BORNE
ELECTROSTATIC ANALYZER FOR MEASUREMENT OF
ENERGETIC PARTICLE FLUX (Illinois Univ.)
107 p HC A06/MF A01

N79-24569

CSCI 04A

Unclas

G3/46

22315

AERONOMY REPORT NO. 82

A ROCKET-BORNE ELECTROSTATIC ANALYZER FOR MEASUREMENT OF ENERGETIC PARTICLE FLUX

by

M. A. Pozzi

L. G. Smith

H. D. Voss

February 1, 1979

Library of Congress ISSN 0568-0581



Supported by
National Aeronautics and Space Administration
Grant NGR 14-005-181

Aeronomy Laboratory
Department of Electrical Engineering
University of Illinois
Urbana, Illinois

CITATION POLICY

The material contained in this report is preliminary information circulated rapidly in the interest of prompt interchange of scientific information and may be later revised on publication in accepted aeronomic journals. It would therefore be appreciated if persons wishing to cite work contained herein would first contact the authors to ascertain if the relevant material is part of a paper published or in process.

A E R O N O M Y R E P O R T
N O. 82

A ROCKET-BORNE ELECTROSTATIC ANALYZER FOR
MEASUREMENT OF ENERGETIC PARTICLE FLUX

by

M. A. Pozzi
L. G. Smith
H. D. Voss

February 1, 1979

Supported by
National Aeronautics and
Space Administration
Grant NGR 14-005-181

Aeronomy Laboratory
Department of Electrical Engineering
University of Illinois
Urbana, Illinois

ABSTRACT

A rocket-borne electrostatic analyzer experiment is described. It is used to measure energetic particle flux (0.9 to 14 keV) in the nighttime midlatitude E region. Energetic particle precipitation there is believed to be a significant nighttime ionization source, particularly during times of high geomagnetic activity. The experiment has been designed for use in the payload of a Nike Apache sounding rocket.

The electrostatic analyzer employs two cylindrical parallel plates subtending a central angle of 90° . The voltage waveform supplied to the plates is a series of steps synchronized to the spin of the payload during flight. Both positive and negative voltages are provided, extending the detection capabilities of the instrument to both electrons and protons (and positive ions). Presented here is a detailed description of the development, construction and operation of the instrument together with a preliminary evaluation of its performance in a rocket flight.

	Page
ABSTRACT.	iii
TABLE OF CONTENTS	iv
LIST OF TABLES.	vi
LIST OF FIGURES	vii
1. INTRODUCTION.	1
2. THE MIDLATITUDE NIGHTTIME <i>E</i> REGION.	6
2.1 <i>Introduction</i>	6
2.2 <i>Dynamics of the Nighttime E Region</i>	6
2.3 <i>Nighttime Ionization Rates</i>	8
2.4 <i>Ionization Sources at Night.</i>	8
3. ENERGETIC PARTICLES IN THE NIGHTTIME <i>E</i> REGION	11
3.1 <i>Previous Observations.</i>	11
3.2 <i>Detectors for Low Energy Particles</i>	16
4. THE ELECTROSTATIC ANALYZER.	20
4.1 <i>Introduction</i>	20
4.2 <i>Theory of the Instrument</i>	20
4.3 <i>Deflection System.</i>	24
4.4 <i>Detection System</i>	26
4.5 <i>Instrument Configuration</i>	26
4.6 <i>Payload Instrumentation System</i>	36
5. ELECTRONIC CIRCUITS	37
5.1 <i>Plate Voltage Sweep Circuit.</i>	37
5.1.1 <i>Plate voltage power supplies.</i>	37
5.1.2 <i>Sweep waveform generator.</i>	42
5.1.3 <i>Clock and synchronization circuit</i>	46
5.1.4 <i>Sweep circuit performance</i>	49
5.2 <i>Electron Multiplier High Voltage Supply.</i>	51
5.3 <i>Preamplifier</i>	59
5.4 <i>Pulse Counting Circuit</i>	61
5.5 <i>Pulse-Height Analysis.</i>	66
6. INSTRUMENT CHARACTERIZATION AND CALIBRATION	70
6.1 <i>Introduction</i>	70
6.2 <i>Verification of System Operation</i>	70

	Page
6.3 <i>Angular Characteristics</i>	70
6.4 <i>Energy Resolution</i>	74
6.5 <i>Geometrical Factor</i>	78
6.6 <i>Pulse-Height Distributions</i>	87
7. SUMMARY, FLIGHT PERFORMANCE AND RECOMMENDATIONS FOR FUTURE WORK. . .	91
7.1 <i>Summary</i>	91
7.2 <i>Flight Performance</i>	91
7.3 <i>Recommendations for Future Work</i>	92
REFERENCES	95

LIST OF TABLES

Table		Page
4.1	Electron multiplier specifications.	28
5.1	Plate voltage power supplies specifications	39
5.2	Spin rates of Nike Apache rockets	47
5.3	A summary of the resistor value calculations.	50
5.4	A summary of the chosen resistor values and corresponding particle energies	52
5.5	High voltage dc-to-dc converter specifications.	57
5.6	Pulse preamplifier measured characteristics [<i>Paarmann and Smith,</i> 1977]	62
5.7	Telemetry channel characteristics	68
7.1	Listed are the dates, times and geomagnetic conditions for each of the eight sounding rockets launched as part of the JASPIC program. The duration of the program was from 3 June to 25 June 1978. K_{PR} is measured at Fredericksburg, Virginia; K_p is the planetary index	93

LIST OF FIGURES

Figure	Page
1.1 Placement of the electrostatic analyzer in the payload of Nike Apache 14.542 at the launch operations area of NASA's Wallops Flight Center. The payload was prepared for launch in June 1978 as part of the JASPIC program.	2
1.2 Nike Apache 14.543 poised and ready on its launcher at Wallops Island, June 1978	4
2.1 Profile 1 is representative of the daytime electron density (10^5 cm^{-3}). Towards night this electron density rapidly decays to a lower nighttime equilibrium level of 10^3 cm^{-3} (Profile 2). The nighttime density profile shows much variability and structure [<i>Voss and Smith, 1977</i>].	7
2.2 The ionization rates calculated from the intermediate layer electron-density profile show a strong correlation with magnetic activity (Index I). The particle energy flux shows a similar variation with magnetic activity [<i>Voss and Smith, 1979</i>]	9
3.1 Regions of high omnidirectional electron flux measured by <i>Seward</i> [1973] using a polar orbiting satellite (240-410 km altitude). These data clearly show two zones of midlatitude precipitation. Also shown on this map are <i>L</i> shells at 100 km corresponding to these zones ($L = 2.6$ and $L = 1.4$). Various rocket launch sites are indicated	12
3.2 The region in the Southern Hemisphere of intense particle precipitation is known as the South Atlantic anomaly. Low magnetic field values there reduce the mirroring heights of drifting energetic particles as they proceed around the earth	13
3.3 Log-log second-order least-squares fit of count rate versus energy for 10-km intervals above 100 km. The spectrum is approximately a power law [<i>Voss and Smith, 1977</i>].	14
3.4 Log-log plot of count rate versus energy for 100-km intervals above 100 km for Nike Apache 14.521. The spectrum is approximately power law [<i>Voss and Smith, 1977</i>].	15

Figure	Page
3.5 Sensitive energy range for various rocket-borne particle detection schemes. The energy comparison is made for electrons in the top half and for protons in the lower half.	17
4.1 Electrostatic analyzer block diagram	21
4.2 Edge-on view of the cylindrical parallel plates used for spectral analysis.	23
4.3 (a) Front view and (b) side view of the particle deflection system	25
4.4 The Johnston Laboratories model MM-1 open electron multiplier . . .	27
4.5 Longitudinal cross-section view of the MM-1 focused mesh multiplier [<i>Johnston Laboratories, Inc.</i> , Technical Data Application Note, JLI-605].. . . .	29
4.6 MM-1 multiplier gain as a function of the applied bias voltage for 600 eV input electrons. This curve was supplied by the manufacturer for the detector flown on Nike Apache 14.543 [<i>Johnston Laboratories, Inc.</i> , Technical Data Application Note, JLI-605 . . .	30
4.7 A view of the assembled electrostatic analyzer showing the electron multiplier housing and high voltage supply in the foreground and the collimator and deflection systems near the top. This instrument was flown on the payload of Nike Apache 14.543	31
4.8 A second view of the assembled electrostatic analyzer showing the two plate voltage supplies in the foreground and the plate voltage sweep circuit behind. To the left of the plate voltage supplies is the 15-pin connector through which all signals in or out of the instrument must pass	33
4.9 Payload integration for the electrostatic analyzer, the particle spectrometer and associated electronics and control systems for Nike Apaches 14.542 and 14.543. The propagation experiments and nose tip probe are located above the door release mechanism. Dimensions are given in inches	35
4.10 Disassembled payload of Nike Apache 14.542	36
5.1 Plate voltage sweep circuit -- generalized block diagram	38
5.2 Output voltage as a function of the input voltage for the Venus Q-30Z power supply (manufacturer's specified typical performance at 25°C) [<i>Venus Scientific, Inc.</i> product brochure]	40

Figure	Page
5.3 Plate voltage power supplies.	41
5.4 Power supply input voltage waveforms. Each division on the horizontal axis represents one cycle of the clock signal.	43
5.5 Sweep waveform generator. The waveforms of Figure 5.4 can be observed at points a and b.	45
5.6 Clock and synchronization circuit	48
5.7 A sketch of the analyzer plate voltage as a function of time (assuming a spin rate of 7 rps)	53
5.8 A photograph of the plate voltage monitor waveform.	54
5.9 Electrical connections to the MM-1 multiplier [<i>Johnston Laboratories, Inc.</i> , Technical Data Application Note, JLI-605]	55
5.10 MM-1 multiplier and associated high voltage electronics	58
5.11 Pulse preamplifier schematic diagram [<i>Paarmann and Smith</i> , 1977]	60
5.12 Pulse preamplifier input and output waveforms: (a) input: 20 ns/cm; (b) output: 1 V/cm, 20 ns/cm (input: 500 mV); (c) output: 1 V/cm, 50 ns/cm (input: 5 mV); (d) output: 0.5 V/cm, 50 ns/cm (input: 1.25 mV) [<i>Paarmann and Smith</i> , 1977].	63
5.13 Pulse preamplifier physical construction.	64
5.14 Pulse counting electronics [adapted from <i>Voss and Smith</i> , 1974].	65
5.15 Output signal supplied to telemetry from the pulse counting electronics. Each ramp represents 16 counts. The horizontal sweep rate is 10 ms/cm, yielding a count rate of approximately 55 counts per second [<i>Voss and Smith</i> , 1974]	67
6.1 The laboratory at Goddard Space Flight Center where the calibration experiments took place.	71
6.2 Pulse preamplifier input and output waveforms for protons of energy 3 keV [in (a) and (b)] and 10 keV [in (c) and (d)]. These photographs were taken during calibration tests at GSFC. The instrument was placed in a vacuum chamber and subjected to energetic particles from an accelerator	72
6.3 The electrostatic analyzer is shown here, without the collimator, mounted on a movable turntable inside the vacuum chamber. Visible on the right is the circular opening in the chamber wall through which energetic particles are introduced. The turntable together	

Figure	Page
with the analyzer can be rotated, making possible an angular scan of the instrument's response.	73
6.4 Electrostatic angular claiibrating using a monoenergetic 1 keV electror beam. Count rate is plotted as a function of the plate voltage monitor sor several different angles of incidence. Positive angles correspond to a clockwise rotation of the instru- ment as shown in Figure 6.3. An envelope curve (dashed line) has been drawn through the peaks of the angular scan curves. The collimator acceptance angle is 2.6° centered about 7°	75
6.5 Count rates as a function of plate voltage for several different monoenergetic proton beams. In all cases, the beam was incident along the axis of the collimator (i.e., slanted 7° with respect to the analyzer plates).	76
6.6 Energy resolution as a function of incident particle energy obtained from the curves of Figure 6.5	77
6.7 The normalized count rate is plotted as a function of plate voltage for several monoenergetic proton beams	78
6.8 Plate voltage for peak response as a function of incident particle energy obtained from the curves of Figure 6.5	80
6.9 A linear approximation to the cylindrical plate electrostatic analyzer. The actual instrument is shown in (a). Shown in (b) is the approximation, used in the calculation of the geometrical factor	82
6.10 The geometry used in the calculation of the solid look-angle. The actual dimensions are those of Figure 6.9(b)	83
6.11 Plots of the normalized multiplier (exit aperture) area il- luminated by a beam of particles incident through the collimator (entrance aperture) at an angle θ measured with respect to the collimator axis. (a) is a scan in the vertical plane (the bi- secting both analyzer plates) and (b) is a scan in the horizontal plane.	85
6.12 Illustrated is the calculation of the solid angle Ω subtended by the orthogonal angles α and β For sufficiently small values of α and β : $\Omega = \alpha\beta$, where α and β are in radians and Ω is in sterradians.	86

Figure	Page
6.13 Count rate as a function of pulse height for several different particle types. Data were taken over an equal time period for each type, and each was adjusted to the same energy (11 keV) and flux (2000 s^{-1}) levels. Both the vertical and horizontal scales are linear.	88
6.14 Count rate plotted on a log scale as a function of pulse height for H^+ and O^+ ions. These data are taken from Figure 6.13 . . .	89

1. INTRODUCTION

In early June 1978 the Soviet research ship "Professor Vize" appeared off the shore of northeastern Virginia at NASA's Wallops Flight Center. Russian scientists aboard the ship were preparing to participate with their American counterparts in a month-long series of coordinated experiments and observations. The joint U.S./U.S.S.R. mission had drawn scientists and experimenters from several parts of the world. Their purpose was to try and resolve widespread controversy within the international scientific community concerning the nature, and in some cases the very existence, of a nighttime ionization source in the earth's upper atmosphere at midlatitudes.

Previous observations cited in the literature had led to vastly differing conclusions, some supporting and some rejecting the existence of a nighttime corpuscular ionization source. These measurements had been made at different locations, at different times and with several different instruments. The purpose of the joint mission was to bring together the various factions in one place and at one time for experiments to resolve the apparent discrepancies.

Toward this end the group was preparing to launch a total of nine sounding rockets. Five of these were Soviet-built vehicles to be launched from the Professor Vize five miles offshore. NASA was to launch four sounding rocket vehicles from its launch operations area on Wallops Island. Complementing the rocket experiments were several ground-based and airborne measurements in addition to overhead satellite observations. The code name for the operation was JASPIC: Joint American-Soviet Particle Intercalibration Program.

Of the four American rocket payloads, two were designed and built by the Aeronomy Laboratory of the University of Illinois at Urbana-Champaign. The main objective of these two vehicles was a direct measurement of the energetic particle flux. Each payload contained, among other experiments, seven energetic particle detectors. One of these detectors, an electrostatic analyzer, was designed specifically to measure the lower energy portion (<12 keV) of the energetic particle spectrum. This report is a detailed description of the design and calibration of that instrument.

The electrostatic analyzer is shown in Figure 1.1 being mounted in the payload of Nike Apache 14.542. The payload is 6.5 inches (16.5 cm) in diameter, 83.1 inches (211.1 cm) in length including the nose cone, and weighs 72 pounds (33 kg). A detailed description of the payload instrumentation system is given in Section 4.6.

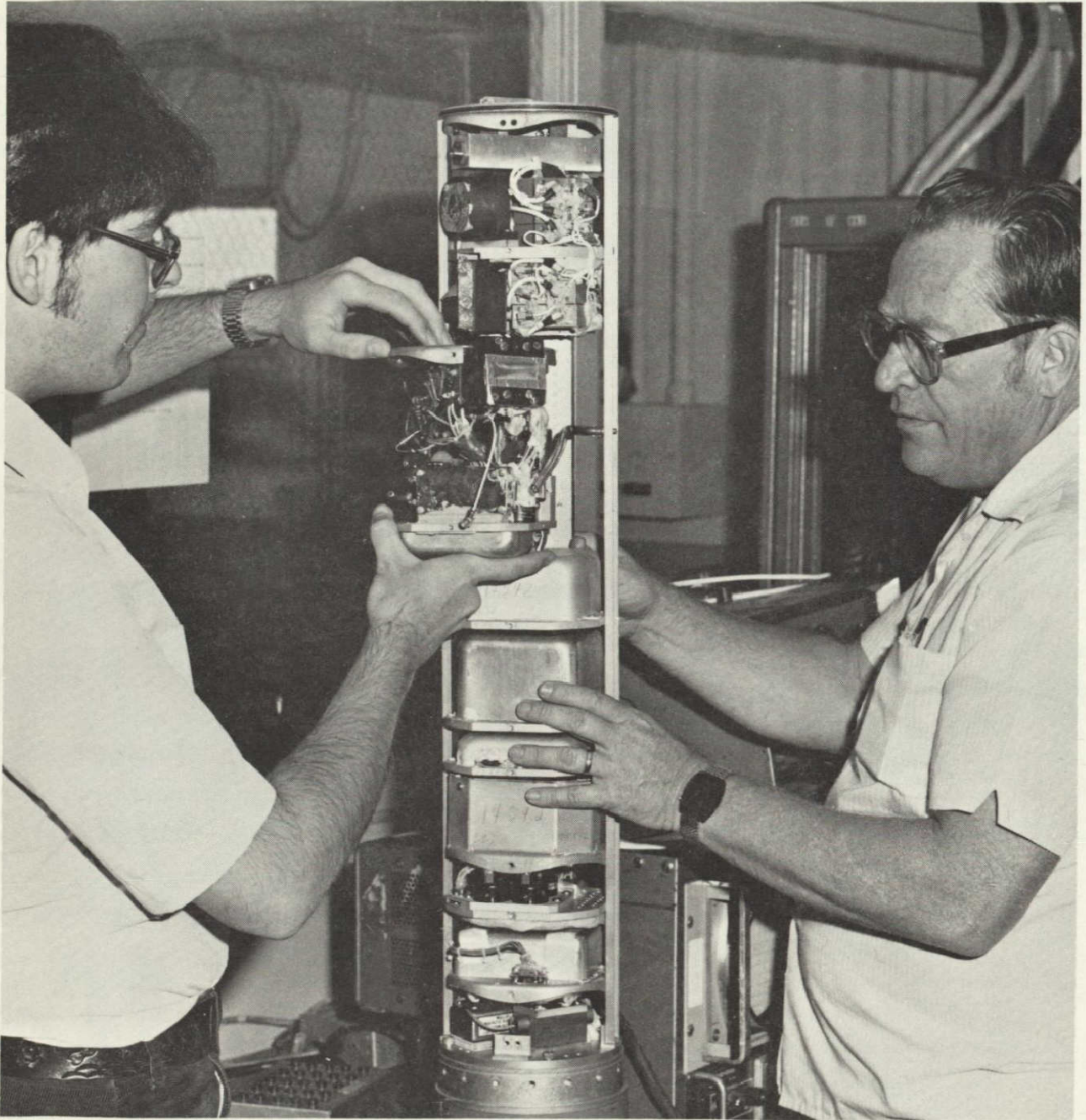


Figure 1.1 Placement of the electrostatic analyzer in the payload of Nike Apache 14.542 at the launch operations area of NASA's Wallops Flight Center. The payload was prepared for launch in June 1978 as part of the JASPIC program.

The Nike Apache is a two-stage sounding rocket designed to lift the payload to an altitude of approximately 180 km. Data from the rocket instruments are telemetered directly to ground receiving stations. After the flight the payload plunges into the ocean at a range of approximately 120 km and is not recovered. Figure 1.2 is a photograph of Nike Apache 14.543 on its launcher.

A description of the midlatitude nighttime E region (90-160 km) is given in Chapter 2. Basic differences which exist between the daytime and nighttime electron-density profiles are discussed along with a brief description of the dynamics responsible for the structure of the nighttime profiles. An argument is then presented supporting the existence of a nighttime source of ionization. A survey of possible ionization sources then leads to the conclusion that energetic particle flux precipitated from the earth's radiation belts may be present in significant quantities at midlatitudes.

In Chapter 3 a brief survey is made of previous experiments in which energetic particles have been observed. The need for a detector to measure the low energy portion of the energetic particle spectrum then becomes apparent. Also included is a summary of the various detector types which were considered to meet that need, leading ultimately to the electrostatic analyzer as the best choice.

The basic theory and operation of the electrostatic analyzer are explained in Chapter 4. A simplified block diagram of the instrument is presented along with a brief discussion of the physics upon which the operation of the instrument is based. Complete descriptions of the energetic particle deflection and detection systems are included. Also described are the mechanical configuration of the instrument and its relationship with other experiments also included in the Nike Apache payload.

Chapter 5 deals with the electronic circuits of the electrostatic analyzer. Described in detail are the plate voltage sweep system, electron multiplier high voltage supply, preamplifier and pulse counting circuits. Then mentioned briefly is the pulse-height analysis system which is part of the on-board data-processing electronics and which is used to extract further information from the electrostatic analyzer particle data.

Chapter 6 contains the characteristics of the completed instrument. The calibration experiments performed are described and the results are

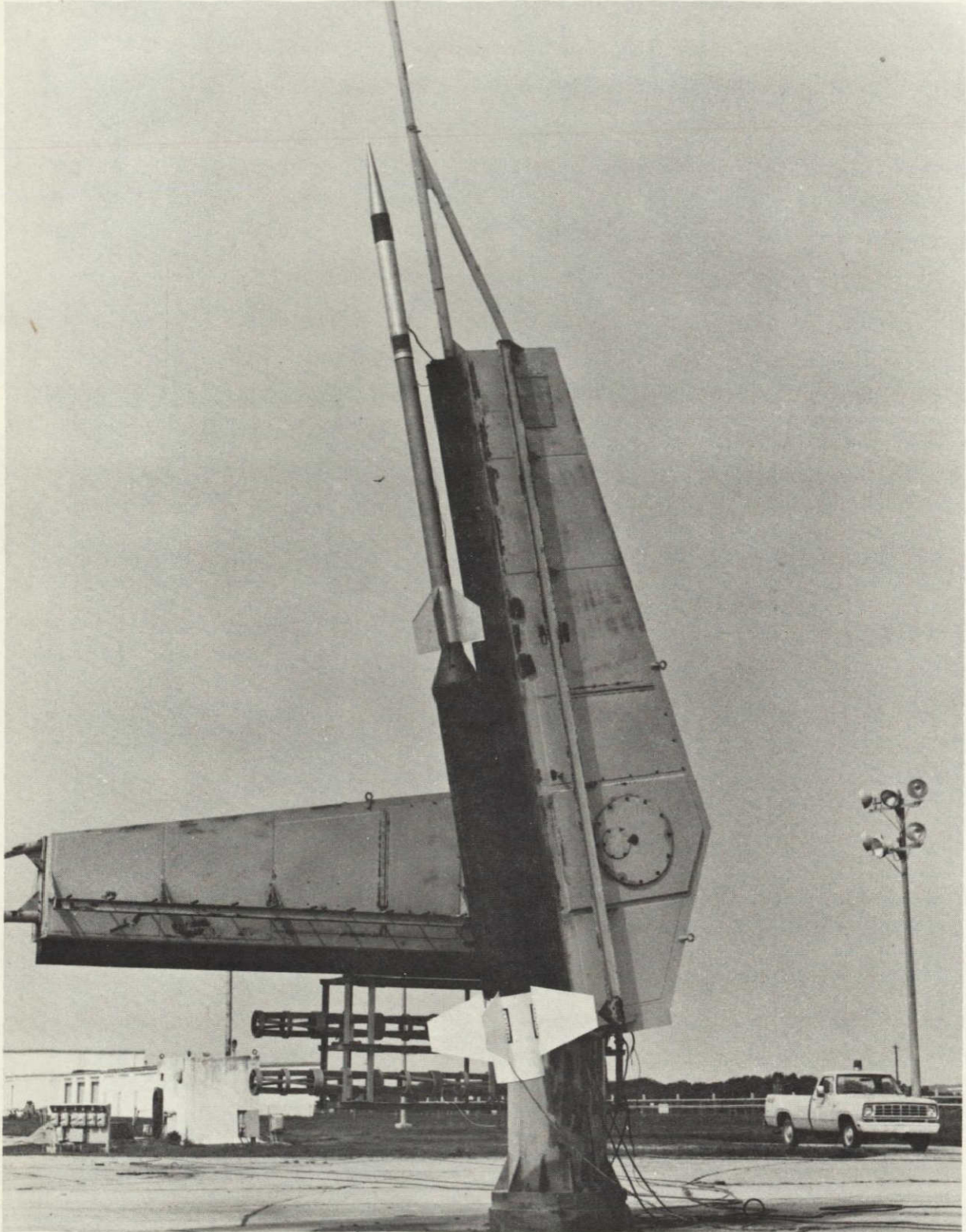


Figure 1.2 Nike Apache 14.543 poised and ready on its launcher at Wallops Island, June 1978.

summarized. The angular characteristics and energy resolution of the instrument are measured. From these results the geometrical factor of the analyzer is derived. Pulse-height distributions observed at the detector output for various energetic particle types are also presented. These calibration data when combined with data obtained from the actual rocket flights will yield valuable information concerning the absolute energetic particle flux and pitch-angle distribution.

The final chapter is a summary of the work done together with a preliminary evaluation of the instrument performance and some suggestions for future work.

2. THE MIDLATITUDE NIGHTTIME E REGION

2.1 *Introduction*

During the daytime the earth's upper atmosphere is subjected to intense solar radiation. This radiation is by far the dominant daytime ionization source, producing an electron density of about 10^5 cm^{-3} at altitudes from 100 to 200 km, as seen, for example, in profile 1 of Figure 2.1. Except for occasional sporadic- E layers (at 100 km in profile 1), the daytime electron-density profile at a given solar zenith angle remains nearly constant from day to day.

Each day after sunset the electron density in this region decays rapidly to a nighttime value of roughly 10^3 cm^{-3} , as illustrated by profile 2 of Figure 2.1. Nighttime electron-density profiles usually exhibit complex altitude structure and show much temporal variability. In addition to occasional intense sporadic- E layers (at 106 km in profile 2), a broad intermediate layer is often observed in the region from 120 to 200 km.

It will be seen later that the nighttime electron density is too large to be explained as a remnant of the daytime ionization (the loss rate by recombination is too large) and a nocturnal ionization source must be invoked.

The situation at night is complicated by the importance of transport processes which redistribute any existing ionization. These processes are unimportant during the daytime (except in sporadic- E layers) because of the short lifetimes of molecular ions (about 1 min), but at night they play an important role in determining the structure of the region between 100 and 200 km and lead to the formation of the intermediate layer.

In the next section the role of the transport processes in the nighttime E region is discussed briefly so that, in Section 2.3, the ionization rate itself can be considered.

For further discussion of the material presented here reference should be made to *Voss and Smith* [1977].

2.2 *Dynamics of the Nighttime E Region*

The neutral atmosphere interacts with the ionized component through collisions. The ions and electrons, because of the presence of the geomagnetic field, acquire velocity components perpendicular to that of the neutral wind. Thus, although the neutral winds are predominantly horizontal, the ions and electrons are transported vertically.

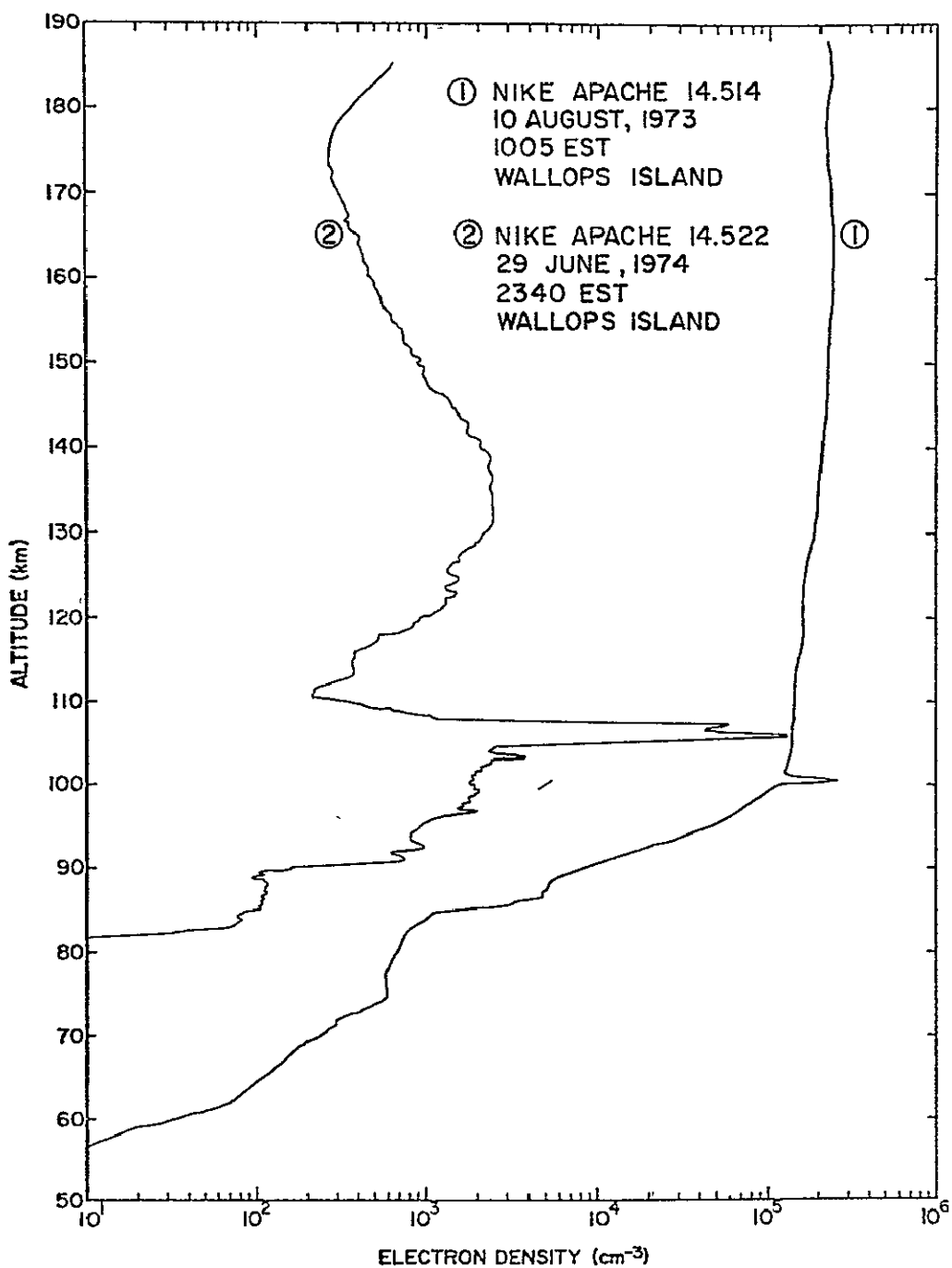


Figure 2.1 Profile 1 is representative of the daytime electron density (10^5 cm^{-3}). Towards night this electron density rapidly decays to a lower nighttime equilibrium level of 10^3 cm^{-3} (Profile 2). The nighttime density profile shows much variability and structure [Voss and Smith, 1977].

This Lorentz (or $\vec{v} \times \vec{B}$) force is important in the ionosphere above 90 km and gives rise to the phenomena of sporadic E and the intermediate layer. In these, shears (of appropriate direction) in the neutral wind cause ionization to converge forming a layer of enhanced electron density.

Further discussion of the role of winds in the formation of sporadic-E layers and of the intermediate layer may be found in, respectively, *Miller and Smith* [1978] and *Geller et al.* [1975].

2.3 Nighttime Ionization Rates

In order to calculate nighttime ionization rates from the measured electron-density profiles, vertical ion drift and diffusion processes must both be taken into account. The steady-state continuity equation for electrons in the E region is:

$$q - \alpha N^2 - \frac{d}{dz} (Nw) + \frac{d}{dz} D \left(\frac{dN}{dz} \right) = 0 \quad (2.1)$$

in which q is the ionization rate, α is the recombination coefficient, N is the electron density, w is the vertical ion drift velocity, D is the ambipolar diffusion coefficient and z is the altitude. The gravitational diffusion term is small and has been neglected.

Equation (2.1) can be solved by integrating between altitude points which are extrema of electron density. This choice of limits of integration makes it possible to average out the effects of vertical ion drift and diffusion. The details of this integration are outlined in *Smith et al.* [1974]. Although the procedure does not require a detailed knowledge of the drift and diffusion processes, they have not been neglected.

Ionization rates from the intermediate layer electron-density profile have been calculated using this method. The results using data obtained at Wallops Island are shown in Figure 2.2. Here the ionization rate is shown to be a strong function of magnetic activity as represented by the magnetic activity index I. The significance of this correlation will be discussed in the next section.

2.4 Ionization Sources at Night

In the absence of any nighttime source of ionization the concentration of molecular ions in the upper E region would decay, in about four hours after sunset, to a value of about 100 cm^{-3} . However, the observed electron density is usually about 10^3 cm^{-3} . Considerations, given in Section 2.3,

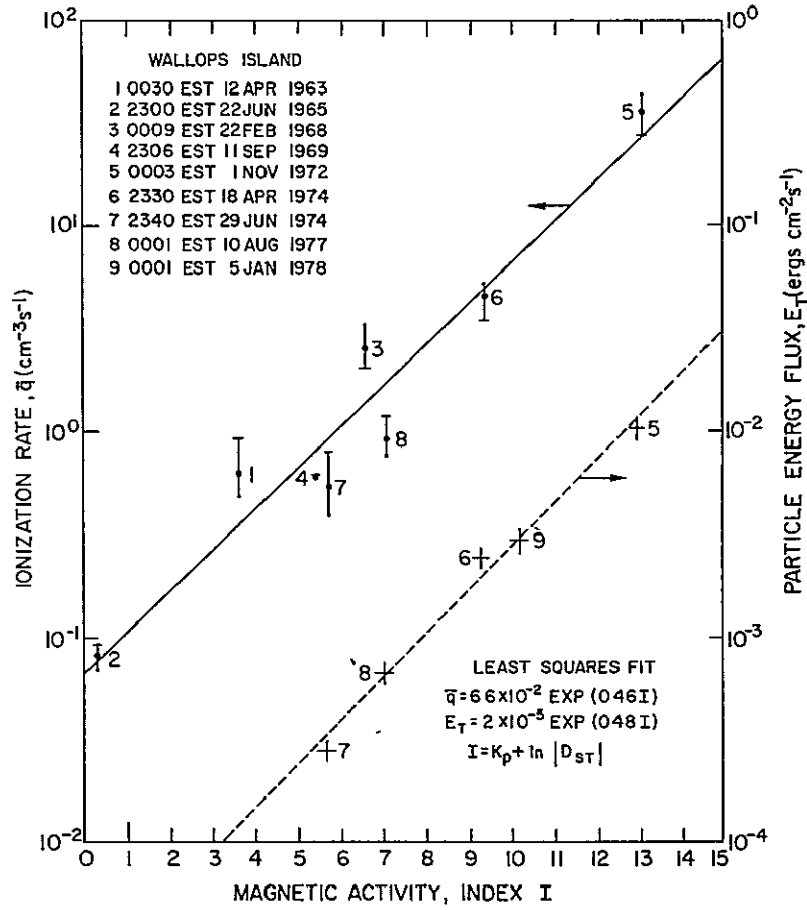


Figure 2.2 The ionization rates calculated from the intermediate layer electron-density profile show a strong correlation with magnetic activity (Index I). The particle energy flux shows a similar variation with magnetic activity [Voss and Smith, 1979].

of transport processes also provide evidence of a source of ionization. We now consider the nature of that source.

Nighttime ultraviolet radiation from the geocorona and of extraterrestrial origin can ionize atmospheric constituents in the region above 80 km and is partially responsible for the observed nighttime electron-density profiles. Detailed calculations of ionization rates caused by nighttime ultraviolet radiation have been developed by *Strobel et al.* [1974] based on the geocorona models of *Meier and Mange* [1973] and on experimental data. The nighttime electron-density profiles predicted by UV ionization sources using these calculations have been compared with densities actually observed by rocket flights at Wallops Island. These data suggest that in the region 90 to 110 km nighttime ultraviolet radiation is at a maximum and dominates as the ionization source. In the region above 120 km, however, measured electron densities are much higher than those predicted by the ultraviolet ionization model. Some other ionization source must be invoked to maintain the large electron densities observed in this region.

It has been noted earlier that a very strong correlation is found to exist between the nighttime ionization rate in the region 120 to 200 km and the magnetic activity. This suggests that energetic particles may be largely responsible for the high electron densities measured there. A least-squares fit to the data of Figure 2.2 is given by the experimental relationship:

$$q = 0.12 \exp (0.70 Kp) \quad (2.2)$$

The correlation coefficient for the seven observations is 0.94. Similar results have been obtained by *Gough and Collin* [1973] in which they measured the flux of energetic electrons (>40 keV) at South Uist on thirteen rocket flights. Their correlation with magnetic activity by a least-squares fit gives an exponent of (0.98 Kp) and a correlation coefficient of 0.79. The total particle energy flux, obtained from rocket data, is also plotted in Figure 2.2. and it, too, shows a strong correlation with magnetic activity. All of these observations point towards energetic particles precipitated from the radiation belts during periods of magnetic activity as the primary ionization source in the upper E region at night.

Further investigation of the nighttime energetic particle flux at midlatitudes is the motivation for the development of the instrument described in later chapters.

3. ENERGETIC PARTICLES IN THE NIGHTTIME *E* REGION

3.1 *Previous Observations*

Several observations of energetic particle flux at middle and low latitudes have been made, both directly and indirectly, in recent years. Of these measurements, the most direct are those involving rocket- or satellite-borne particle detectors. Rocket instruments in particular are capable of providing excellent height resolution, and spectral and pitch-angle information. A summary of observations which have been made to date is included in *Voss and Smith* [1977]. Only those experiments directly related to the present instrument development will be mentioned here.

Shown in Figures 3.1 and 3.2 are the first global maps of particle precipitation [*Seward*, 1973]. These measurements were made with a polar orbiting satellite on 18 and 19 September 1961 (K_p about 1) at altitudes of 240 to 410 km. The detector, a beryllium-coated cesium iodide scintillator, was sensitive to electrons with energy greater than 100 keV. Also shown in the figure are several launch sites from which rocket-borne particle observations have been made.

The most interesting features of the mapping are the roughly concentric bands of midlatitude energetic particle precipitation. The location of Wallops Island near the center of one of these bands makes it an ideal site from which to carry out rocket-borne particle precipitation experiments.

Three such particle observation experiments launched at Wallops Island will be mentioned here. The first two, Nike Apaches 14.520 and 14.521, both included a solid-state energetic particle detector, a Langmuir probe, a propagation experiment and a magnetometer. Nike Apache 14.520 was launched at 2330 EST on 18 April 1974 under moderately disturbed magnetic conditions ($K_p = 5+$). The count rate observed is plotted in Figure 3.3 as a function of particle energy for several different altitude ranges. Nike Apache 14.521 was launched several weeks later at 2120 EST on 29 June 1974 under less disturbed conditions ($K_p = 3+$). Figure 3.4 is a plot of the observed count rate versus particle energy for this flight. Note that the count rates are uniformly higher for the disturbed night, as would be expected. In addition, both spectra display approximate power law behavior, with increasing flux at lower energies.

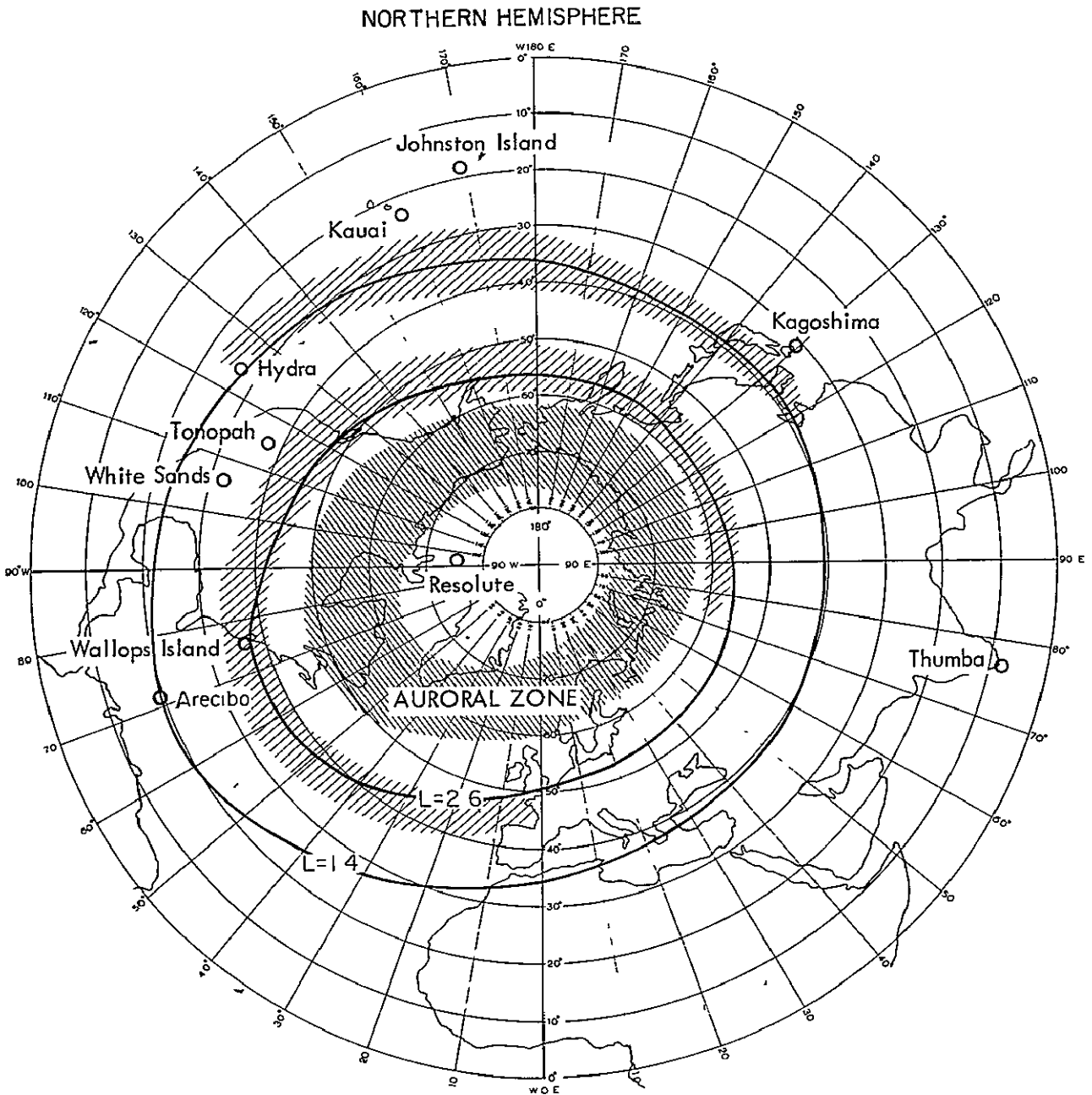


Figure 3.1 Regions of high omnidirectional electron flux measured by Seward [1973] using a polar orbiting satellite (240-410 km altitude). These data clearly show two zones of midlatitude precipitation. Also shown on this map are L shells at 100 km corresponding to these zones ($L = 2.6$ and $L = 1.4$). Various rocket launch sites are indicated.

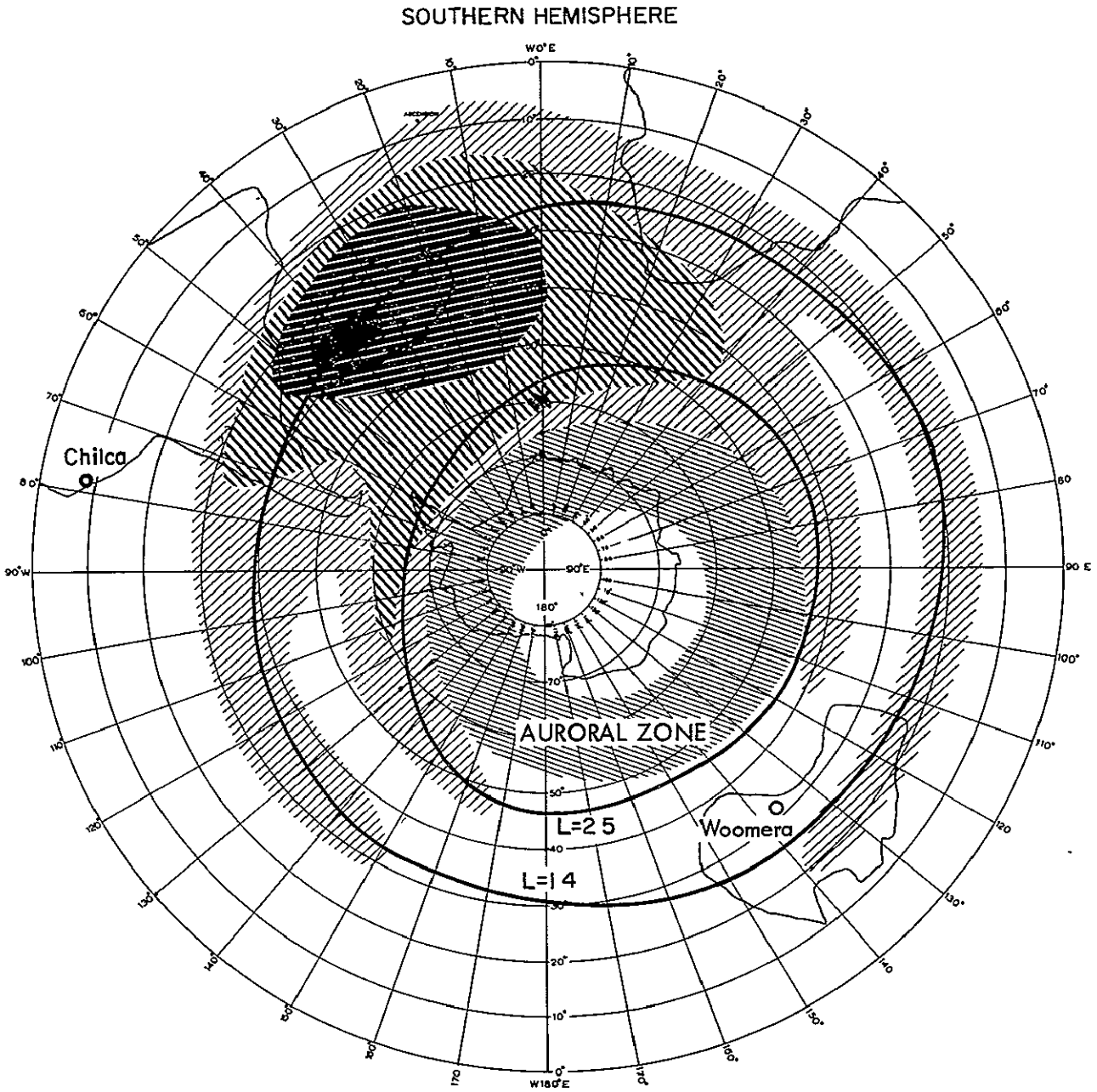


Figure 3.2 The region in the Southern Hemisphere of intense particle precipitation is known as the South Atlantic anomaly. Low magnetic field values there reduce the mirroring heights of drifting energetic particles as they proceed around the earth.

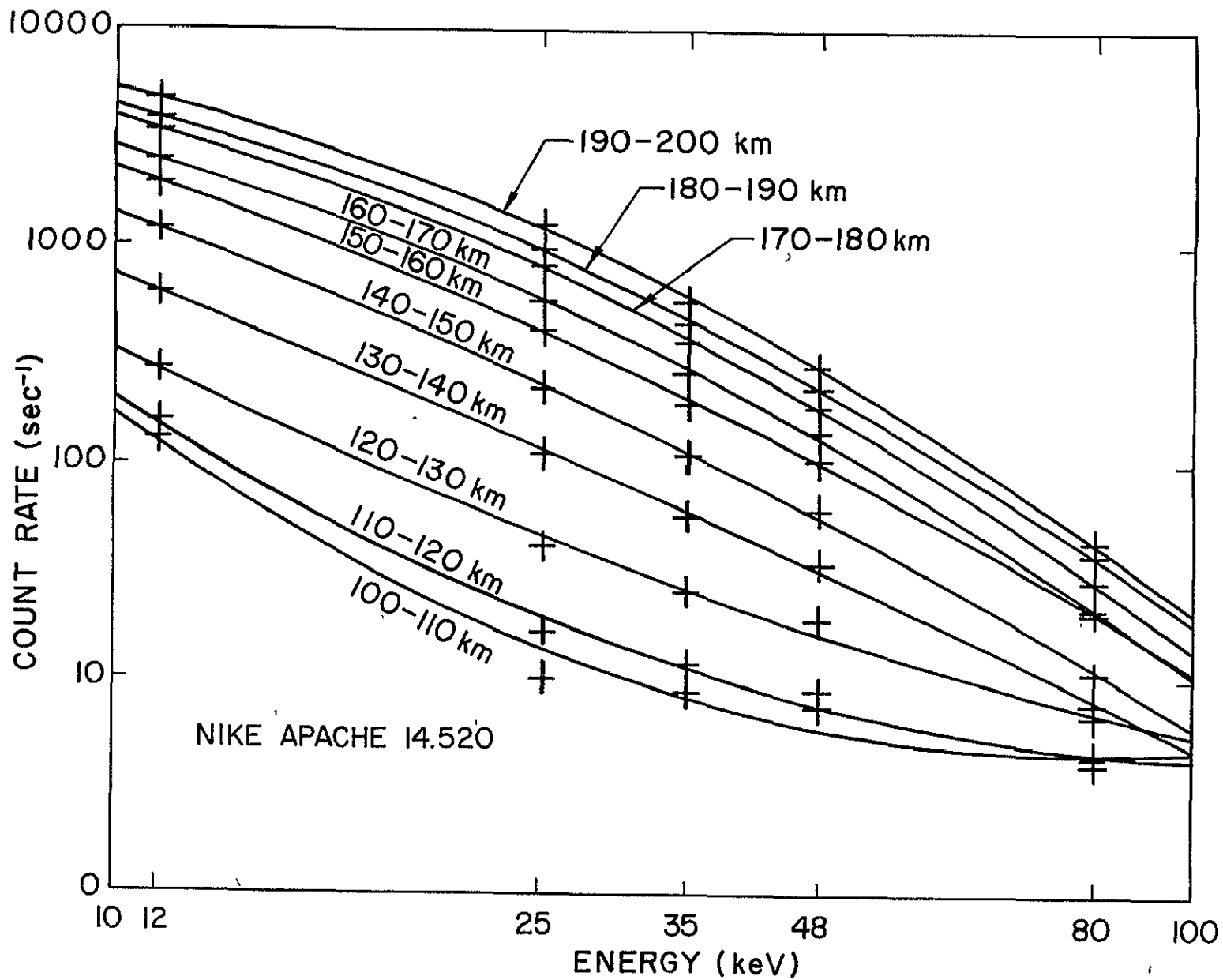


Figure 3.3 Log-log second-order least-squares fit of count rate versus energy for 10-km intervals above 100 km. The spectrum is approximately a power law [Voss and Smith, 1977].

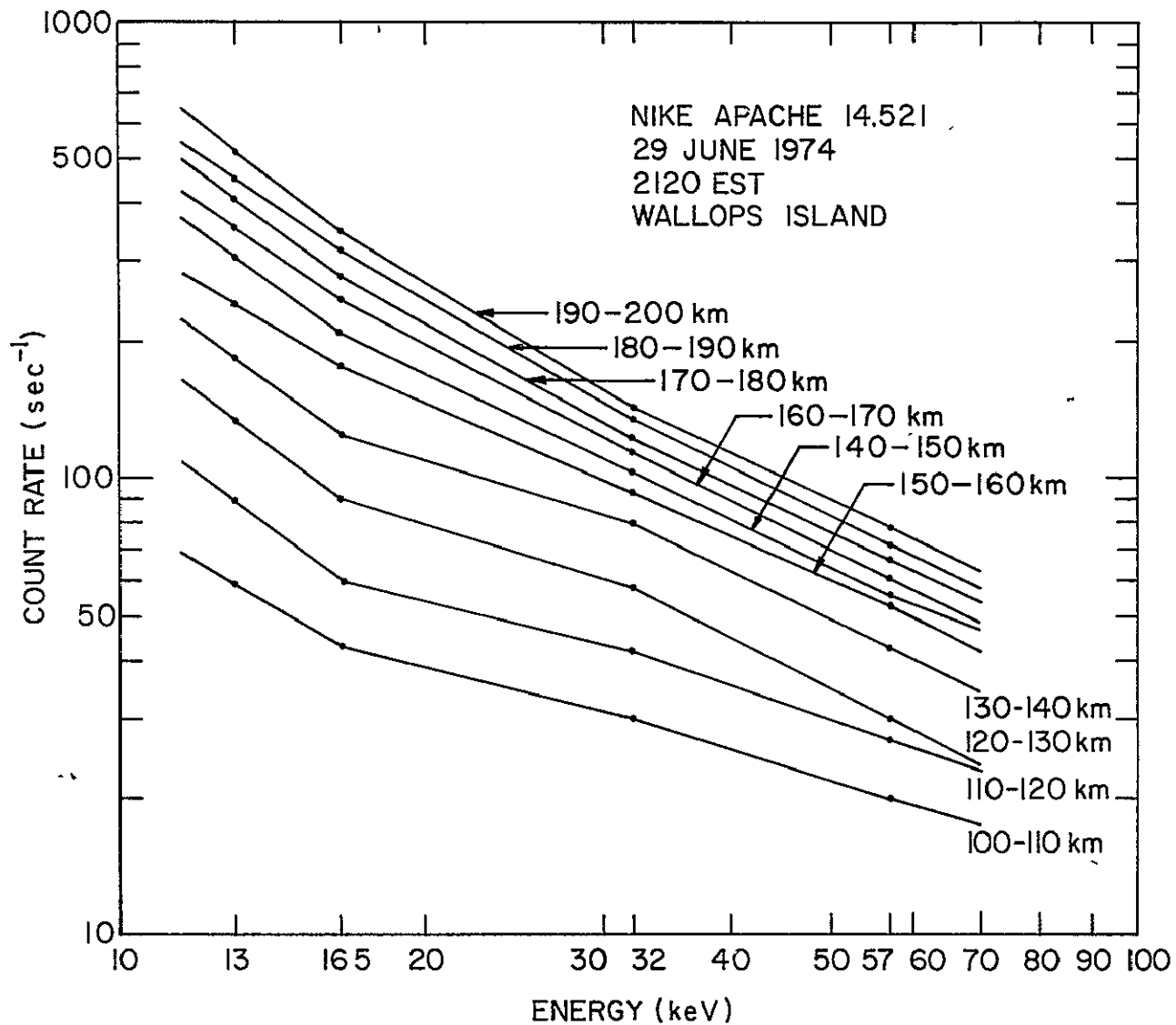


Figure 3.4 Log-log plot of count rate versus energy for 10-km intervals above 100 km for Nike Apache 14.521. The spectrum is approximately power law [Voss and Smith, 1977].

The solid-state detectors used in these experiments are insensitive to particles with energies less than about 12 keV so that no information was gained about the lower energy particles where large fluxes seem to be indicated. The calculation of ionization (or energy deposition) rates from the particle flux requires that the spectrum be extended to lower energies than the roughly 12 keV limit provided by the (uncooled) solid-state detectors. Extension of the energy range to about 500 eV is necessary if all particles penetrating below 200 km are to be measured. Thus the need arises for an experiment designed to measure the low energy (<12 keV) particle flux.

Nike Apache 14.533 was launched from Wallops Island at 0001 EST on 5 January 1978 also under moderately disturbed conditions ($K_p = 6-$). It included two energetic particle detectors and a 391.4 nm airglow photometer, as well as the Langmuir probe and propagation experiments. The solid-state detectors were the same as those from previous flights except that a "broom" magnet was placed in front of one of them, preventing electrons from reaching the detector. This detector was therefore sensitive only to protons and heavier particles.

Preliminary analysis of the data from Nike Apache 14.533 shows comparable fluxes of energetic particles in the two detectors, indicating that the particles, at least on that occasion, were mostly protons. This rather surprising result leads to the requirement that the low energy particle detector be designed to be sensitive to both electrons and protons, and that, if possible, it should be able to distinguish between the two.

3.2 *Detectors for Low Energy Particles*

Many types of particle detectors have been investigated for this particular application. The energy ranges of the principal types of detectors are shown in Figure 3.5. The solid-state energetic particle detectors as flown on Nike Apaches 14.520, 14.521 and 14.533 are incapable of detecting particles at the lower end of the energy spectrum. Even if cooled to liquid nitrogen temperatures, the noise level inherent in these surface-barrier type semiconductor detectors would preclude adequate resolution of the lower energy protons. Although the solid-state detector remains the best choice for particle energies greater than about 12 keV, a new detection scheme is needed to investigate particle flux at smaller energies.

PARTICLE DETECTOR ENERGY COMPARISON

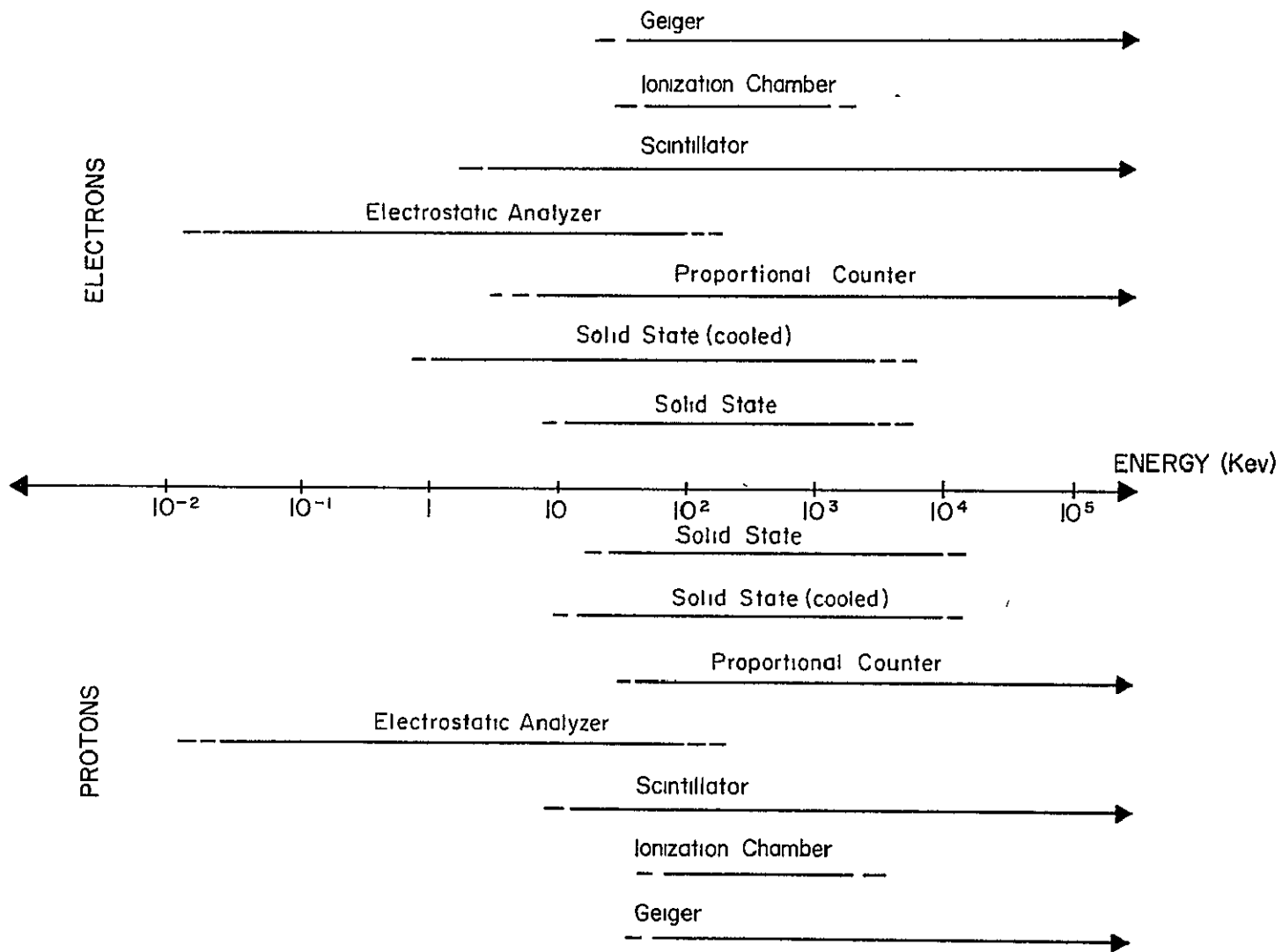


Figure 3.5 Sensitive energy range for various rocket-borne particle detection schemes. The energy comparison is made for electrons in the top half and for protons in the lower half.

One such scheme considered is that of a gaseous ionization detector. Gas detectors are classified into three modes of operation: ionization, proportional and Geiger. The collection process is based on the principle of the ionization of a gas by a charged particle in the presence of an electric field. The ions created are separated and accelerated by the field, yielding a current pulse at the detector output. If the field strength is small, there will be no secondary ionization and only the very small charge released by the decaying particle will be recorded. When used in an integrating mode, this device is called an ionization chamber. The proportional counter utilizes the multiplication of secondary electrons by applying a higher electric field strength. The number of secondaries formed, and the magnitude of the output charge pulse, will be proportional to the energy of the incident particle (for a fixed field strength). A still higher electric field strength will cause complete breakdown of the gas in the chamber, a process termed the "Geiger" mode.

The major drawback of the gas detectors is the choice of a window material thin enough to efficiently transmit low energy particles yet at the same time strong enough to withstand the large pressure differences encountered in a rocket flight. Although windows of $50 \mu\text{g}/\text{cm}^2$ polypropylene have been constructed to pass 5 to 8 keV electrons [Hayakawa *et al.*, 1973], passage of low energy protons would be impossible. In addition, Coulomb scattering and range straggling of the electrons cause large fluctuations in the amount of energy loss through the film, resulting in poor resolution.

The scintillation detector has also been considered. Energetic particles colliding with the lattice of a scintillator crystal cause excitation of electrons resulting in the release of photons. These small bursts of light (scintillations) are then detected with a photomultiplier. Although small, rugged and of simple construction, the scintillator is ruled out due mainly to its very poor resolution in the pulse counting mode. In addition, the efficiency of the best scintillation phosphors falls off sharply below 5 keV for electrons (higher for protons).

Clearly the best choice in this application is an electrostatic analyzer. The analyzer is an instrument consisting of two cylindrical parallel plates followed by an electron-multiplier detector. Spectral analysis of the incoming particle flux is accomplished by the electric field created in the

region between the analyzer plates. Although somewhat larger and more difficult to construct than the other detectors considered, the electrostatic analyzer offers excellent energy resolution (approximately 20% FWHM) over the entire spectral range of interest (0.5 to 12 keV) for both electrons and protons.

4. THE ELECTROSTATIC ANALYZER

4.1 *Introduction*

The electrostatic analyzer is an instrument designed to measure the energetic particle flux as a function of energy. Particles of a particular energy are selected by the analyzer and then counted by a detector, which in the present case is an electron multiplier. The selection is accomplished by applying an electric field perpendicular to the velocity vector of the particles. The particles execute a circular trajectory. With a suitable geometrical arrangement of the analyzer, namely uniformly curved plates, the energy of the particles that are accepted is proportional to the voltage difference applied to the analyzer. Particles of other energies execute trajectories which lead to collisions with the analyzer plates and consequent removal. By sweeping the voltage applied across the analyzer plates the desired range of particle energy can be examined and the flux determined as a function of energy.

Figure 4.1 is a block diagram of the electrostatic analyzer experiment. Particles enter through a collimator which defines the acceptance angle of the instrument. Grids are also included to prevent the internal electric fields of the instrument from affecting the vehicle potential and hence the Langmuir probe experiment. The particles then enter the analyzer and are deflected by the electric field generated by the voltage applied between the analyzer plates. Voltages of up to ± 3 kV are supplied to the plates by the plate voltage sweep circuits. Those particles of a selected energy determined by the plate voltage are deflected into the electron multiplier. A small negative charge pulse is fed from the multiplier to the preamplifier for each particle which strikes the multiplier. The output pulse of the preamplifier is sufficient to drive the pulse counting electronics, which assembles the count rate for telemetry to ground receiving stations. A fraction of the plate voltage is also telemetered back to the ground in order to monitor this voltage.

4.2 *Theory of the Instrument*

Consider a particle of velocity \vec{v} moving in a circular path of radius R . The particle acceleration (\vec{a}) is directed perpendicular to \vec{v} and has the magnitude

$$|\vec{a}| = \frac{|\vec{v}|^2}{R} \quad (4.1)$$

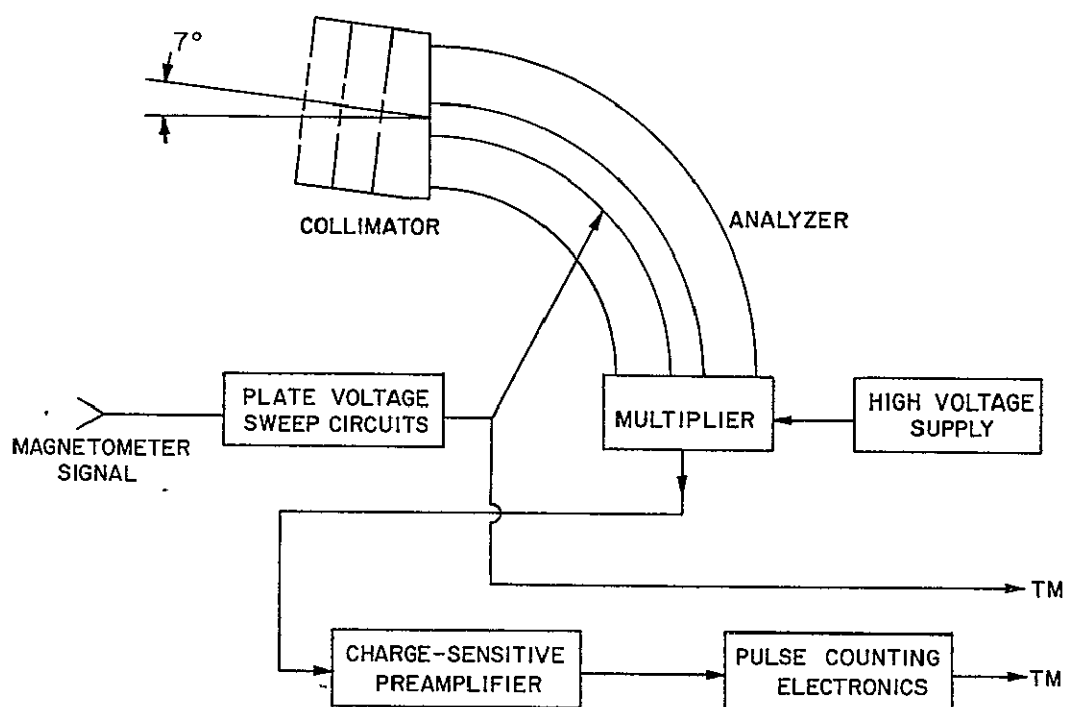


Figure 4.1 Electrostatic analyzer block diagram.

The kinetic energy of a particle of mass m is

$$U = \frac{1}{2} m |\vec{v}|^2 \quad (4.2)$$

Substituting for $|\vec{v}|^2$ from equation (4.1) gives

$$U = \frac{1}{2} m |\vec{a}| R \quad (4.3)$$

If, now, the acceleration is produced by a radially-directed electric field, \vec{E} , we have

$$m\vec{a} = q\vec{E} \quad (4.4)$$

where q is the particle charge. Thus equation (4.3) becomes

$$U = \frac{1}{2} q |\vec{E}| R \quad (4.5)$$

This shows that for a uniform, radially directed electric field, the particle moves in a circular trajectory with a radius proportional to its energy and inversely proportional to the magnitude of the electric field.

If the field is generated by applying a voltage V_p between two plates whose separation is d , then

$$|\vec{E}| = \frac{V_p}{d} \quad (4.6)$$

and equation (4.5) becomes

$$U = \left(\frac{R}{2d} \right) q V_p \quad (4.7)$$

or

$$[\text{Particle energy in eV}] = \left(\frac{R}{2d} \right) \cdot [\text{Plate voltage}] \quad (4.8)$$

The kinetic energy of an incoming particle traversing the analyzer will be directly proportional to the applied plate voltage. The constant of proportionality depends only on the plate separation and on the radius of curvature described by the particle path. It is independent of the mass of the particle.

A deflection system consisting of two cylindrical parallel plates is used, as shown in Figure 4.2. A voltage applied across these plates creates the electric field to deflect the incoming particles. For the field to be

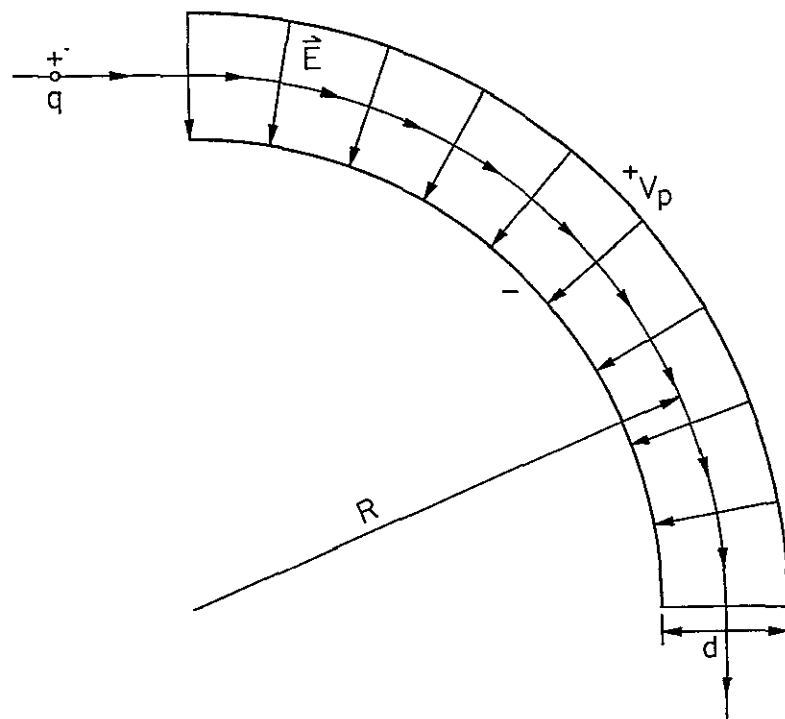


Figure 4.2 Edge-on view of the cylindrical parallel plates used for spectral analysis.

considered uniform, the radius of curvature R must be large compared with the plate separation distance, d . As the particle moves through the field region, \vec{E} remains perpendicular to \vec{v} .

For a given plate voltage, only particles with a particular energy, given by equation (4.7), are deflected through an arc of radius R . Others are deflected either too much or too little and collide with the plates. It is by this selectivity that spectral analysis of energetic particles is achieved. Resolution and sensitivity will be discussed in Chapter 6.

4.3 Deflection System

Figure 4.3 is a photograph of the particle deflection system used in this experiment. The radius of curvature R of the center of the analyzer channel is 7.5 cm. The channel subtends a central angle of 90° . Sawtooth ridges 0.1 cm deep along the inner faces of the plates impede reflective scattering of particles toward the detector. The effective plate separation (d), measured at half the depth of the ridges, is 0.83 cm. The plate width is 3.5 cm. The entire surface of the analyzer plates is black anodized to minimize scattering of UV radiation into the detector.

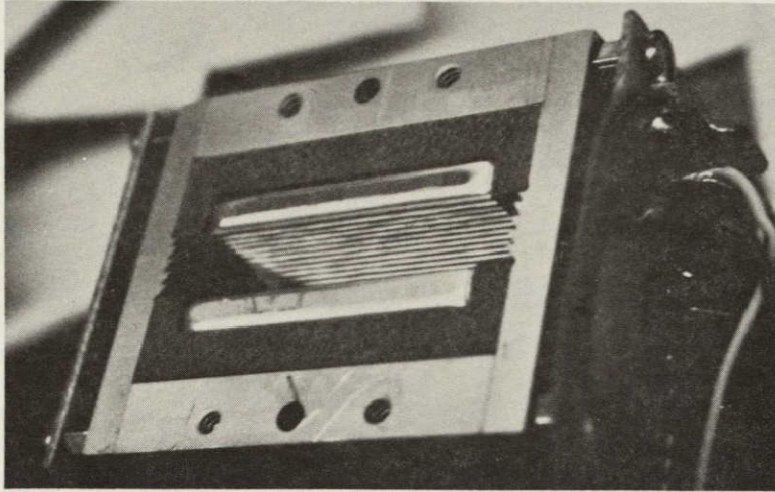
The look-angle of the detector is defined at the entrance aperture by a collimator. The collimator is tilted 7° upward from the horizontal. It is found experimentally (see Chapter 6) that the detector response is greatest for particles entering the analyzer aperture at this angle due to the focusing properties of the analyzer channel. The focusing effects of a radial electrostatic field on energetic particles are described in *Hughes and Rojansky* [1929].

Two thin-wire copper grids are also located within the collimator. The first is at -10 V in order to repel ambient electrons. The second is at ground potential to prevent outward fringing of the electric field.

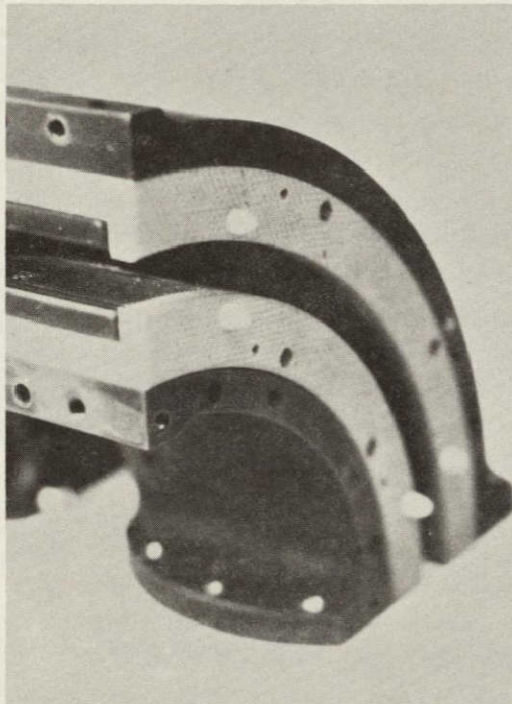
The exit aperture at the detector end of the analyzer channel is offset slightly from the center of the channel in the direction of the innermost plate. This is done in part to accommodate the focusing properties of the channel and in part to reduce the sensitivity of the instrument to scattered UV radiation, which is at a minimum closest to the innermost plate.

With the dimensions given above, the proportionality factor of equation (4.8) can be evaluated:

$$[\text{Particle Energy in eV}] = (4.52) [\text{Plate Voltage}] \quad (4.9)$$



(a)



(b)

Figure 4.3 (a) Front view and (b) side view of the particle deflection system.

4.4 *Detection System*

The detector, shown in Figure 4.4, is a large area electron multiplier model MM-1-5NG manufactured by Johnston Laboratories, Inc. of Cockeysville, Maryland. Specifications for the MM-1 are summarized in Table 4.1. It consists of a 20-stage secondary electron multiplier with activated copper-beryllium dynodes. Incoming particles strike the surface of the first dynode and generate secondary electrons. These secondary electrons are constrained by the electrostatic field to pass through the nearest hole in the dynode, Figure 4.5. They are then accelerated through the interdynode potential and strike the active surface of the second dynode, generating more secondary electrons. This process continues, with secondary electrons from each stage being focused and accelerated onto the succeeding dynode stage. After 20 stages of amplification, from 10^5 to 10^9 secondary electrons, depending on the bias voltage, leave the last dynode and strike the anode. A typical gain curve for the MM-1 as a function of the dc bias appears in Figure 4.6; the guaranteed minimum gain at 3500 V is 10^6 . Charge pulses collected at the anode are then amplified and counted.

A pressure of 10^{-4} torr or less is required for proper operation of the MM-1. At higher pressures an ion current can be generated by electron impact on the gas. Above 10^{-3} torr corona discharge becomes a problem. When used in rocket payloads the high voltage supply to the MM-1 is not turned on until the rocket is well up into the low pressure region (approximately 120 km).

The MM-1 is an open multiplier and therefore susceptible to a loss in gain through exposure to humid air or contaminating vapors. It is only slightly affected, however, by normal room atmosphere. After installation in the instrument and prior to launch, the multiplier casing is gently purged with dry nitrogen.

4.5 *Instrument Configuration*

A side view of the assembled electrostatic analyzer is shown in Figure 4.7. The particle entrance aperture and collimator are visible in the upper right-hand corner. Note that the collimator has been angled upward slightly with respect to the horizontal. The reasons for this tilt will be given in Chapter 6.

A circuit board containing the high voltage circuitry of the particle deflection system is attached to the side of the housing of the analyzer

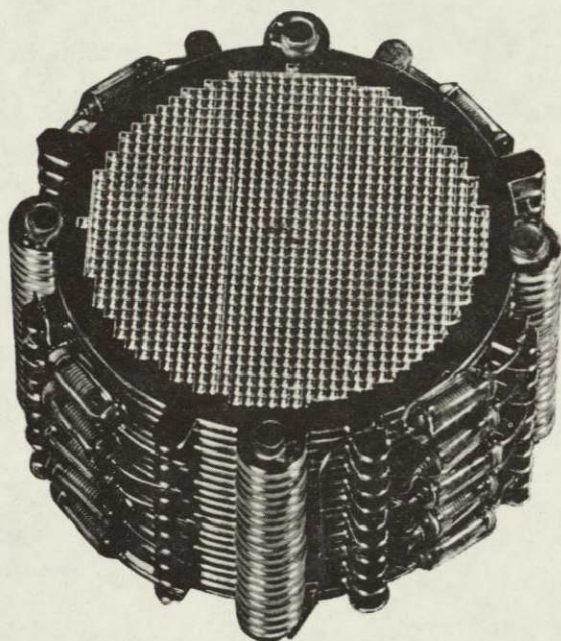


Figure 4.4 The Johnston Laboratories model MM-1 open electron multiplier.

Table 4.1

Electron multiplier specifications.

Model MM-1-5NG

Manufactured by Johnston Laboratories, Inc.

ELECTRICAL CHARACTERISTICS

Guaranteed Electron Gain:	10^6 at 3.5 kV
Delivered Typical Gain:	10^6 at 2.5 kV, 10^8 at 3.5 kV
Maximum Count Rate:	10^8 counts/second
Electron Detection Efficiency:	Greater than 90% at 200 eV
Ion Detection Efficiency:	Greater than 90% at 3000 eV
Dark Current:	Less than 10^{-13} amps at 10^6 gain
Noise:	Less than 1 count/minute at 10^7 gain
Output Rise Time:	Approximately 90% at 3 ns
Average Transit Time:	Approximately 25 ns
Dynode Resistors:	5 M Ω /stage
Maximum Operating Voltage:	5 kV (250 V/stage)
Maximum DC Anode Current:	5 μ A

PHYSICAL CHARACTERISTICS

Size:	2" dia. \times 1.35" long (5.1 cm dia. \times 3.4 cm long)
Weight:	3.6 oz. (100 gm)
Number of Stages:	20
Sensitive Area:	1.3" dia. (3.30 cm dia.) uniform across surface
Dynode Material:	activated copper-beryllium
Maximum Operating Pressure:	10^{-4} Torr

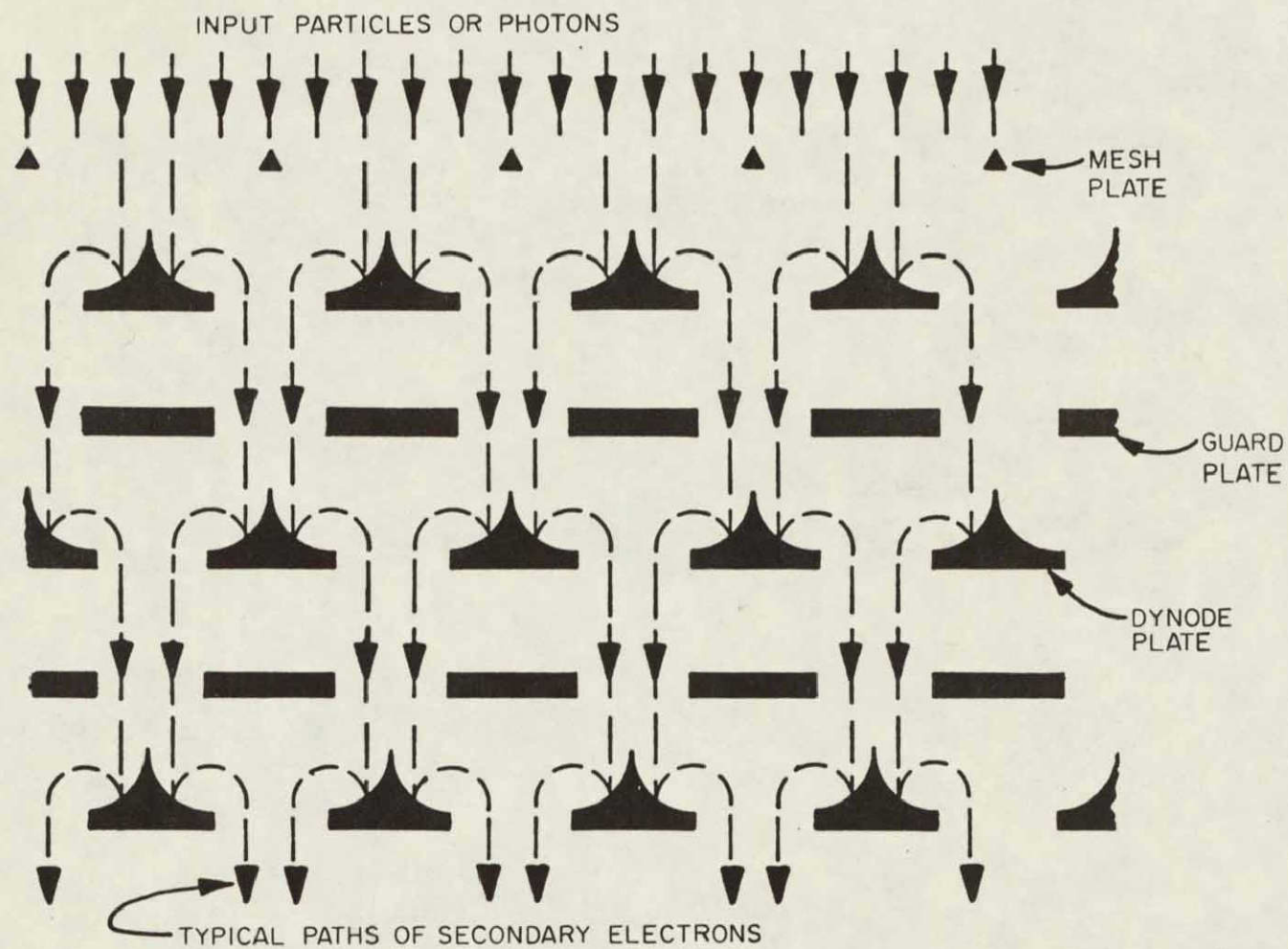


Figure 4.5 Longitudinal cross-section view of the MM-1 focused mesh multiplier [Johnston Laboratories, Inc., Technical Data Application Note JLI-605].

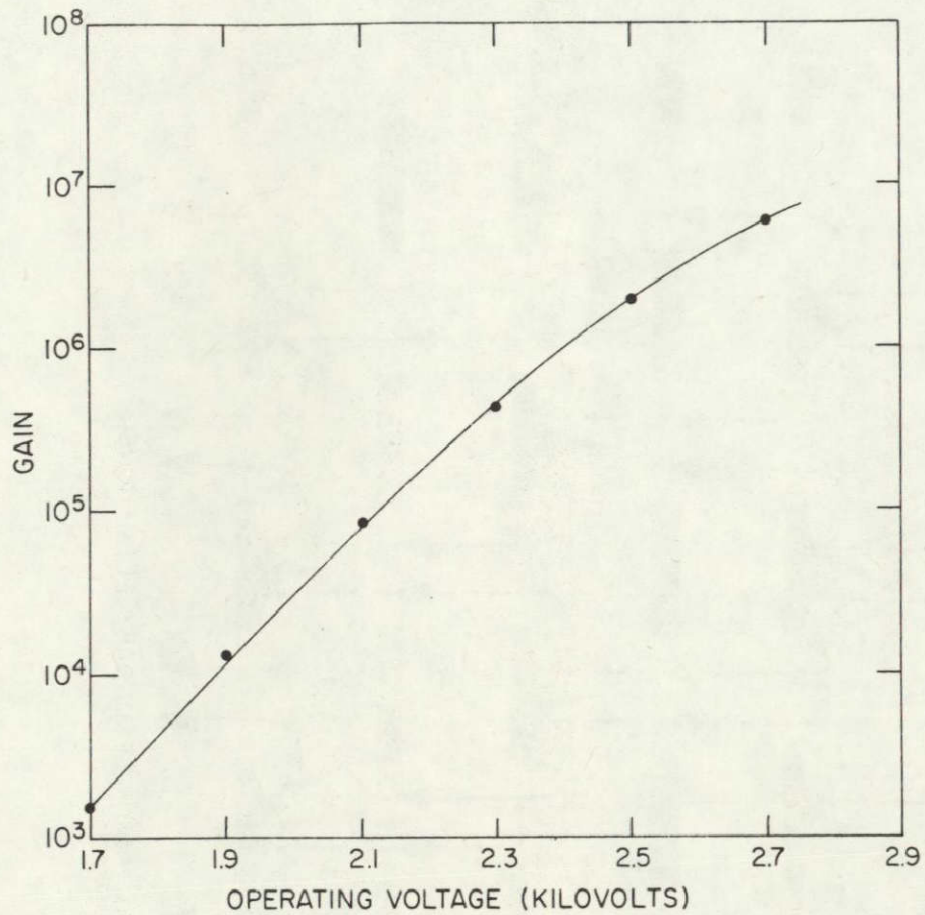


Figure 4.6 MM-1 multiplier gain as a function of the applied bias voltage for 600 eV input electrons. This curve was supplied by the manufacturer for the detector flown on Nike Apache 14.543 [*Johnston Laboratories, Inc.*, Technical Data Application Note JLI-605].

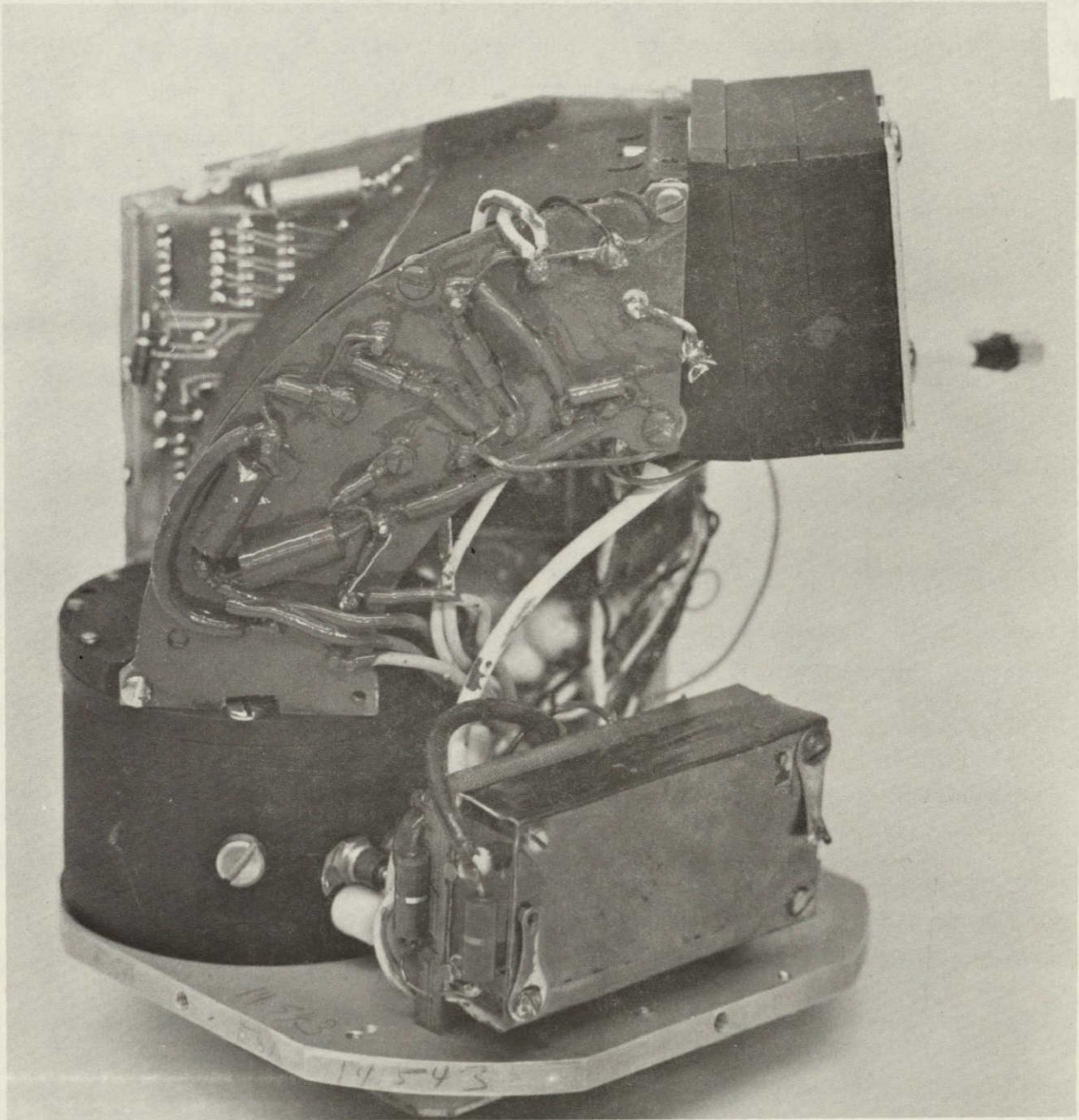


Figure 4.7 A view of the assembled electrostatic analyzer showing the electron multiplier housing and high voltage supply in the foreground and the collimator and deflection systems near the top. This instrument was flown on the payload of Nike Apache 14.543.

plates. Included there are the resistor-divider networks responsible for keeping the plate voltage symmetric about ground potential as well as providing a low-level plate voltage monitor signal. Wires attached to the lower right corner of the board provide the high voltages generated by a pair of dc-to-dc converters located on the opposite side of the instrument. Two screws visible in the center section of the board are attached directly to the plates. It is through this pair of terminals that the plate voltage is delivered. These screws are insulated from the outer housing of the deflection system. The entire high-voltage circuit board is coated with epoxy to minimize corona.

Visible at the lower left in Figure 4.7 is the cylindrical aluminum housing enclosing the MM-1 electron multiplier. It is attached to the base plate of the instrument by screws extending upward from underneath. The detector housing together with the entire particle deflection system have been black anodized.

Also attached directly to the base plate, to the right of the detector housing, is the high-voltage supply for the MM-1. The dc-to-dc converter, visible in the foreground, is wrapped in a magnetic shield. Mounted to the back of the converter is the high-voltage filter circuit of the supply. These circuits are also coated with epoxy to minimize corona.

The output signal from the electron multiplier is fed by coaxial cable through a hole in the base plate to the preamplifier mounted beneath that plate on the underside of the instrument.

Figure 4.8 is a photograph from the opposite side of the electrostatic analyzer. Visible in the center are the two high-voltage dc-to-dc converters for the analyzer plates. Directly behind these converters is the plate voltage sweep circuit. It is mounted on the side of the analyzer plate housing. The plate voltage sweep circuit is used to drive the converters. The circuit board has been coated with eccofoam and covered with an aluminum plate. The eccofoam helps to protect the components during the launch but is a poor thermal conductor. Mounted on the aluminum plate, which serves as a heat sink, are the +5-volt regulator (lower left corner) and the driver transistors (right side) of the plate voltage sweep circuit.

Just to the left of the plate voltage supplies is the 15-pin connector used to carry all signals in and out of the instrument. The connector attaches directly to the rail of the payload when the instrument is in place.

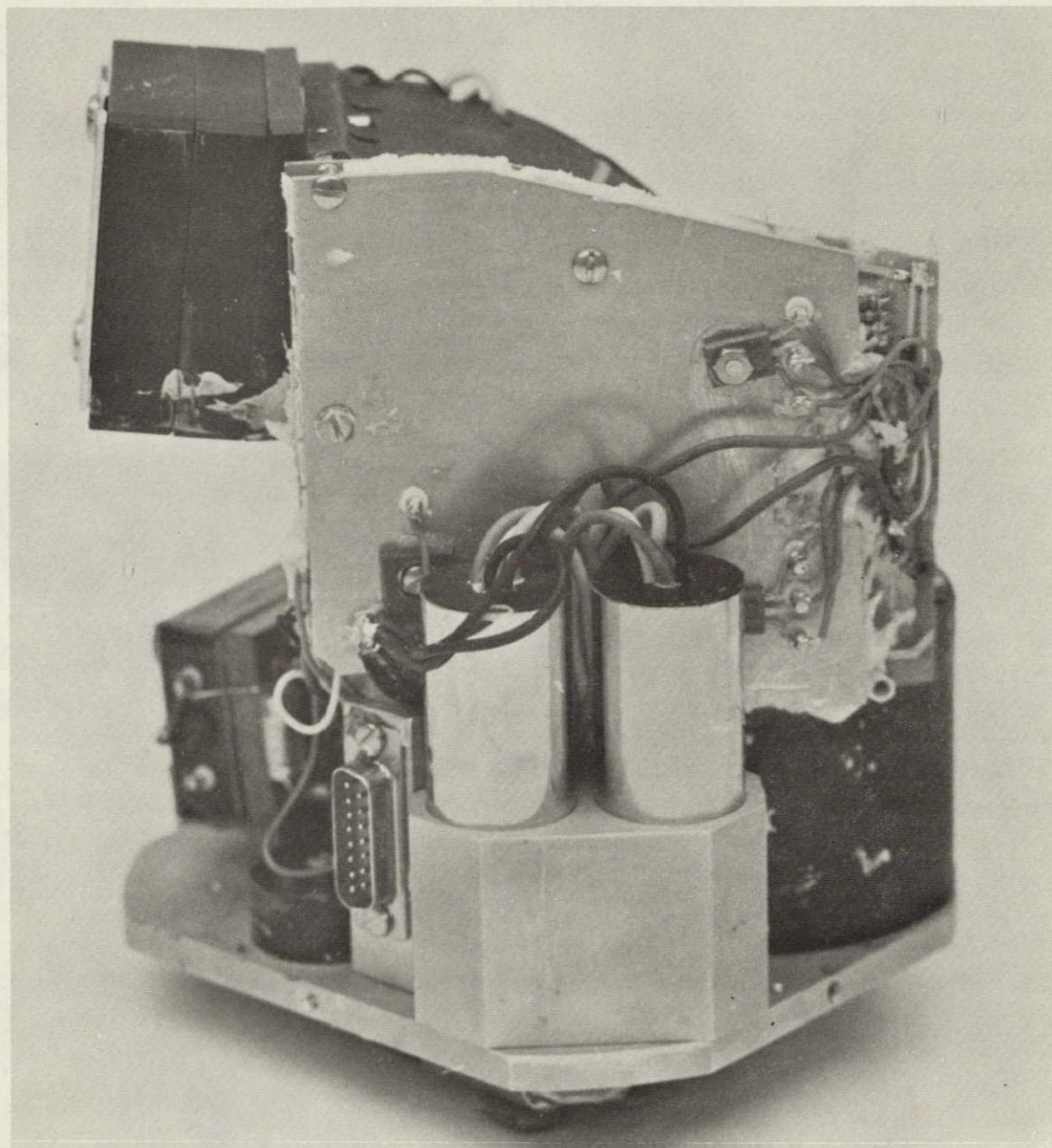


Figure 4.8 A second view of the assembled electrostatic analyzer showing the two plate voltage supplies in the foreground and the plate voltage sweep circuit behind. To the left of the plate voltage supplies is the 15-pin connector through which all signals in or out of the instrument must pass.

4.6 *Payload Instrumentation System*

The two payloads built for the JASPIC program are identical. The vehicles are Nike Apaches 14.542 and 14.543. Each payload contains six energetic particle spectrometers (EPS), an electrostatic analyzer (ESA), two propagation experiments for electron density and a Langmuir probe for electron density and electron temperature. Telemetry and antenna sections as well as timing, control and power decks and a magnetometer are also included. Data processing electronics for the EPS and ESA experiments include on-board pulse-height analyzer (PHA) and microprocessor systems.

The configuration of the part of the payload containing the particle-related experiments appears in Figure 4.9. The EPS experiment, consisting of six solid-state detectors, six preamplifiers and four pulse-shaping amplifiers, is located at the top of this section. The electrostatic analyzer is mounted directly beneath the EPS. Two doors on opposite sides of the payload cover areas 40.6 cm by 10.2 cm and conceal the entrance apertures of the EPS and ESA experiments. The doors are ejected 35 seconds after launch at an altitude of about 40 km by a timer-actuated pyrotechnic system.

Wires running down through the main rail of the payload feed signals from the detectors to data processing electronics in the lower enclosed section of the payload. The magnetometer, timing, control and power sections are also located there. Timing and control circuits are responsible for signal switching, door ejection and high voltage turn-on during flight.

Processed data are fed to a telemetry section located just below the portion of the payload shown in Figure 4.9. Included in that section are the 16 subcarrier VCO's and transmitting antenna of the 3W S-band FM/FM telemetry system.

Located above the detector portion of the payload is a fiberglass shell section enclosing the receivers of the propagation experiments. Mounted above this section is the nose cone with the ceramic-insulated steel probe tip of the Langmuir probe experiment. Figure 4.10 is a photograph of the disassembled payload of Nike Apache 14.542.

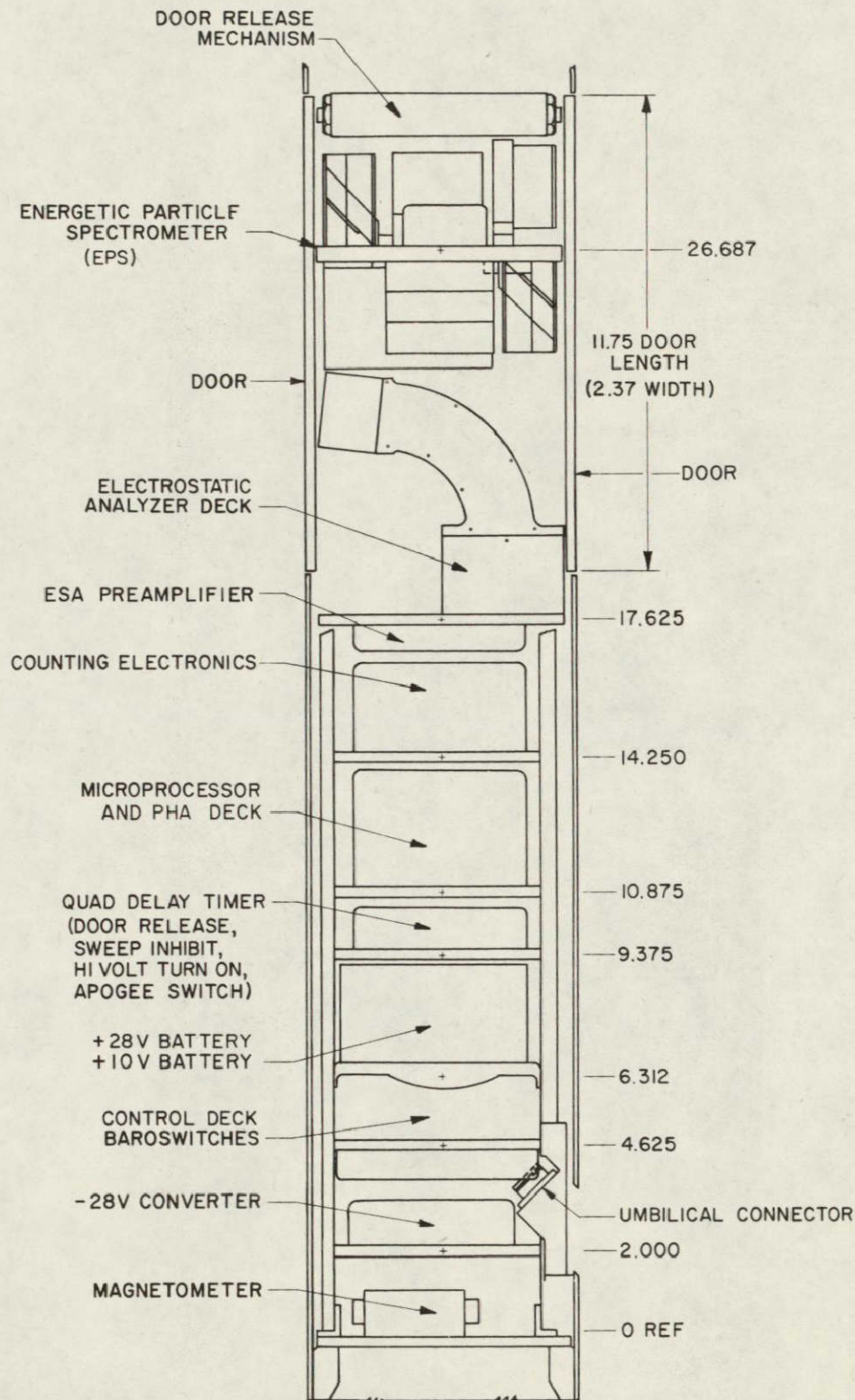


Figure 4.9 Payload integration for the electrostatic analyzer, the particle spectrometer and associated electronics and control systems for Nike Apaches 14.542 and 14.543. The propagation experiments and nose tip probe are located above the door release mechanism. Dimensions are given in inches.

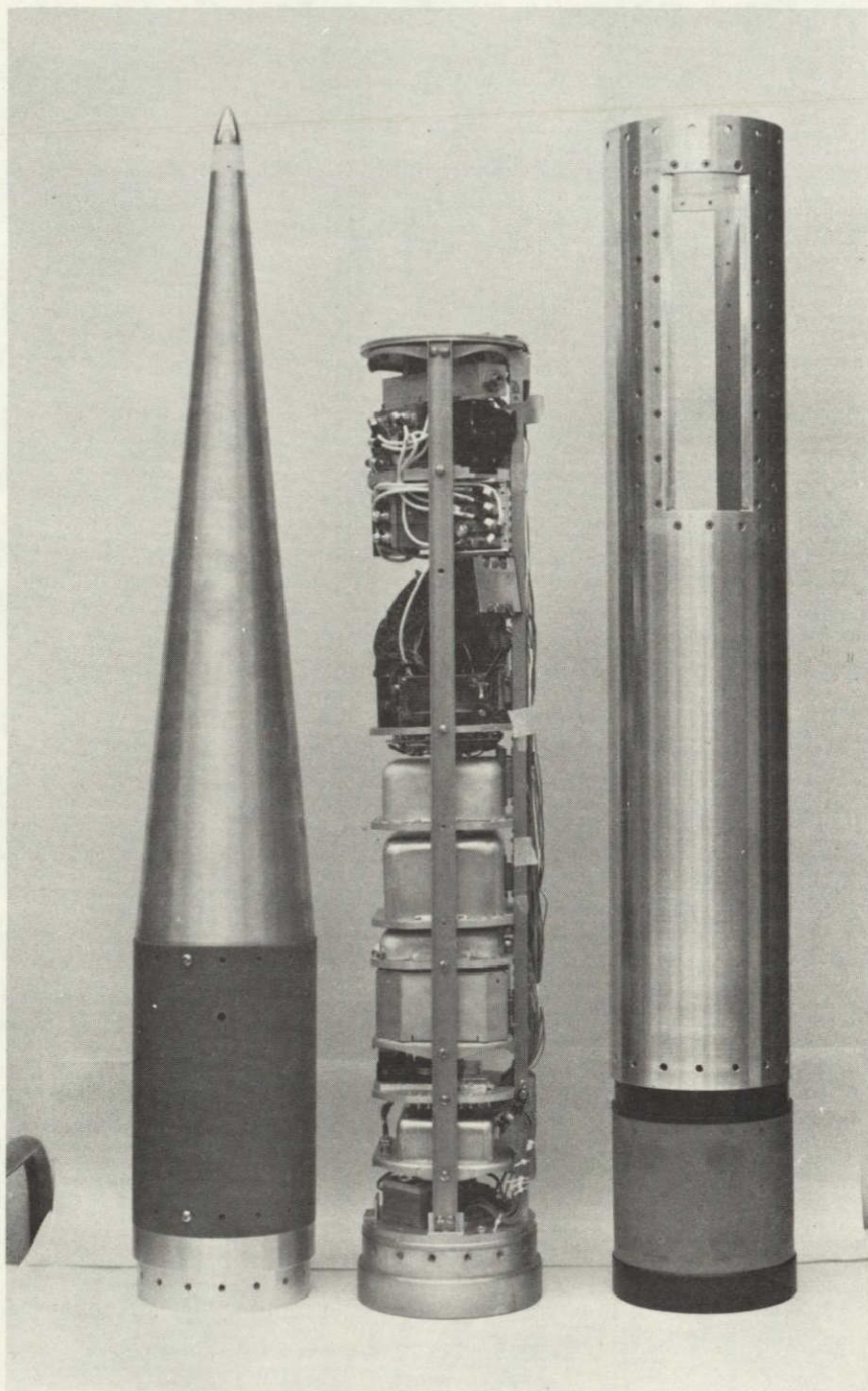


Figure 4.10 Disassembled payload of Nike Apache 14.542.

5. ELECTRONIC CIRCUITS

5.1 *Plate Voltage Sweep Circuit*

The purpose of the plate voltage sweep circuit is to provide the necessary potential difference across the analyzer plates. It is the electric field that will exist between the plates due to this potential that will deflect particles towards the detector. Changes in the electric field strength brought about by the plate voltage sweep circuit make possible a spectral analysis of the incoming energetic particles. Because the instrument is required to measure electrons and protons, though not simultaneously, it is necessary for the sweep circuit to alternate both polarities of voltage.

A block diagram of the plate voltage sweep circuit is shown in Figure 5.1. The clock and synchronization circuit drives the sweep waveform generator. This clock signal may be synchronized with the output signal from an on-board magnetometer. The sweep waveform generator creates the desired plate voltage waveform at a low voltage level. This waveform is then stepped up to the desired high voltage level and applied to the analyzer plates by the plate voltage power supplies. It is with these power supplies that a detailed description of the circuit operation begins.

5.1.1 *Plate voltage power supplies.* The analyzer plate voltage is generated by two high voltage power supplies. One is used to generate negative fields and the other, positive fields. The supplies are the vacuum-sealed model Q-30Z manufactured by Venus Scientific Inc. of Farmingdale, New York. Specifications for the Q-30Z supply are listed in Table 5.1. The output voltage of each supply is floating relative to the input voltage. The magnitude of the dc output voltage, up to 3000 V, is directly proportional to the dc input voltage over the range 2 to 12 V, Figure 5.2.

When connected as in Figure 5.3, these supplies provide an analyzer plate voltage of either polarity. Because of the grounded center tap of the high impedance voltage divider, the plate voltage is always symmetric about ground potential. In order to provide for the maximum possible excursion of the plate voltage only one of the two supplies is turned on at any given time. With supply A turned on, the outer plate will be positive with respect to the inner plate and the plates will deflect protons and other energetic positive ions to the detector. When supply B is on, the outer plate will be driven negative with respect to the inner plate and electrons will be deflected to the detector.

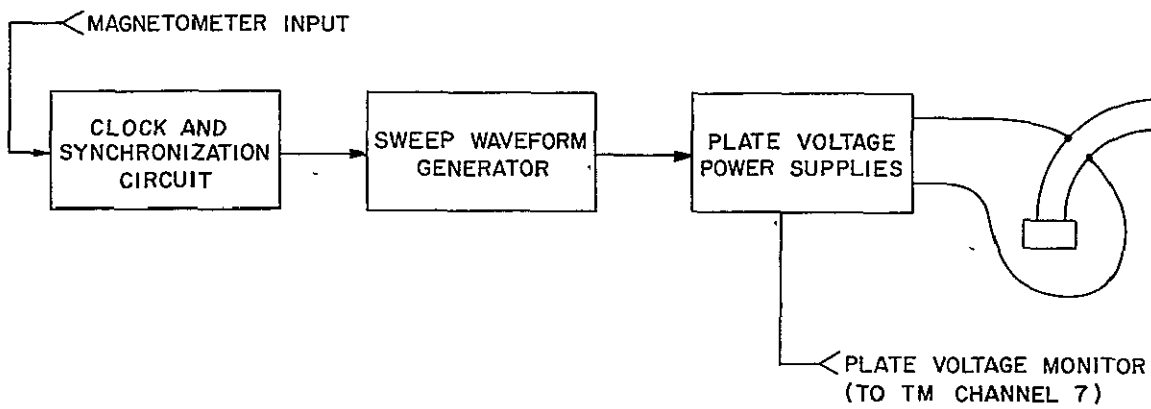


Figure 5.1 Plate voltage sweep circuit -- generalized block diagram.

Table 5.1

Plate voltage power supplies specifications.

Model Q-30Z

Manufactured by Johnston Laboratories, Inc.

Variable DC-to-DC Converter

Input Voltage:	2 to 12 VDC
Input Current (maximum):	90 mA
Output Voltage:	500 to 3000 VDC (Proportional to Input $\pm 5\%$)
Output Current:	200 μ A maximum
Ripple (maximum):	0.25%
Insulation Strength:	3500 V Input/Output
Input/Output Floating	
Dimensions:	1" dia. \times 2 $\frac{1}{2}$ " (2.5 cm dia. \times 6.4 cm)
Volume:	2 cu. in. (33 cm ³)
Weight:	3.5 oz. (100 gm)
Packaging:	Solid Encapsulation, Steel Can, Vacuum Sealed for High Vacuum Environments

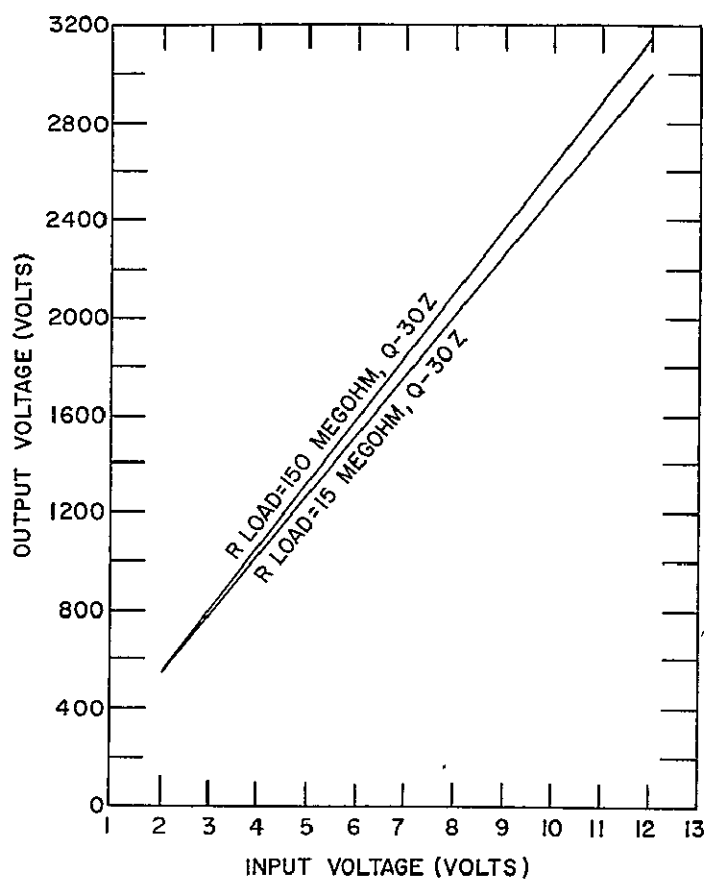


Figure 5.2 Output voltage as a function of the input voltage for the Venus Q-30Z power supply (manufacturer's specified typical performance at 25°C) [Venus Scientific, Inc. product brochure]

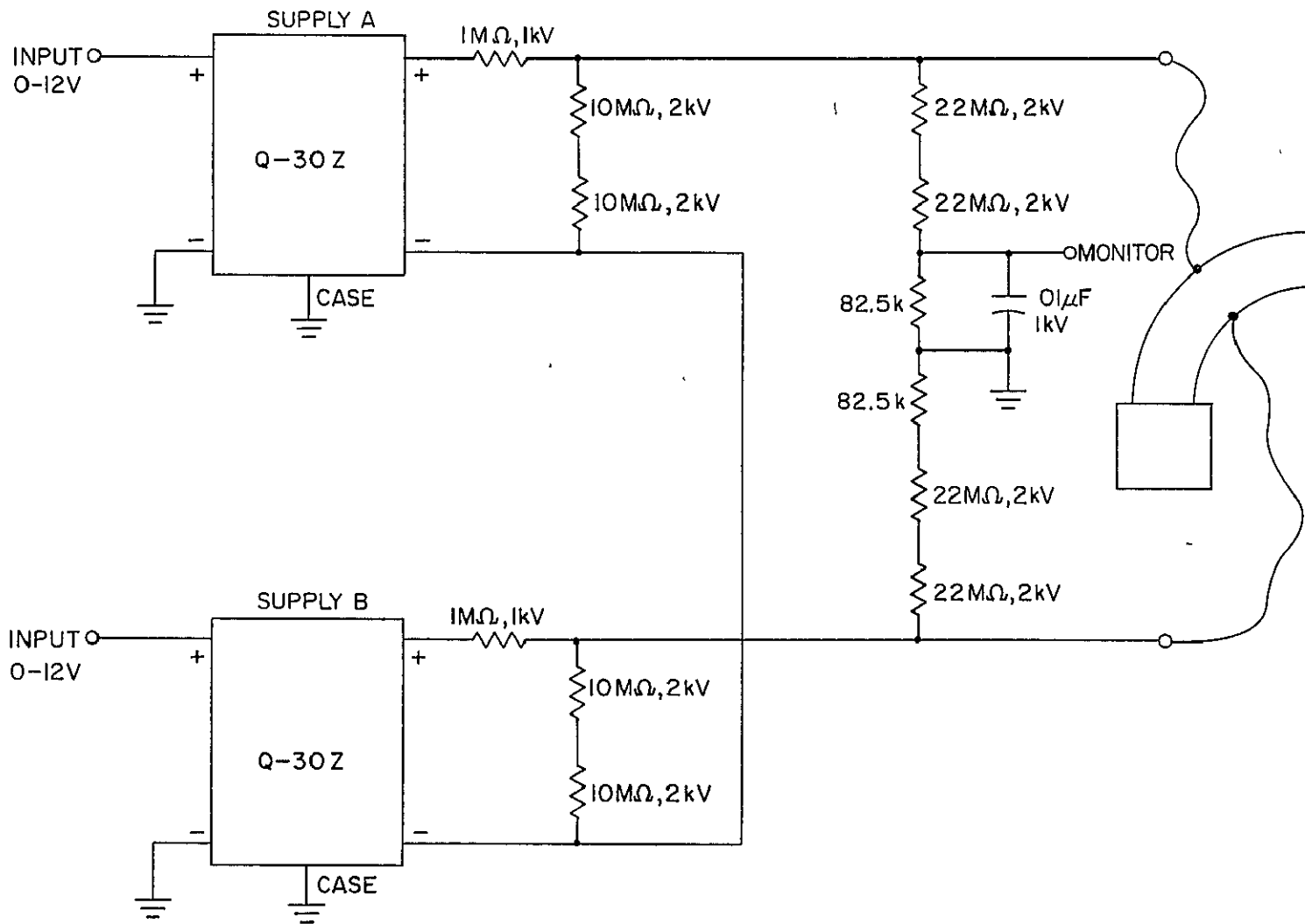


Figure 5.3 Plate voltage power supplies.

In series with the high impedance divider are two 82.5 k Ω resistors, one on either side of the grounding point. These are inserted so that a fraction (nominally 0.08%) of the total plate voltage can be monitored directly for telemetry to the ground. The input impedance of the telemetry channel VCO is 500 k Ω . The plate voltage is reduced to the range of from -2.5 V to +2.5 V by this resistor divider network.

Note that all of the high value resistors are rated at 2 kV and that at no time is this maximum voltage rating exceeded.

5.1.2 *Sweep waveform generator.* The approach used in generating the plate voltage waveform is illustrated in Figure 5.4. In this figure each division on the horizontal (time) axis represents one cycle of the clock signal. The waveforms of the inputs of the power system are a series of logarithmically spaced voltage steps. The waveforms are 180° out of phase with one another. As is seen in Figure 5.4, only one of the voltages has a non-zero value at any given time. This insures that power supplies A and B will not turn on simultaneously. During the first half cycle, supply A will drive the outer plate through a series of voltage steps, positive with respect to the inner plate, while supply B is off. Then during the second half-cycle, supply B will drive the outer plate through a series of voltage steps, negative with respect to the inner plate, while supply A is turned off.

The sweep circuit used to drive the power supplies is shown in Figure 5.5. It requires as an input a TTL-compatible 0 to +5 V clock signal which is generated by the clock and synchronization circuit. The input clock signal is used to drive a 4-bit binary counter. The four output lines of the counter are fed to a 4 to 16-line decoder. Each period of the output waveform is thus separated into 16 divisions, each division representing one cycle of the input clock signal. As the clock signal bounces up and down, the decoder will sequence through its 16 output lines pulling one line low at a time while all other outputs remain high.

Each of the 16 decoder outputs is fed to a non-inverting open-collector driver. The SN7407 driver was chosen because of its rated maximum high level output voltage $V_{OH} = 30$ V. The output of each driver is connected through a resistor to the base of a Darlington pair transistor configuration. Also connected to that base is a 1 k Ω pull-up resistor to a regulated +15 V supply. This pull-up resistor, together with the driver resistance to

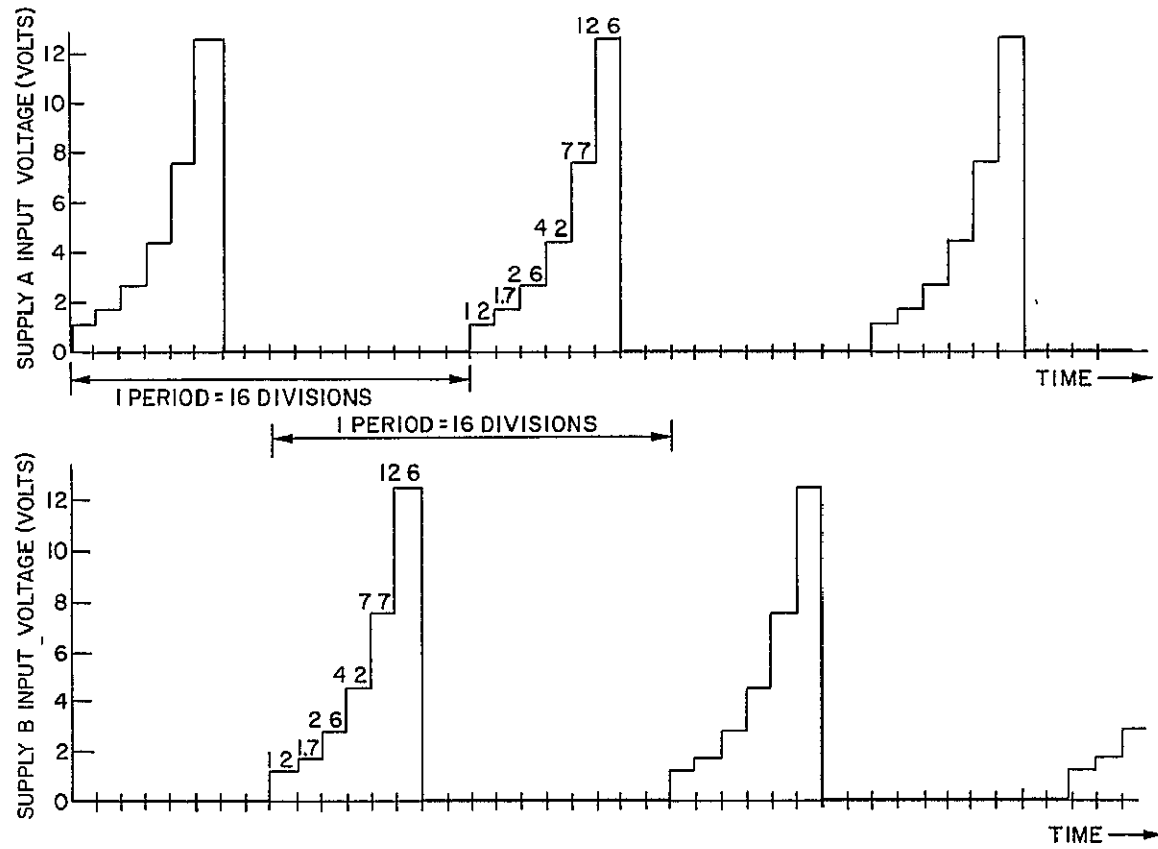


Figure 5.4 Power supply input voltage waveforms. Each division on the horizontal axis represents one cycle of the clock signal.

whichever driver is active (low), form a voltage divider which will determine the value of the voltage at the base of the Darlington pair. Only one of the driver resistors (R1 through R16) will be active at any given time as determined by the sequencing of the decoder outputs. Because the drivers are open-collector, no current will flow through any of the resistors R1 through R16 except the one fed by the active driver. Thus as the decoder activates the drivers one at a time sequentially, the voltage at the base of the Darlington pair will step through a series of levels determined by the resistances R1 through R16.

Driver resistances R35 and R36 determine the voltage levels to whichever Darlington pair is not activated by the 16 decoder outputs. These resistors are used to determine the state of one of the power supplies when the other supply is being stepped by the decoder. In the circuit shown in Figure 5.5, R35 and R36 have been chosen to be zero so that whichever supply is not being stepped will be turned off.

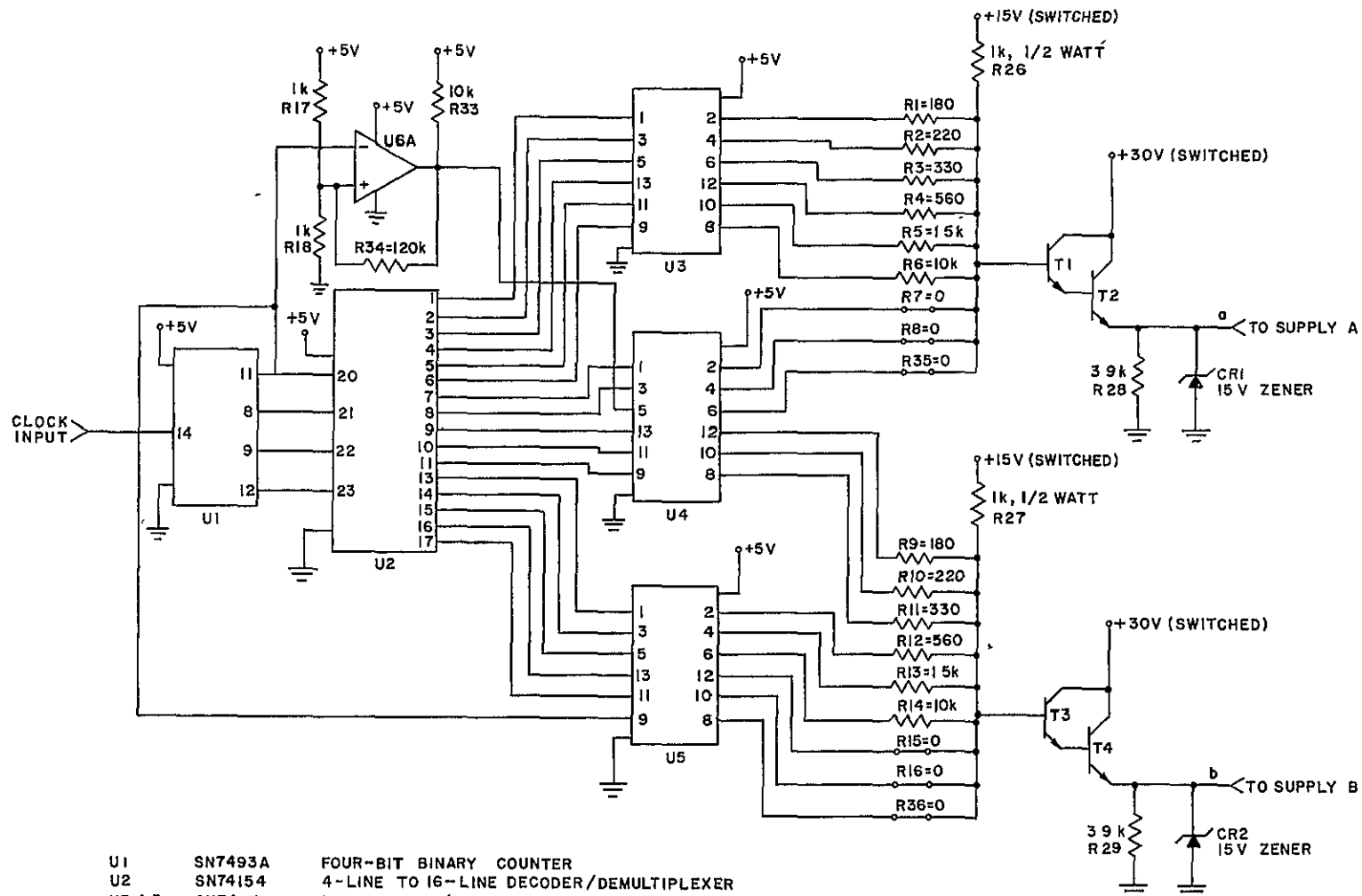
Drivers corresponding to the blanking resistors R35 and R36 are driven from the most significant bit output from the 4-bit binary counter. The comparator U6A is used as a TTL level inverter such that supply A will be off as supply B is being stepped (and vice versa).

Resistors R1 through R16 are chosen to produce whatever stepped waveform is desired. The values specified in Figure 5.5 are chosen so that the voltage levels are logarithmically related. This is done in anticipation of an energetic particle flux density which decays approximately exponentially with increasing particle energy.

Since up to 100 mA may be required to drive the power supplies at full output level, a Darlington pair is necessary as a current buffer to the voltage divider.

Resistors R28 and R29 provide a dummy load so that the plate voltage sweep circuit may be tested without connecting the power supplies. Zener diodes are added in parallel with resistors R28 and R29 in order to protect the power supplies.

Transistors T2 and T4 will run quite warm and are therefore provided with an adequate heat sink. In the present instruments, case style 77-03 was used and bolted directly to an aluminum plate used to cover the plate voltage sweep card.



- | | | |
|--------|------------|--|
| U1 | SN7493A | FOUR-BIT BINARY COUNTER |
| U2 | SN74154 | 4-LINE TO 16-LINE DECODER/DEMULTIPLEXER |
| U3,4,5 | SN7407 | HEX BUFFERS/DRIVERS WITH OPEN-COLLECTOR HIGH-VOLTAGE OUTPUTS |
| U6A | 1/4MC3302P | QUAD SINGLE-SUPPLY COMPARATOR |
| T1, T3 | 2N2270 | GENERAL PURPOSE MEDIUM POWER NPN |
| T2, T4 | 2N4922 | SILICON NPN POWER TRANSISTORS |
- ALL RESISTORS 1/4 WATT UNLESS OTHERWISE LABELLED

Figure 5.5 Sweep waveform generator. The waveforms of Figure 5.4 can be observed at points a and b.

The +30 V supply to the Darlington pair and the regulated +15 V supply to the voltage dividers are both switched on 88 seconds after launch, at an altitude of about 115 km, in order to avoid the high voltage arcing which might otherwise occur in the payload as the rocket passes through the lower atmosphere.

5.1.3 *Clock and synchronization circuit.* For ease of data reduction it is desired that each of the 16 divisions in a period of the voltage sweep waveform (i.e., each voltage level in the staircase waveform) corresponds in time to exactly one revolution of the rocket payload about its longitudinal axis. This is accomplished by synchronizing the clock signal to the output of a magnetometer located in the payload and oriented perpendicular to the spin axis.

The magnetometer is a device which senses the orientation of the payload with respect to the magnetic field of the earth. As the payload spins in that field, the magnetometer output is a sinusoid with a peak-to-peak value of typically 4 V centered at +2.4 V. The period of this sinusoid will be exactly the same as the payload spin period. Mid-flight spin rates for some previous Nike Apache rocket payloads are given in Table 5.2. A spin rate in the range from 6 to 8 revolutions per second is expected.

It is also desirable to have the plate voltage sweep waveform generated when the payload is not spinning as, for example, during the pre-launch testing. For this reason, the plate voltage sweep circuit is also provided with its own internal oscillator which can be used if the magnetometer signal should fail during the flight. Thus the clock and synchronization circuit must be able to choose the appropriate clock source (either the magnetometer signal or the internal oscillator) and to apply it in a TTL-compatible form to drive the sweep waveform generator. If the magnetometer signal is present at a frequency greater than 3 Hz, then it will override the internal oscillator as the clock source. If the magnetometer signal is not present, or is present at a frequency less than 3 Hz, then the internal oscillator will take over as the clock source.

The clock and synchronization circuit is shown in Figure 5.6. Comparator U6B is used as a Schmitt trigger in this arrangement to convert the magnetometer sinusoid into a TTL-compatible 0 to +5 V square wave. Comparator U6C is used as a free-running oscillator. Its output is also a 0 to +5 V square wave

Table 5.2

Spin rates of Nike Apache rockets.

<u>Rocket</u>	<u>Date (UT)</u>	<u>Spin Rate</u>	<u>Spin Period</u>
14.533	1/5/78	7.06 rps	142 ms
14.534	8/10/77	7.38 rps	136 ms
14.525	6/2/75	6.39 rps	156 ms
14.524	5/30/75	7.43 rps	135 ms
14.523	6/30/74	6.50 rps	154 ms
14.522	6/30/74	6.70 rps	149 ms
14.521	6/30/74	6.37 rps	157 ms
14.520	4/19/74	<u>7.20 rps</u>	<u>139 ms</u>
	Average	6.88 rps	146 ms
	Range of spin rate:	6.37 to 7.43 rps	
	Range of spin period:	157 to 135 ms	
	Nominal spin rate:	6 to 8 rps	

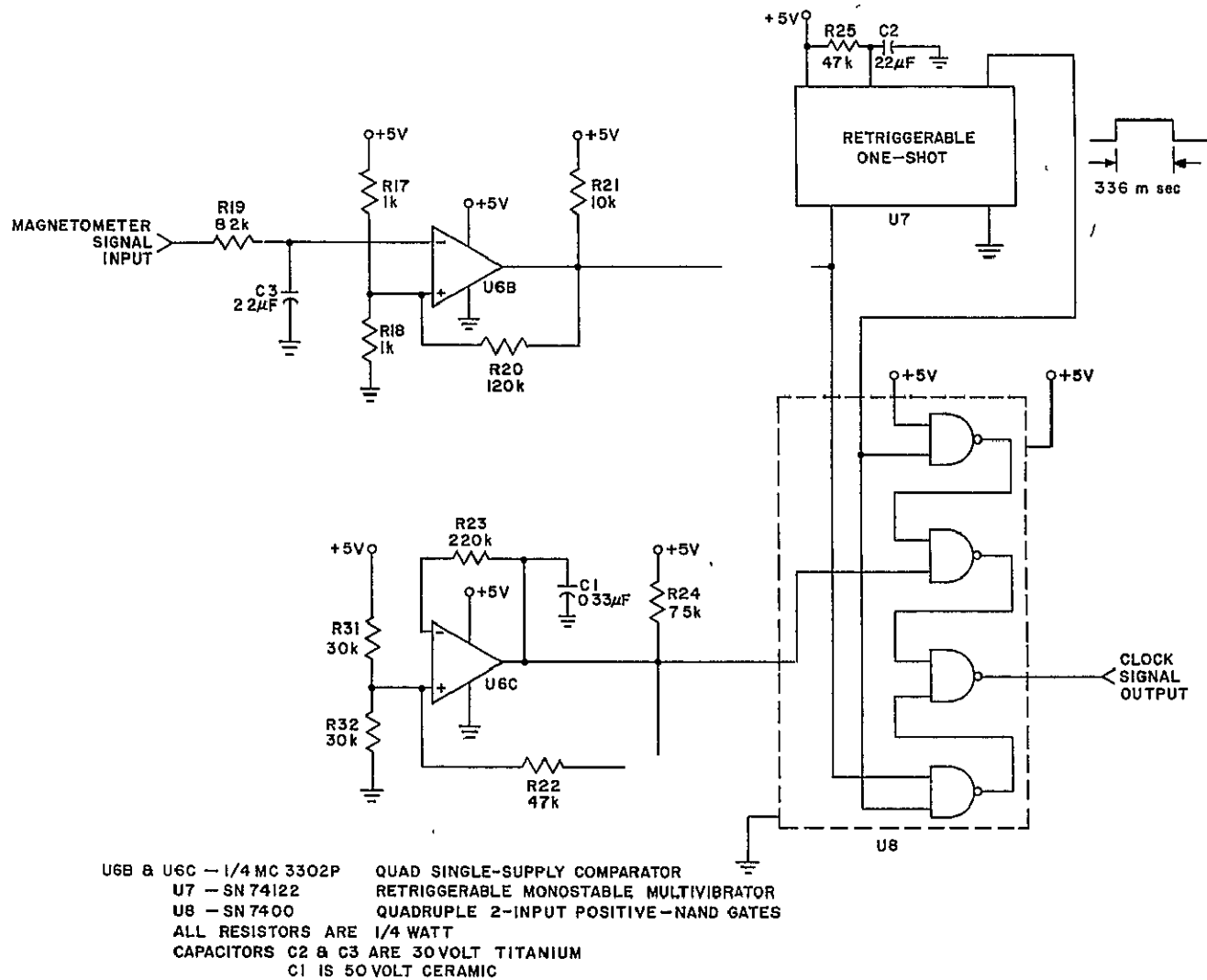


Figure 5.6 Clock and synchronization circuit.

with a frequency of approximately 7 Hz. The output of the Schmitt trigger U6B is fed to a retriggerable one-shot multivibrator with an output pulse width of 336 ms. As long as the frequency of the magnetometer signal is greater than 3 Hz the output of the one-shot will remain high. If the magnetometer signal is not present, the one-shot output will stay low.

The four NAND-gate arrangement (U8) is used as a gating structure which passes either the magnetometer signal or the internal oscillator signal, depending upon the state of the one-shot output. If the output of the one-shot is high, indicating the presence of a magnetometer input, then the signal from the magnetometer will be gated through as the clock signal output. If, on the other hand, there is no magnetometer signal present, then the one-shot output will be low causing the internal oscillator signal to be gated through. It is in this manner that the proper clock signal is chosen and passed on to drive the plate voltage sweep waveform generator.

5.1.4 *Sweep circuit performance.* The circuit of Figure 5.3 is capable of supplying plate voltages, in either polarity, in the range of 200 to 3000 V. Since the plate voltage is directly proportional to the selected particle energy, a logarithmic relationship between the desired energy levels will imply a logarithmic relationship between the chosen plate voltages. The voltage levels of the plate voltage waveform are therefore chosen to be logarithmically distributed from 200 to 3000 V. These levels are given in Table 5.3, where the multiplicative factor from each value to the next is

$$n = \left(\frac{3000}{200} \right)^{0.2} = 1.719$$

Also shown in Table 5.3 are the approximate power supply input voltages needed to produce those plate voltages. These values were obtained from the graph of Figure 5.2.

From the desired power supply input voltages it is a simple matter to calculate the needed resistance values R1 through R16. Let V_d be the desired control voltage to the supply (at a and b in Figure 5.5). If V_{be} is the base-to-emitter voltage drop across each of the transistors, and V_{sat} is the low level output (saturation) voltage of an open-collector driver, then the resistance value needed to produce a voltage V_d to the supply is given by

$$R = 10^3 \left(\frac{V_d + 2V_{be}}{15 - V_{sat} - 2V_{be}} \right) \quad (5.1)$$

Table 5.3

A summary of the resistor value calculations.

Plate Voltage (volts)	Supply Input Voltage V_d (volts)	R (calculated) (Ω)	R (standard) (Ω)	Corresponding Particle Energy (keV)
200	1.2	177.9	180	0.90
344	1.7	226.3	220	1.55
591	2.6	330.4	330	2.67
1016	4.2	544.0	560	4.59
1745	7.7	1.423 k	1.5 k	7.89
3000	12.6	10.92 k	10 k	13.56

Using measured values of $V_{be} = 0.5 \text{ V}$ and $V_{sat} = 0.1 \text{ V}$ in this equation leads directly to the calculated resistance values given in Table 5.3. The standard resistor values actually used in the circuit are also listed. Particle energies corresponding to these levels of plate voltage, using the proportionality factor of equation (4.9) are also given.

Due to the capacitance of the output filter of the plate voltage power supplies, the voltage on the analyzer plates decays exponentially after each supply is turned off. It is found experimentally that, with the resistive load provided by the circuit of Figure 5.3, the time constant of this decay is about 100 ms. Two divisions (approximately 300 ms) are set aside each half cycle to allow the voltage of one supply to decay before the other supply is switched on. This is accomplished by setting resistors R7, R8, R15 and R16 (Figure 5.5) equal to zero.

A summary of the final chosen resistor values together with the corresponding particle energies is provided for easy reference in Table 5.4.

Figure 5.7 shows the analyzer plate voltage as a function of time assuming a rocket spin rate of 7 revolutions per second. Counts obtained during the decay portions of this waveform will be useful in defining the fine structure of the energetic particle spectra.

Figure 5.8 is a photograph of the waveform observed at the plate voltage monitor (see Figure 5.3). This is a fraction (nominally 0.08%) of the actual plate voltage and can be used to determine exactly the plate voltage at any given time.

5.2 *Electron Multiplier High Voltage Supply*

Charge amplification is provided in the electron multiplier by the generation of secondary electrons through a series of collisions with the multiplier dynodes. A large potential difference must exist between the dynode stages in order to accelerate these electrons toward further collisions. This potential is provided by the electron multiplier high voltage supply.

Shown in Figure 5.9 is a schematic representation of the MM-1 electron multiplier. The multiplier is used here in the pulse counting mode with the anode at high potential. The twenty dynode stages are shown connected by $5 \text{ M}\Omega$ load resistors. These resistors, which are integrated into the construction of the detector, serve as voltage dividers to provide approximately the same electron accelerating potential between any two adjacent dynode stages. A high voltage power supply is connected between the back plate and the suppressor

Table 5.4

A summary of the chosen resistor values
and corresponding particle energies.

<u>Resistor Value (ohms)</u>	<u>Particle Energy (keV)</u>	
R1 = 180	0.90	} Protons
R2 = 220	1.55	
R3 = 330	2.67	
R4 = 560	4.59	
R5 = 1.5 k	7.89	
R6 = 10 k	13.56	
R7 = 0	0	
R8 = 0	0	
R9 = 180	0.90	} Electrons
R10 = 220	1.55	
R11 = 330	2.67	
R12 = 560	4.59	
R13 = 1.5 k	7.89	
R14 = 10 k	13.56	
R15 = 0	0	
R16 = 0	0	

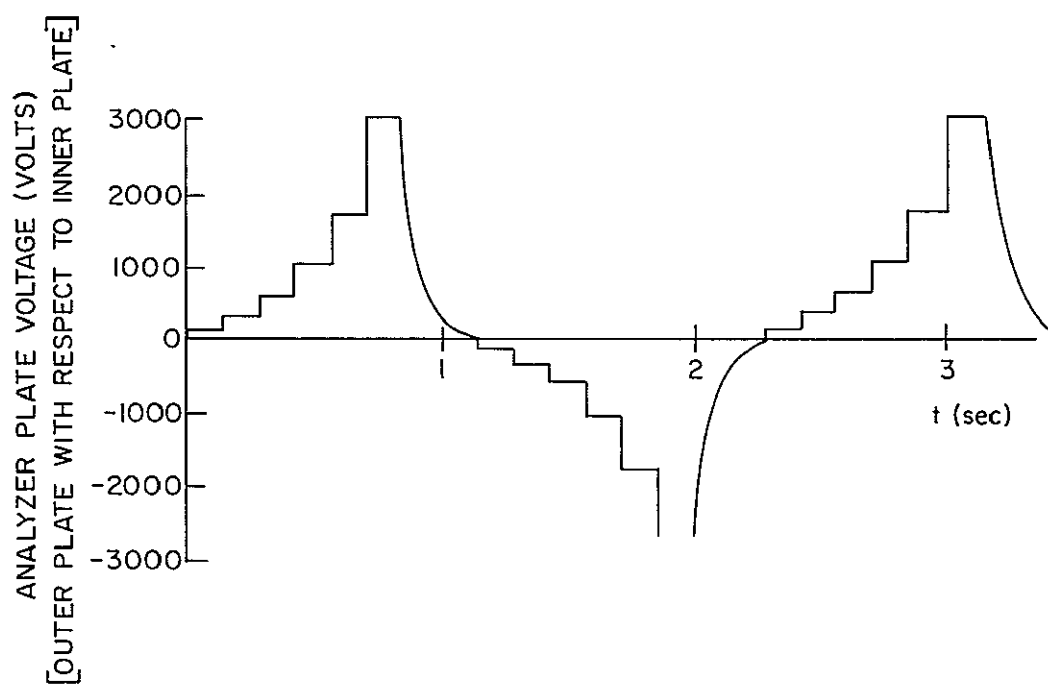


Figure 5.7 A sketch of the analyzer plate voltage as a function of time (assuming a spin rate of 7 rps).

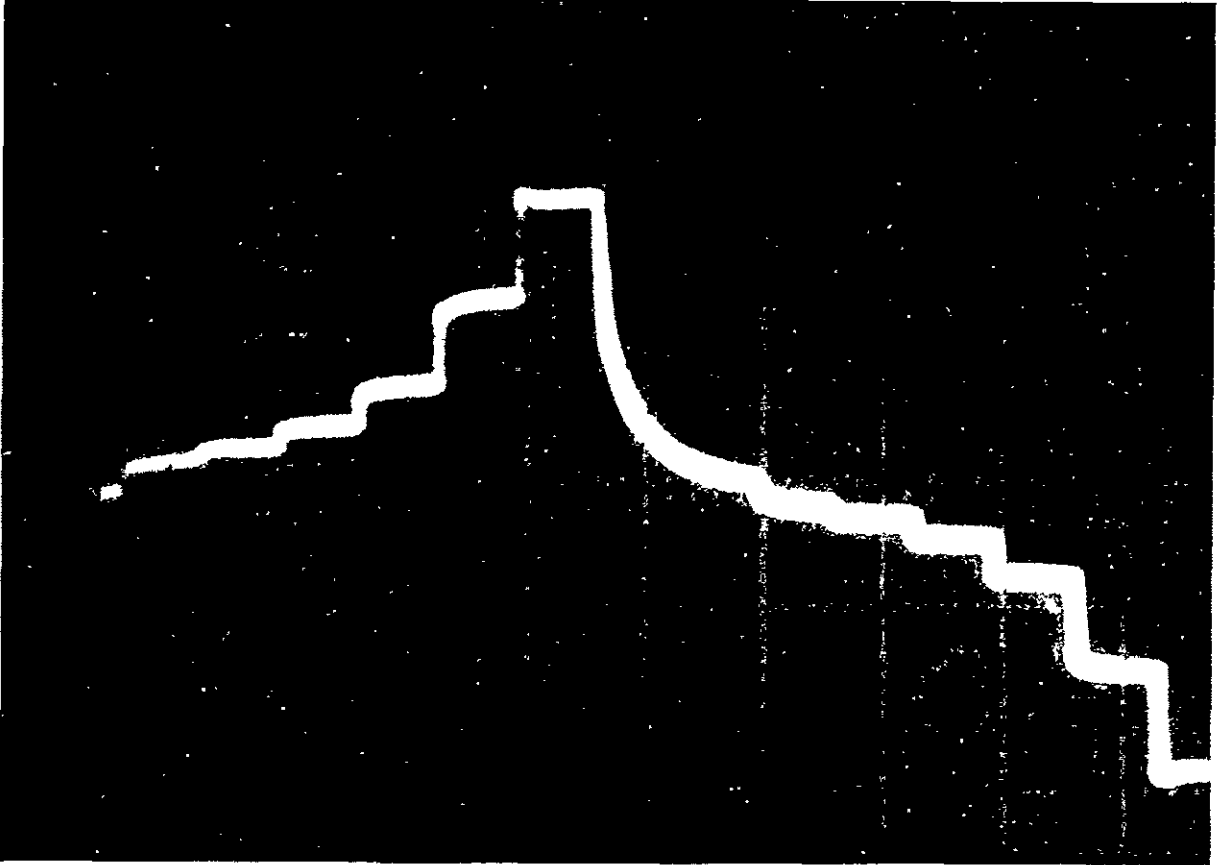


Figure 5.8 A photograph of the plate voltage monitor waveform.

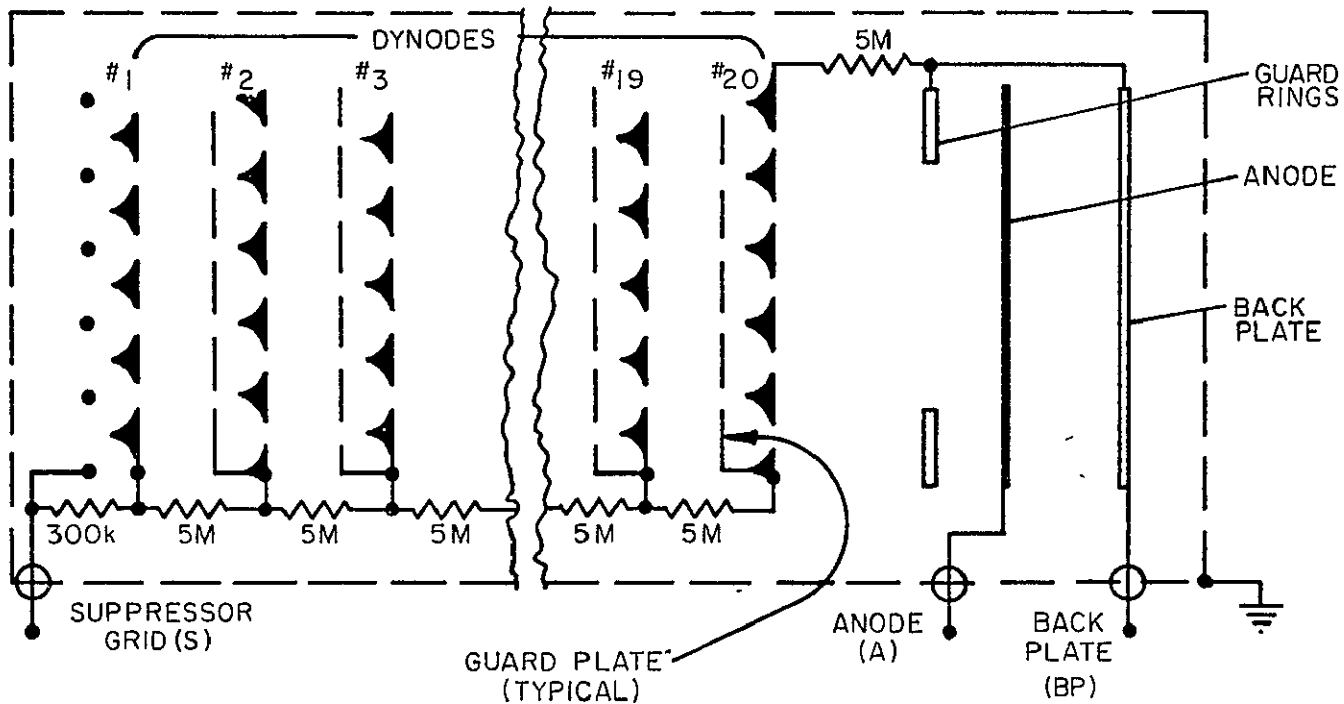


Figure 5.9 Electrical connections to the MM-1 multiplier [Johnston Laboratories, Inc., Technical Data Application Note, JLI-605].

grid with the back plate positive and the suppressor grid grounded. Approximately 4 kV is applied to the back plate so that the current through the dynode resistors is 40 μ A. The potential between adjacent dynodes is therefore 200 V.

The anode is kept at high potential by a load resistor connected between it and the back plate. After an energetic particle enters the detector, a burst of secondary electrons will be accelerated through the twenty dynode stages and towards the anode. When the electron burst strikes the anode, there will be a small negative excursion in the anode voltage. The anode is capacitively coupled to the input of a charge-sensitive preamplifier.

The circuit of the high voltage supply is shown in Figure 5.10. The dc-to-dc high voltage converter used in this application is the Tecnetics model 9567-119. Specifications for the Tecnetics converter appear in Table 5.5.

For packaging in the instrument the Tecnetics converter was placed in a fitted magnetic shield. This drastically reduced the level of electromagnetic interference which originates from within the unit and can be disruptive to the surrounding circuits.

Resistors R1 and R2 in Figure 5.10 provide an additional load to better stabilize the converter. R3, C2 and R4, C3 are cascaded RC low pass filter stages providing additional filtering for the power supply. R5 is the load resistor across which a small voltage will be developed as an electron burst strikes the anode. The negative charge burst is neutralized by positive current from the power supply through R5 causing a negative pulse on the anode voltage. Each pulse is approximately 10 mV in amplitude and 10 ns in duration.

Inductor L1 and capacitor C1 form a low pass filter at the input to the Tecnetics converter. This filter is intended to keep any high frequency transient which might develop on the +28 V line from affecting the operation of the high voltage supply. This safeguard helps to insure that the bias level and hence the gain from the MM-1 electron multiplier will remain constant. The filter also prevents the converter from adding noise to the +28 V line.

Two cascaded RC high pass filters deliver the anode signal in Figure 5.10 to the preamp. The first filter, which consists of C4 and R6, is designed basically to remove the high dc bias voltage. C4 is a high voltage (6 kV)

Table 5.5

High voltage dc-to-dc converter specifications.

Model 9567-119

Manufactured by Tecnetics, Inc.

Input Voltage:	28 VDC \pm 3 VDC continuous 50 VDC for 1 sec max
Input Current:	38 mA typical @ 100 mW load 210 mA typical @ full load
Minimum Load:	100 mW
Maximum Load:	3 W
Output Voltage:	4000 VDC nom
Output Voltage Adjust:	\pm 10% @ full load
Output Current:	0.75 mA max
Output Ripple:	28.0 V p-p max
Line Regulation:	21.0 VDC max ($V_{in} = 25$ to 31 VDC)
Load Regulation:	165.0 VDC max (1/2 to Full)
Dimensions:	1.5 \times 3.0 \times 0.6 in (3.8 \times 7.6 \times 1.5 cm)
Weight:	4.0 oz (110 gm) fully encapsulated

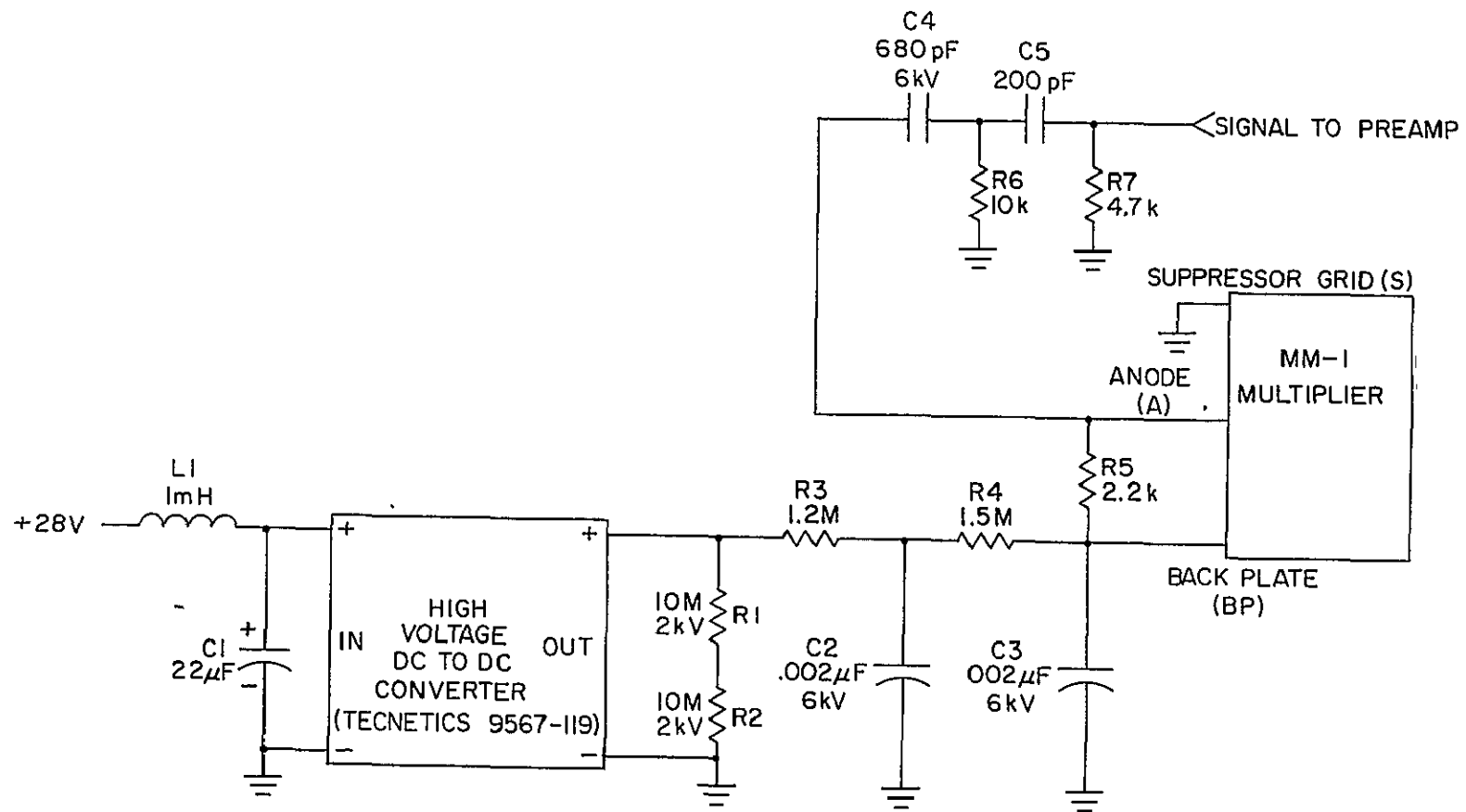


Figure 5.10 MM-1 multiplier and associated high voltage electronics.

ceramic disk capacitor. The nominal 3 dB cutoff of this first filter stage is 23.4 kHz.

The second filter, formed by C5 and R7, is designed to remove higher frequency noise from the anode signal such as noise from the chopper amplifier of the Tecnetics dc-to-dc converter and the resultant power supply ripple. The nominal 3 dB cutoff of this second filter stage is 169 kHz.

5.3 Preamplifier

Output charge pulses from the electron multiplier result in negative-going voltage pulses across the load resistor R7 (Figure 5.10) as described in Section 5.2. These small, fast pulses are fed to the input of a charge-sensitive preamplifier. The output pulses from the preamplifier are to drive the TTL-compatible counting electronics to be described in Section 5.4. The preamplifier must invert and amplify each input pulse so that the corresponding output pulse is 0 to +5 V TTL-compatible.

A schematic diagram of the preamplifier circuit is shown in Figure 5.11. It is adapted from a charge preamplifier developed for an airglow photometer [Paarmann and Smith, 1977]. The first stage, the MC1733L, is a wideband differential video amplifier. Successive stages are MC10216 high speed emitter-coupled differential amplifiers. Discrete transistors Q1 and Q2 form a single-ended differential amplifier output stage.

Charge pulses are capacitively coupled from the output of the MM-1 to the input of the preamp. Since most of the input charge (q) is dumped into the input capacitance (C_{in}) of the preamplifier, the magnitude of the input voltage pulse (V_{in}) is given approximately by

$$V_{in} = \frac{q}{C_{in}}$$

The input capacitance is made up of both inherent and stray capacitances of the preamplifier circuit. It has been measured experimentally and has a value of 17 pF [Paarmann and Smith, 1977]. Given an incident particle of one elementary charge and a multiplier gain of 10^6 , the input voltage pulse will have a magnitude of approximately 10 mV.

Referring once more to Figure 5.11, note that R1, R2 and R3 in addition to establishing the bias conditions for the MC1733L also affect the input resistance (R_{in}) of the preamp. The width of the input voltage pulse is primarily determined by the input time constant $R_{in} C_{in}$. Resistors R1, R2

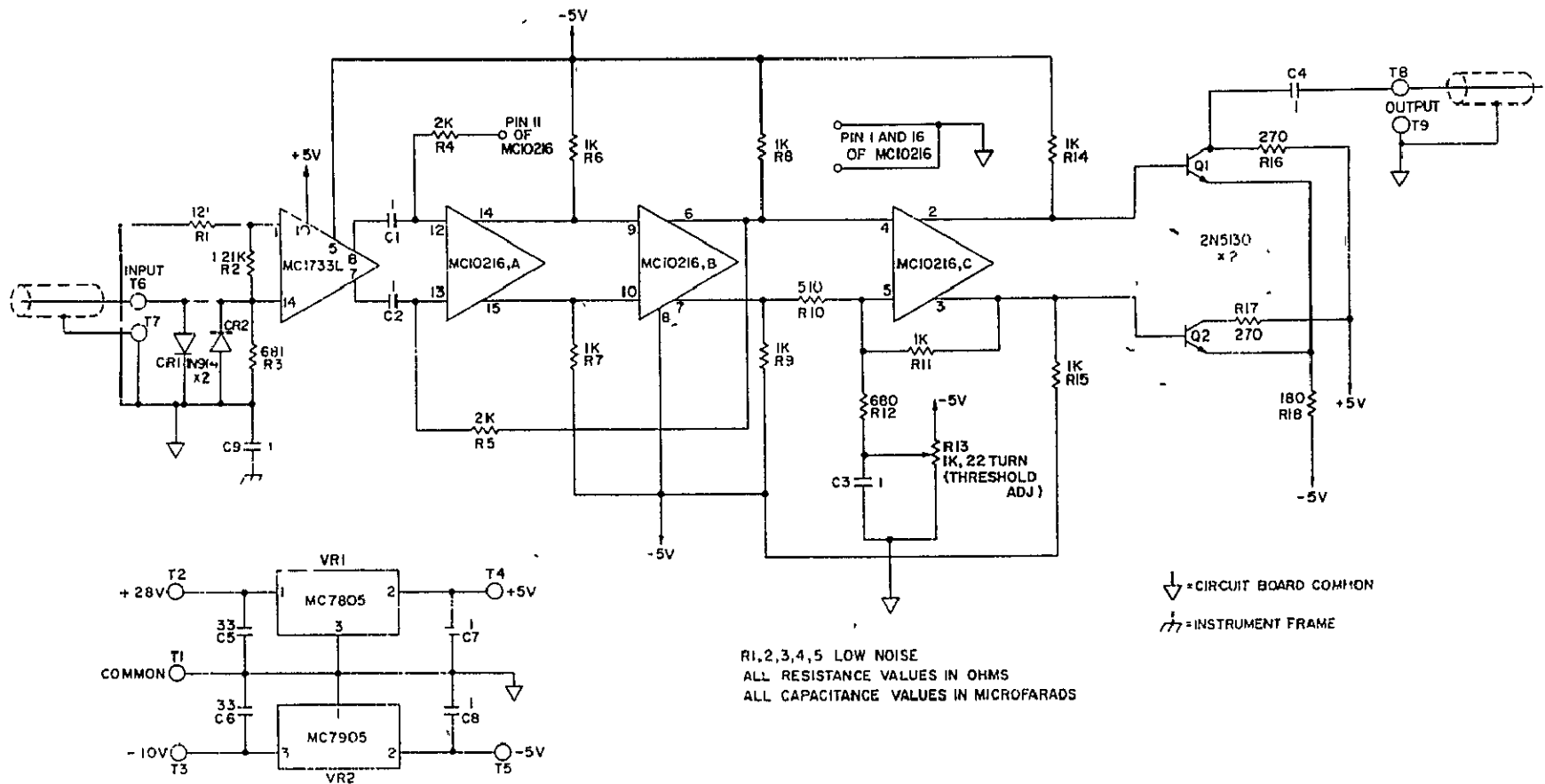


Figure 5.11 Pulse preamplifier schematic diagram [Paarmann and Smith, 1977].

and R3 have been chosen so that R_{in} is kept small in order to maintain a narrow input pulse width.

Diodes CR1 and CR2 have been placed across the input in order to prevent damage to the preamp due to high voltage transients. Such transients might occur as the electron multiplier high voltage supply is switched on.

The voltage gain from the input (T6) to pin 7 of the MC1733L is -5 and to pin 8 is +5. The following three MC10216 stages are emitter-coupled devices and provide current gain to the signal. The output stage differential amplifier then boosts the output voltage swing to approximately 4.5 V.

Due to the high gain of the preamplifier, there will be a significant amount of noise present at pins 4 and 5 of the MC10216. In order to prevent this noise from appearing at the output, a threshold-adjust potentiometer has been added to apply just enough negative offset to pin 5 to disable the output stage in the presence of noise. Thus only a significant excursion beyond the noise level (i.e., a signal pulse) will appear at the output. The threshold-adjust potentiometer was replaced in the flight instruments by appropriate discrete resistors.

Measured characteristics of the pulse preamplifier are listed in Table 5.6. Shown in Figure 5.12 are some typical input and output waveforms. The input signal was obtained from a Hewlett-Packard 8002A pulse generator and fed through a Kay model 30-0 attenuator. Oscilloscope traces were obtained with a Tektronix 7623.

The construction of the preamplifier circuit is illustrated in Figure 5.13. The input signal is fed by coaxial cable through the base plate of the instrument to the preamp at the upper left corner of the board. The output signal coax is visible near the upper right corner. The preamplifier circuit is mounted just below the MM-1 multiplier on the bottom side of the electrostatic analyzer deck.

5.4 Pulse Counting Circuit

Pulses from the preamplifier are processed by the pulse counting electronics which assemble them in a staircase format for telemetering to the ground. Correlation of this count rate with the observed plate voltage will later yield the desired particle energy spectra.

Figure 5.14 is a schematic representation of the pulse counting circuit. Pulses from the preamp are fed to the Schmitt trigger input of a monostable multivibrator. The output is a +5 V, 20 ns positive-going pulse which is used

Table 5.6

Pulse preamplifier measured characteristics
 [Pacermann and Smith, 1977].

Input Impedance (measured on an hp 4815A vector impedance meter at 10 MHz)	380 Ω \angle -24 $^\circ$, or 416 Ω shunted by 17 pF (includes approximately 4 inches of RG-188 A/U cable)
Voltage Gain from Input to Output (small input)	-1000
Output Amplitude	4.5 V
Minimum Input Amplitude for Proper System Operation	1.3 mV
Output Pulse Width at 50% points (input pulse width = 23 ns at 50% points)	40 ns (500 mV input) 30 ns (5 mV input)

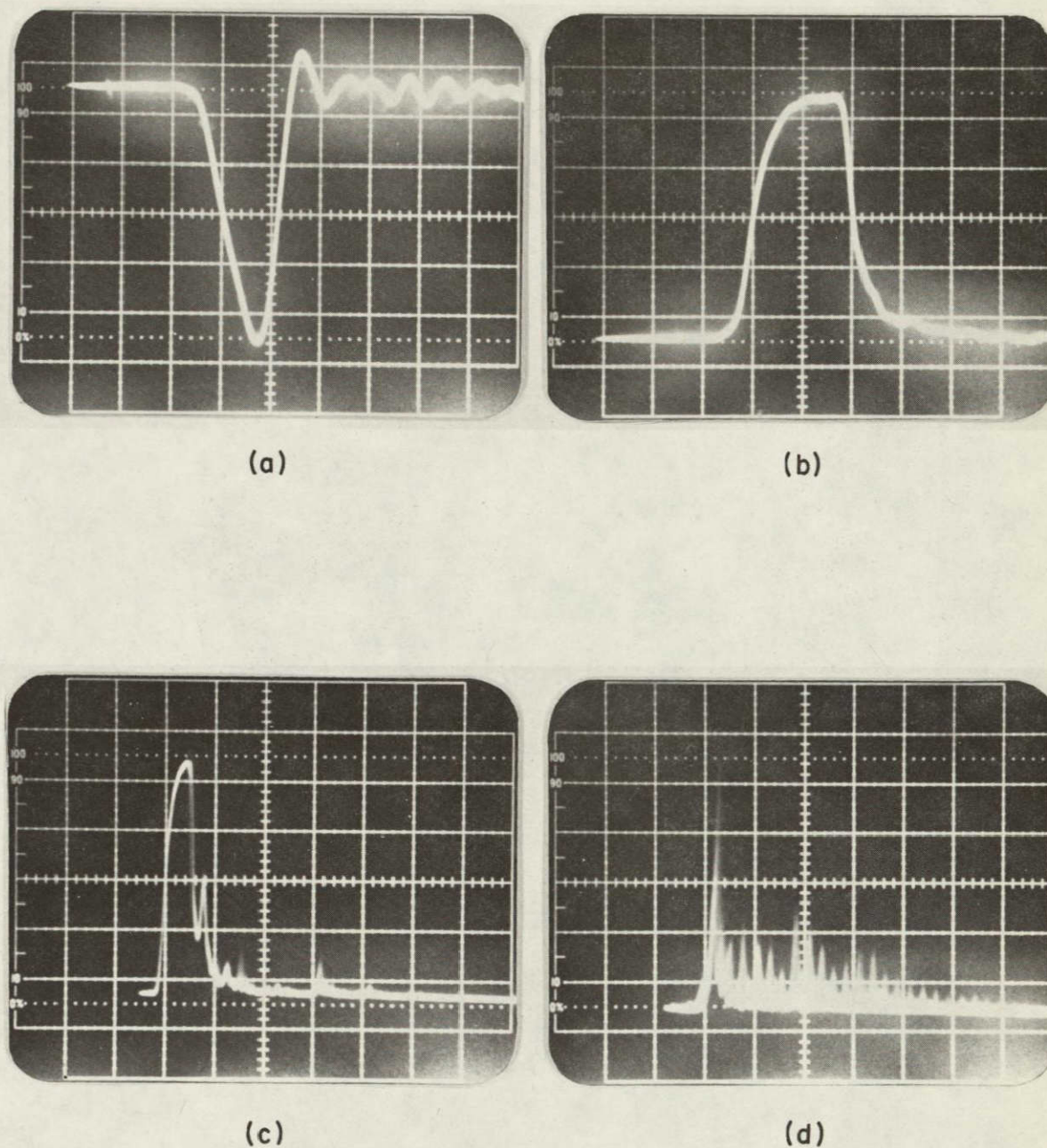


Figure 5.12 Pulse preamplifier input and output waveforms: (a) input: 20 ns/cm; (b) output: 1 V/cm, 20 ns/cm (input: 500 mV); (c) output: 1 V/cm, 50 ns/cm (input: 5 mV); (d) output: 0.5 V/cm, 50 ns/cm (input: 1.25 mV) [Paarmann and Smith, 1977].

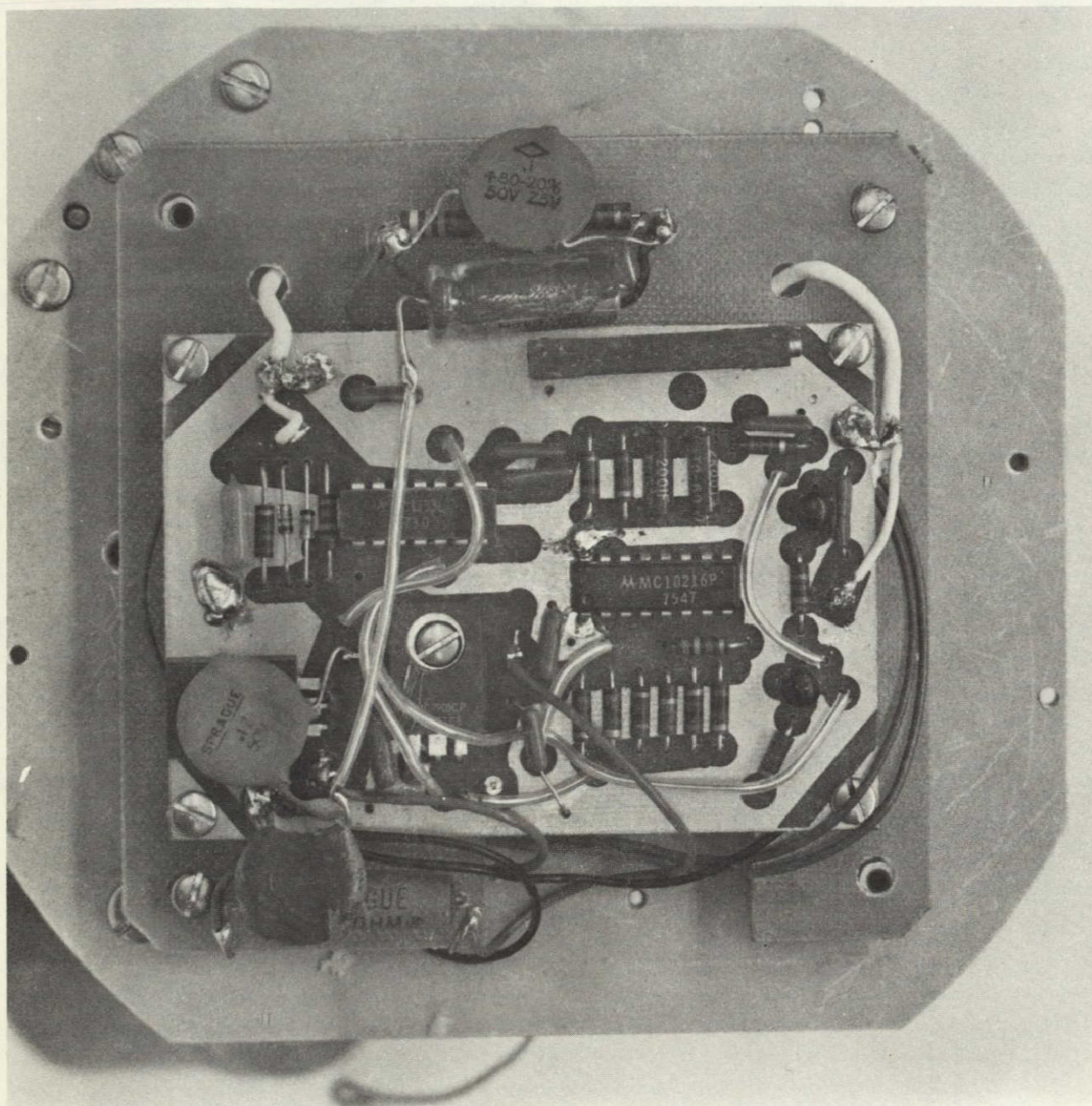


Figure 5.13 Pulse preamplifier physical construction.

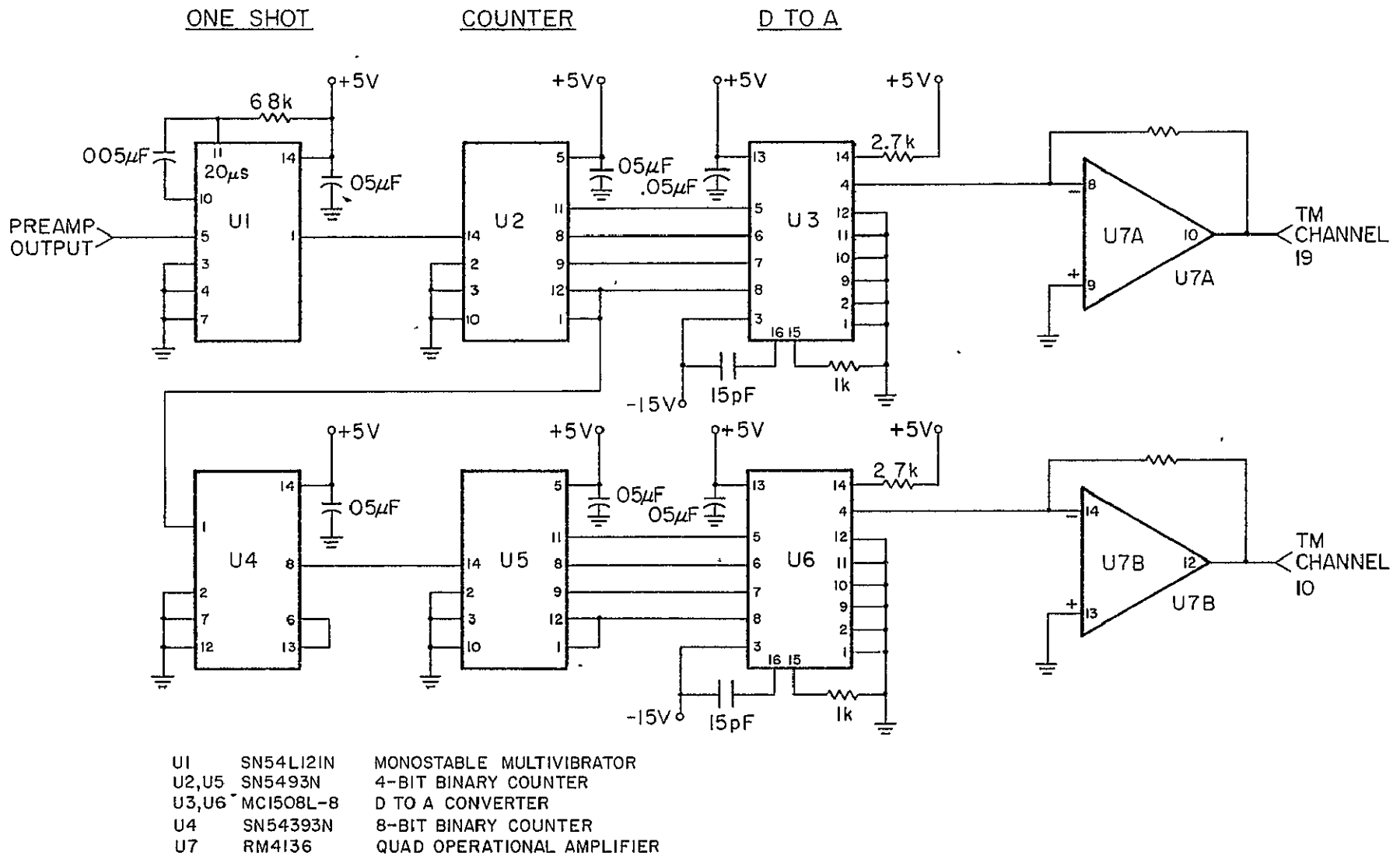


Figure 5.14 Pulse counting electronics [adapted from Voss and Smith, 1974]

to drive a 4-bit binary counter. The one-shot serves to better define the pulse shape and to eliminate effects of multiple triggering.

The four output lines from the counter U2 are fed to the four most significant bits of an 8-bit D/A converter. As the counter accumulates pulses, the analog output current of the D/A will step through a series of 16 discrete levels. The operational amplifier U7 is necessary to convert the current signal from the D/A to a voltage signal of sufficient magnitude for interface with the telemetry voltage-controlled oscillators. The output of op-amp U7A is a series of positive-going ramps, each ramp consisting of 16 discrete voltage levels equally spaced from 0 to +5 V. Each step of the ramp represents one count, so that 16 counts are represented by every ramp, as illustrated in Figure 5.15.

Telemetry channel 19, fed by operational amplifier U7A, is the main data channel for the electrostatic analyzer experiment. The bandwidth of channel 19 is 2000 Hz. With 16 counts per ramp and 2000 ramps per second, the maximum count rate allowed by the channel is 3.2×10^4 counts per second. The resolution for this channel will be ± 1 count each spin of the rocket, or approximately ± 7 counts per second.

Channel 10 is used as an overflow channel in case the main data channel saturates due to high count rate. The addition of an 8-bit binary counter U4 in Figure 5.15 causes each step in the ramp waveform of U7B to represent $2^9 = 512$ counts. The signal output to channel 10 is otherwise identical to that signal which is output to the main data channel.

The bandwidth of channel 10 is 100 Hz. The maximum count rate, 100 ramps per second with 16 steps per ramp and 512 counts per step, is 8.2×10^5 counts per second. The resolution of the overflow channel is ± 512 counts per rocket spin, or approximately $\pm 3.5 \times 10^3$ counts per second. Specifications for both the main and overflow data channels are summarized in Table 5.7.

5.5 *Pulse-Height Analysis*

The system described to this point is designed to determine the count rate at various energy levels for energetic electrons, protons and positive ions. It will yield a spectrum of the energetic electrons and another of both energetic protons and positive ions. It is not possible for this system to distinguish between energetic protons and various positive ions. The distinction can be made, however, if output pulses from the electron multiplier are also pulse-height analyzed.

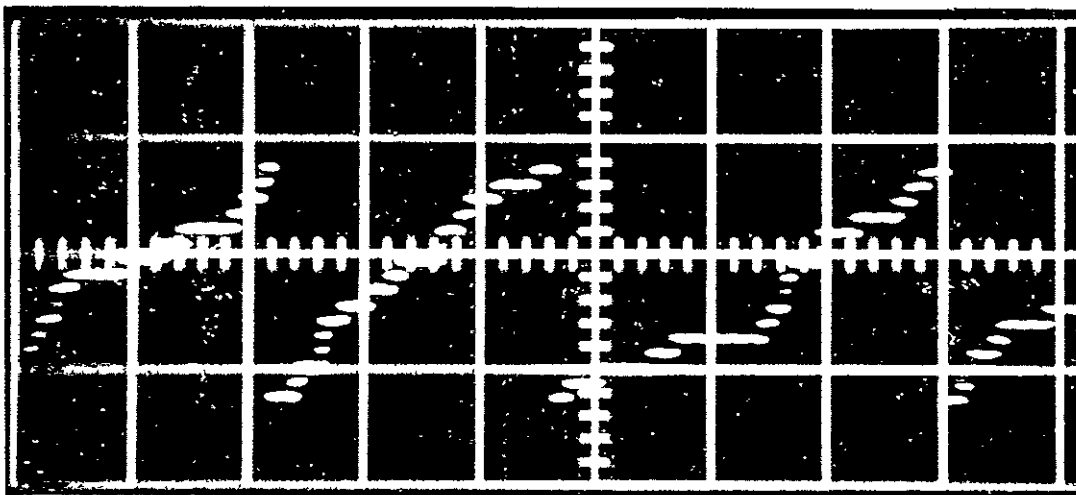


Figure 5.15 Output signal supplied to telemetry from the pulse counting electronics. Each ramp represents 16 counts. The horizontal sweep rate is 10 ms/cm, yielding a count rate of approximately 55 counts per second [Voss and Smith, 1974].

Table 5.7

Telemetry channel characteristics.

1. Main Data Channel, Channel 19

Bandwidth: 2000 Hz

Maximum Count Rate: $3.2 \times 10^4 \text{ s}^{-1}$

Resolution: $\pm 7 \text{ counts/sec}$

2. Overflow Channel, Channel 10

Bandwidth: 100 Hz

Maximum Count Rate: $8.2 \times 10^5 \text{ s}^{-1}$

Resolution: $\pm 3.5 \times 10^3 \text{ counts/sec}$

When the rocket reaches apogee, a switch is activated which allows the output pulses from the electron multiplier to be fed to one of the pre-amplifier and shaper circuits of the energetic particle spectrometer experiment. The shaper output is then pulse-height analyzed. Data from the pulse-height analyzer circuit are fed to an on-board microprocessor. The microprocessor assembles and formats the data before delivering it to channel 18 for telemetering to the ground. Multiplexed data from the pulse-height analyzer are also telemetered directly on channel H. Either set of data will allow one to identify energetic protons and/or positive ions on the downleg of the flight.

A description of the shaper circuit (and its associated preamplifier) is included in a report on the energetic particle spectrometer being prepared by K. L. Fries, L. G. Smith, and H. D. Voss. The pulse-height analyzer and multiplexer, and the microprocessor data-manipulation experiment are described in *Leung et al.* [1979] and in *Davis et al.* [1979], respectively.

6. INSTRUMENT CHARACTERIZATION AND CALIBRATION

6.1 *Introduction*

The two electrostatic analyzers built for the payloads of Nike Apaches 14.542 and 14.543 were taken, in the spring of 1978, to Goddard Space Flight Center (GSFC) in Greenbelt, Maryland for calibration. There they were each placed in a vacuum chamber and subjected to energetic particles of known types and energies. Figure 6.1 is a photograph of the laboratory in which the experiments took place, showing the vacuum chamber, the particle accelerator and the measurement and control electronics. The particle energy is established by adjusting the accelerating potential.

The results of these experiments are summarized in this chapter; a distinction is made between the two instruments only where significant differences in their operation were observed.

The calibration facility is under the direction of Steve Brown, whose assistance is gratefully acknowledged.

6.2 *Verification of System Operation*

In order to verify that the instrument did indeed detect energetic particles, it was placed in the vacuum chamber and subjected to a beam of energetic protons. Coaxial cables running through connectors in the sides of the chamber made possible the observation of signals at critical points within the instrument. Photographs of the signals observed at the output of the electron multiplier and at the output of the preamplifier appear in Figure 6.2. As expected, output pulses from the multiplier were larger for the higher than for the lower energy particles, and from the preamplifier were of nearly constant amplitude. The pulses proved quite adequate to drive the succeeding counter stages.

6.3 *Angular Characteristics*

The instrument was placed on its side in the chamber on a turntable as shown in Figure 6.3. Initially the entrance aperture of the analyzer was aligned directly with the incident particle beam, which entered the chamber through the circular opening on the right. The turntable was then rotated through a known angle with respect to the beam and the response of the analyzer was monitored. This procedure made possible the measurement of the angular characteristics of the instrument in the vertical plane (i.e., the plane bisecting both analyzer plates).

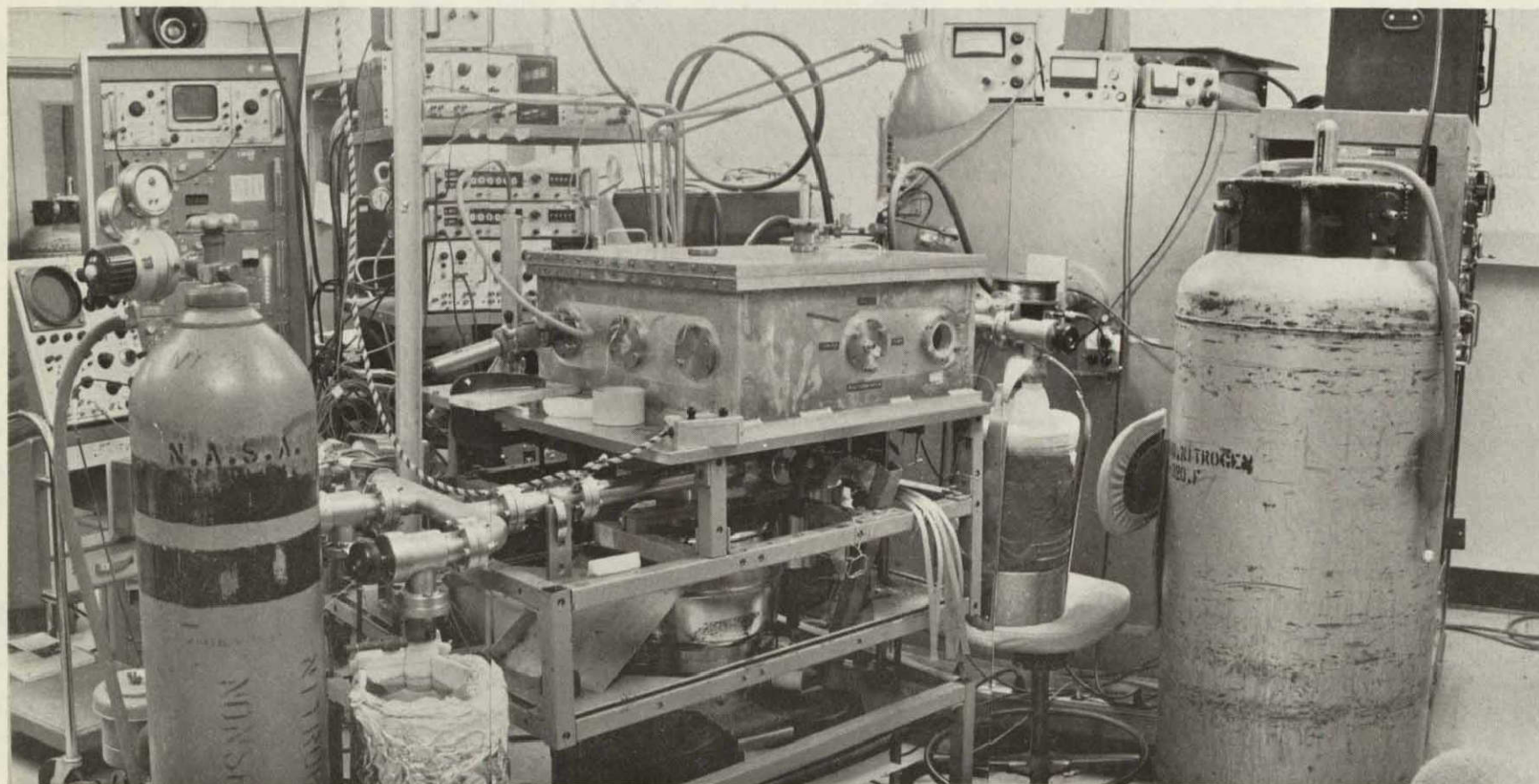
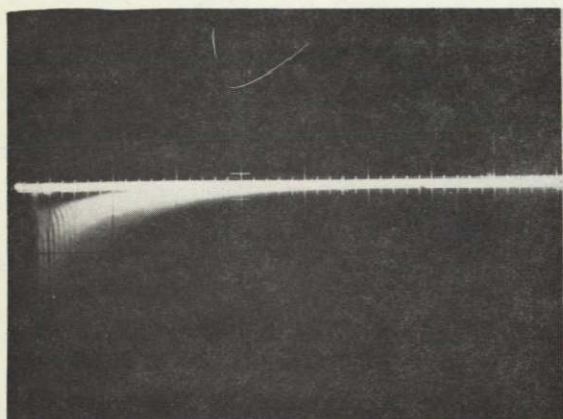
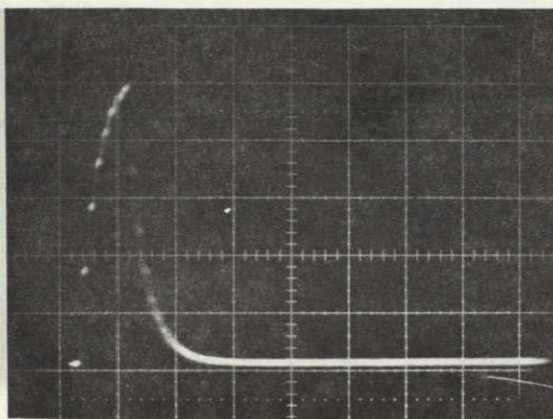


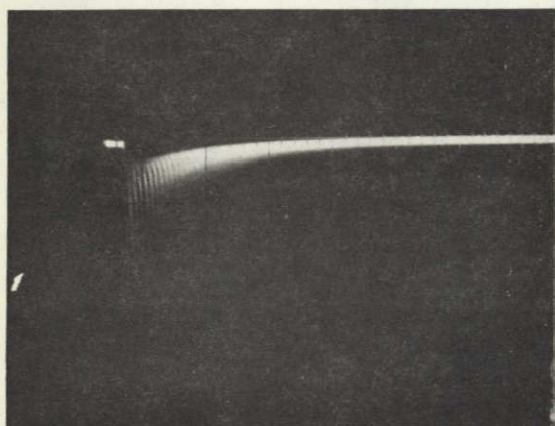
Figure 6.1 The laboratory at Goddard Space Flight Center where the calibration experiments took place.



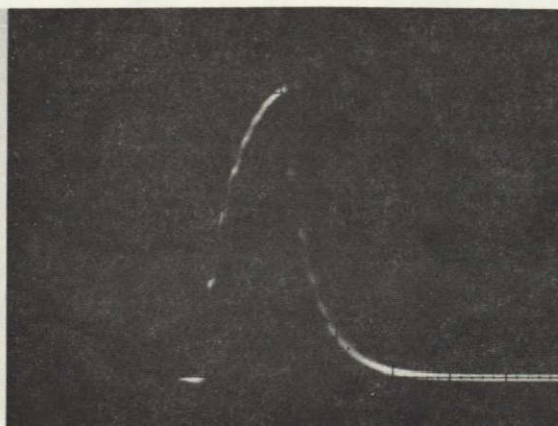
(a) Output pulses from the MM-1 for 3 keV protons; 0.05 V/cm, 0.5 μ s/cm.



(b) Output pulses from the preamp for 3 keV protons; 1 V/cm, 0.2 μ s/cm.



(c) Output pulses from the MM-1 for 10 keV protons; 0.1 V/cm, 0.5 μ s/cm.



(d) Output pulses from the preamp for 10 keV protons; 1 V/cm, 0.1 μ s/cm.

Figure 6.2 Pulse preamplifier input and output waveforms for protons of energy 3 keV [in (a) and (b)] and 10 keV [in (c) and (d)]. These photographs were taken during calibration tests at GSFC. The instrument was placed in a vacuum chamber and subjected to energetic particles from an accelerator.

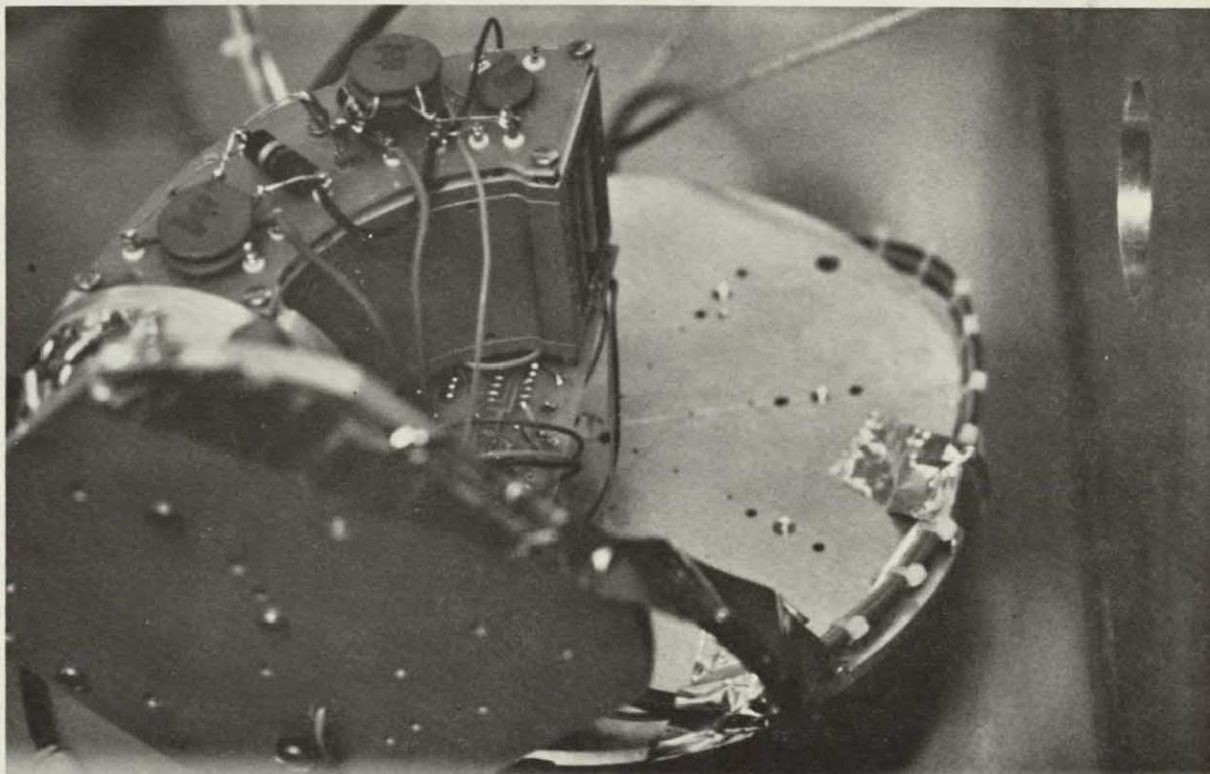


Figure 6.3 The electrostatic analyzer is shown here, without the collimator, mounted on a movable turntable inside the vacuum chamber. Visible on the right is the circular opening in the chamber wall through which energetic particles are introduced. The turntable together with the analyzer can be rotated, making possible an angular scan of the instrument's response.

The electrostatic analyzer was subjected to a beam of monoenergetic 1 keV electrons. It then was rotated on the turntable to a number of different angular positions. At each of these positions the plate voltage was varied and the count rate recorded. Plots of count rate as a function of plate voltage (recorded as the TM monitor voltage, see Section 5.1.1) are shown in Figure 6.4 at several different positions. For most cases only the peak points of the curves have been plotted; three curves are shown complete. An envelope curve through each of the peaks has also been drawn (dashed line). Positive angles correspond to a clockwise rotation of the instrument as shown in Figure 6.3. These curves show excellent agreement with those presented by *Hoffman et al.* [1973] for calibration of a satellite-borne 60° electrostatic analyzer.

These measurements of the angular characteristics of the analyzer were made without a collimator. In fact the results of these measurements were subsequently used in the design of the collimator. Note that, for 1 keV electrons, the maximum response occurs at an angle of about 7°. Therefore, when the collimator was added, it was mounted with an upward slant of exactly 7° with respect to the horizontal. The collimator can be seen mounted on the analyzer in Figure 4.8.

6.4 Energy Resolution

The energy resolution of the electrostatic analyzer with the collimator in place was investigated by subjecting the instrument to a monoenergetic beam of protons incident along the axis of the collimator. At several different particle energies, the plate voltage was varied and the count rate recorded. The data appear in Figure 6.5. There the count rate is plotted as a function of plate voltage (recorded as the TM monitor voltage) for protons of several energies.

The curve shape in each case is approximately Gaussian. The energy resolution is expressed for each energy level as the full-width at half-maximum (FWHM). (Recall from Section 4.2 that the plate voltage is directly proportional to the particle energy. This assumption will be verified shortly.)

A plot of the energy resolution as a function of incident particle energy appears in Figure 6.6. The resolution is seen to vary by a factor of three over a twenty-to-one range of energy. First-order theory indicates that the energy resolution should be independent of energy.

In Figure 6.7 the count rates of Figure 6.5 have been normalized and plotted together as a function of the plate voltage (recorded as the TM monitor

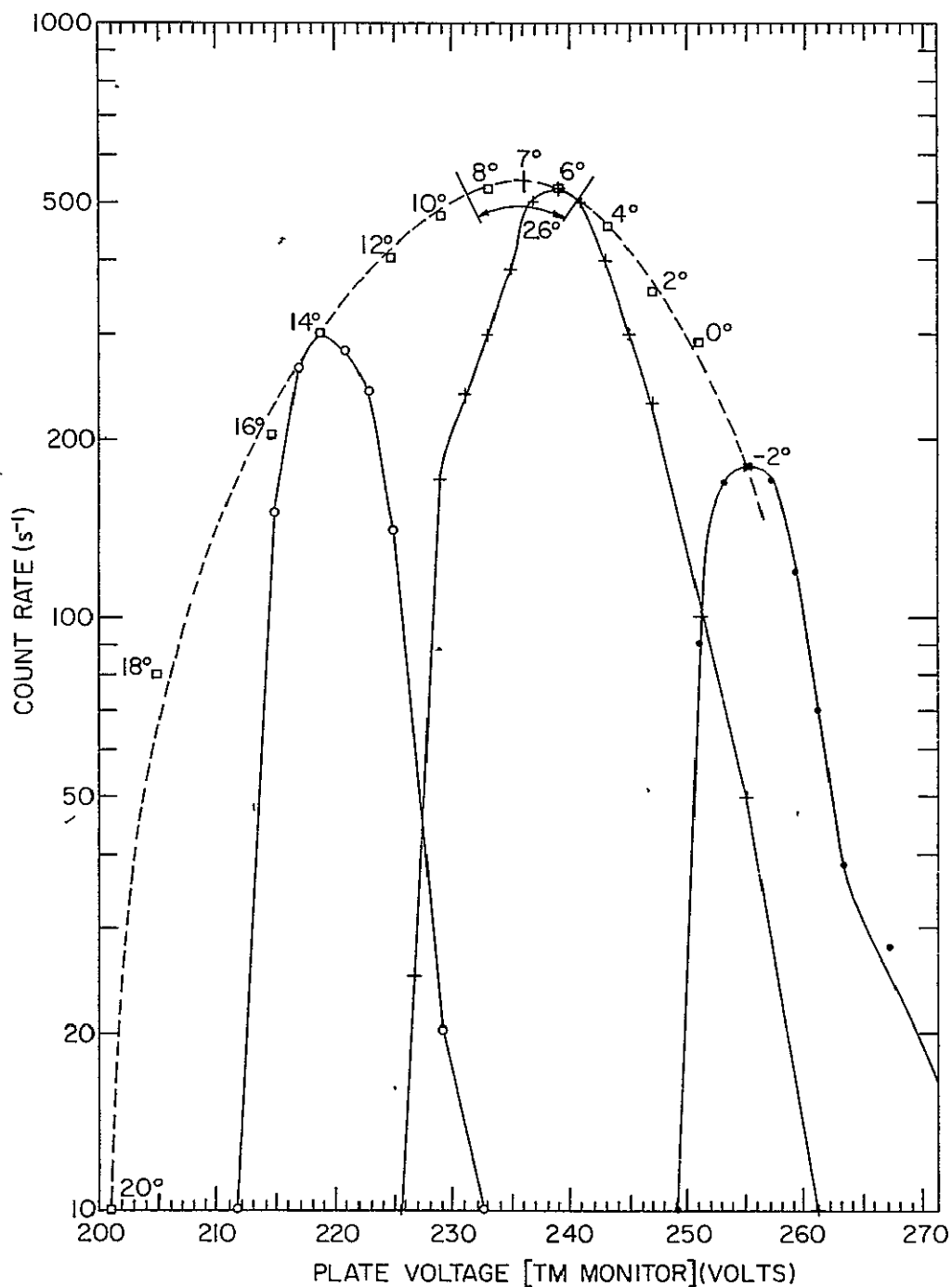


Figure 6.4 Electrostatic angular calibration using a monoenergetic 1 keV electron beam. Count rate is plotted as a function of the plate voltage monitor for several different angles of incidence. Positive angles correspond to a clockwise rotation of the instrument as shown in Figure 6.3. An envelope curve (dashed line) has been drawn through the peaks of the angular scan curves. The collimator acceptance angle is 2.6° centered about 7° .

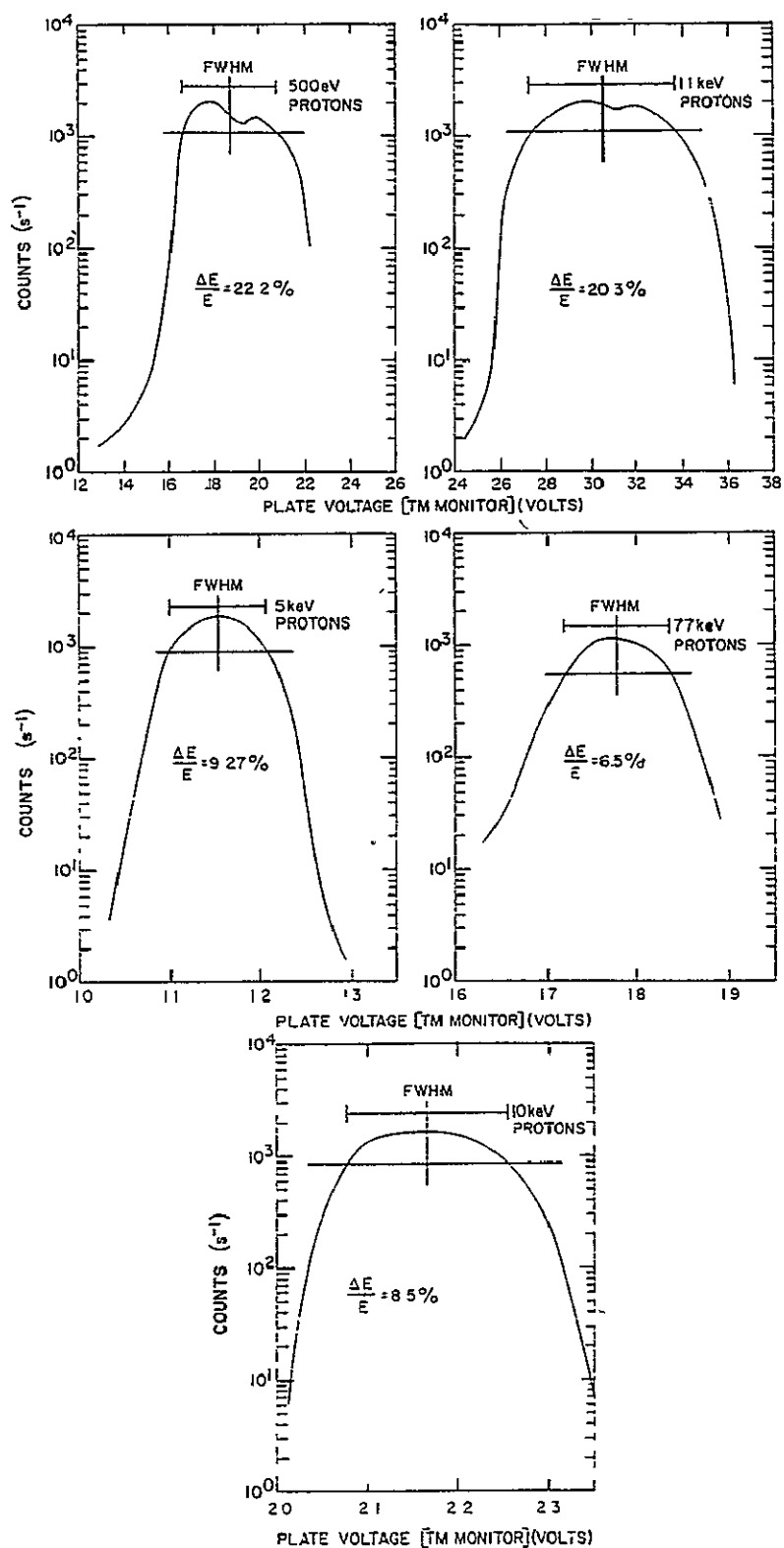


Figure 6.5 Count rates as a function of plate voltage for several different monoenergetic proton beams. In all cases, the beam was incident along the axis of the collimator (i.e., slanted 7° with respect to the analyzer plates).

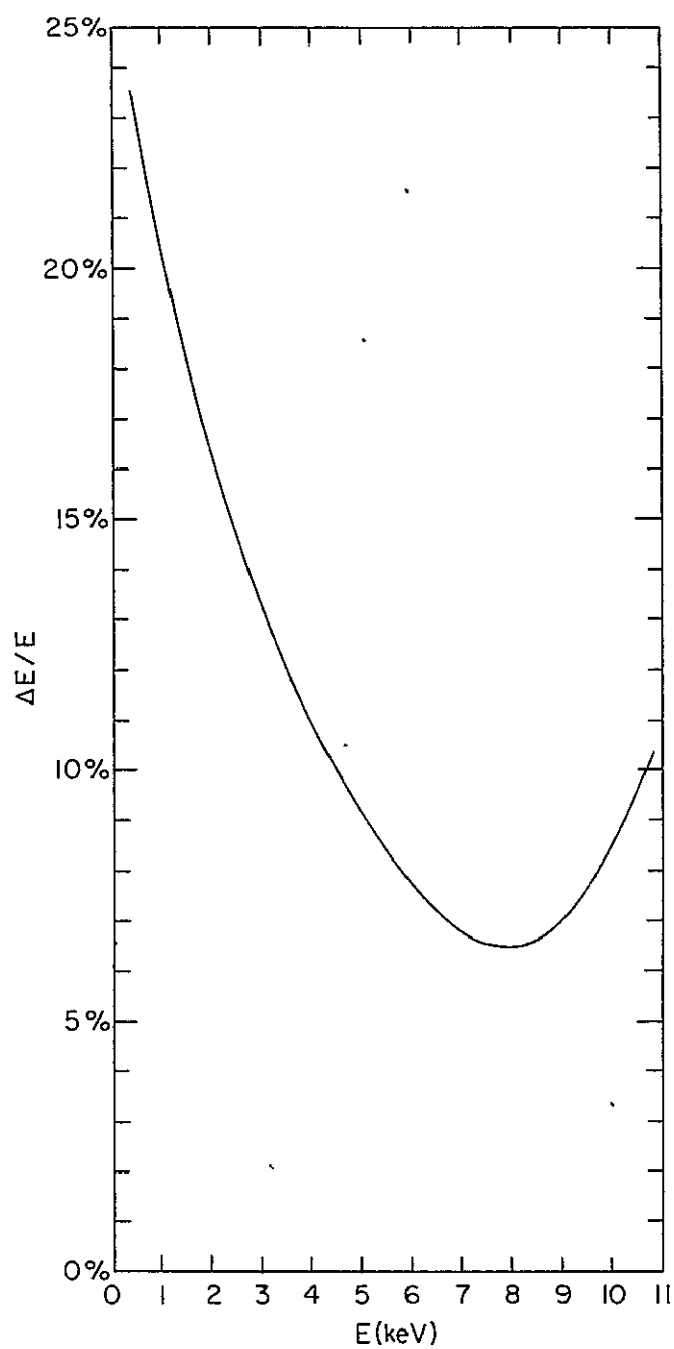


Figure 6.6 Energy resolution as a function of incident particle energy obtained from the curves of Figure 6.5.

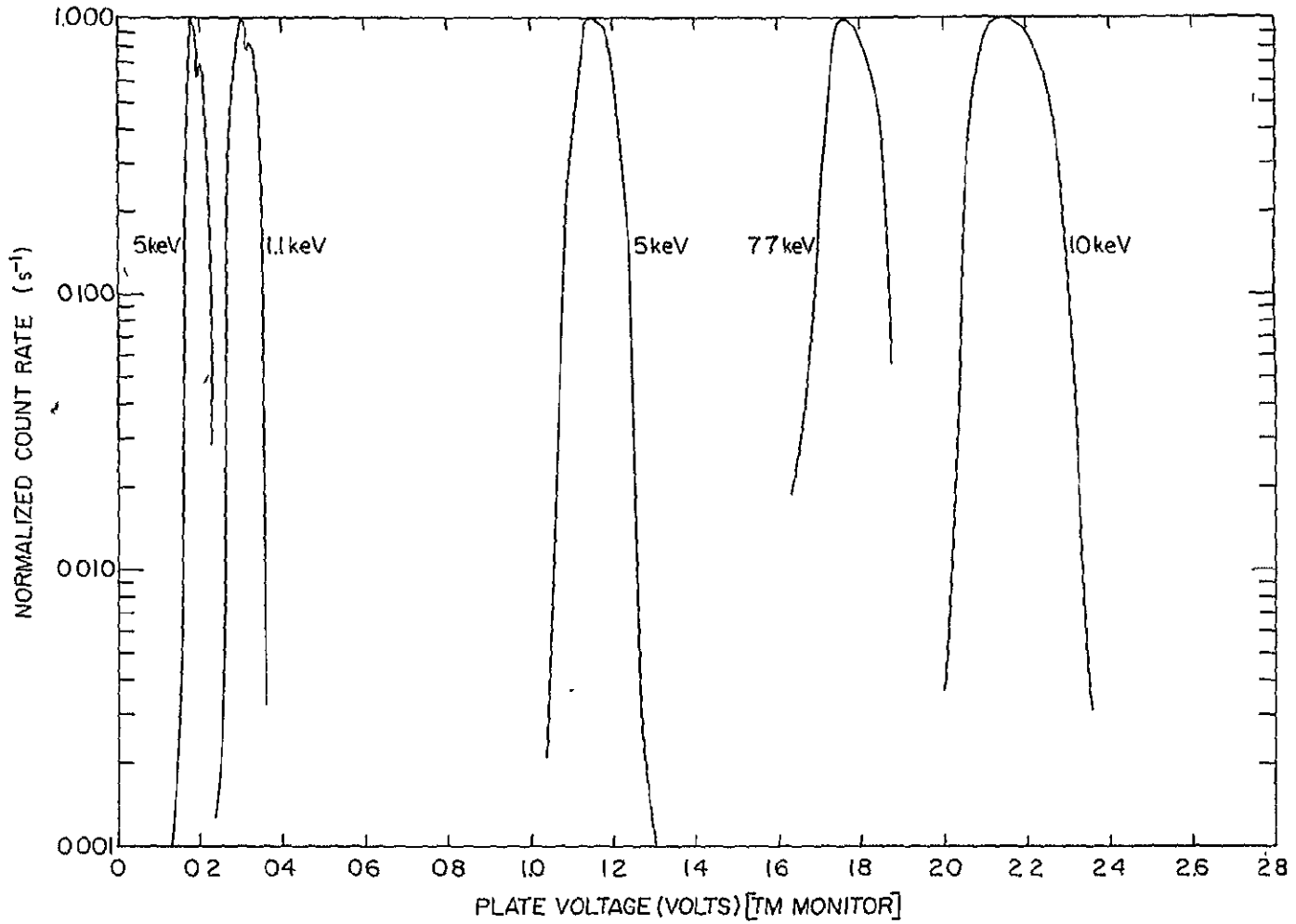


Figure 6.7 The normalized count rate is plotted as a function of plate voltage for several monoenergetic proton beams.

voltage). These curves agree well with those observed by *Frank* [1967] for an electrostatic analyzer having a central angle of 60° .

The voltages at which the peak response occurs in Figure 6.7 for each energy level are plotted as a function of particle energy in Figure 6.8. The plate voltage is found to be linearly related to the incident particle energy, as predicted in Section 4.2.

6.5 Geometrical Factor

The geometrical factor (G) of a particle detector relates the measured count rate to the actual particle flux. It is defined as

$$G = \frac{\text{count rate}}{\text{incident flux}} \quad (6.1)$$

The incident flux, assumed to be isotropic over the acceptance angle of the detector, is expressed in units of particles $\text{cm}^{-2} \text{s}^{-1} \text{sr}^{-1}$, while the count rate is in particles s^{-1} . The geometrical factor, therefore, is in units of $\text{cm}^2 \text{sr}$. It is usually calculated from the known configuration of the instrument and subsequently verified by laboratory calibration.

The geometrical factor is calculated, in the general case, by integrating the scalar product of the (vector) element of area \vec{dA} of the detector and the (vector) element of solid angle, $\vec{d\Omega}$,

$$G = \int \vec{dA} \cdot \vec{d\Omega} \quad (6.2)$$

The integral is taken over the sensitive area of the detector and over the appropriate range of solid angle.

The calculation of geometrical factor is precise for well-defined situations such as a solid-state detector with a cylindrical collimator [*Voss and Smith*, 1977]. For the electrostatic analyzer the calculation is complicated by the curved trajectories of the particles and by the effect of the fringing fields at the ends of the analyzer plates.

Johnstone [1972] has given a detailed discussion of the calculation of the geometrical factor of a cylindrical plate electrostatic analyzer. Experimental determinations by *Sanderson and Henriion* [1975] of the geometrical factor of an analyzer having a 90° central angle are found to be in good agreement with the theoretical predictions.

For some cases the integral of equation (6.2) can be simply replaced by the product $A\Omega$, where \vec{A} is the sensitive area of the detector and Ω is the

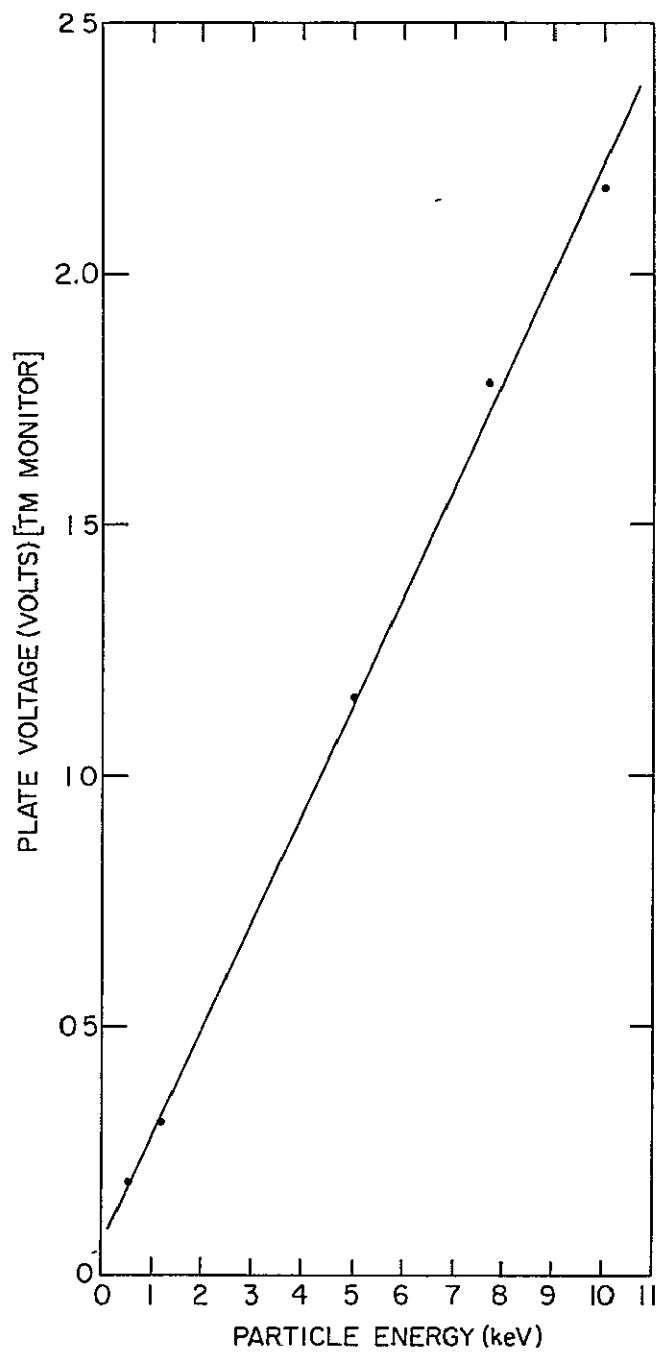


Figure 6.8 Plate voltage for peak response as a function of incident particle energy obtained from the curves of Figure 6.5.

solid angle subtended at any point in the area A . Such an approximation can be made when Ω is constant (or nearly so) over the area A and when A is perpendicular to the directions contained in Ω . Subsequent analysis of the geometrical factor of the electrostatic analyzer will be based on these assumptions. In this particular case, A will be taken as the amount of usable sensitive area of the electron multiplier and Ω as the total solid angle subtended by the analyzer plates.

The model shown in Figure 6.9 is used to simplify the calculations. As an approximation, line-of-sight trajectories are assumed for the energetic particles. Figure 6.9(a) shows the actual dimensions of the cylindrical plate analyzer, while (b) contains the dimensions of the linear model. In both cases the plates have a finite width (w).

The area of the front aperture is $0.699 \times 3.493 = 2.44 \text{ cm}^2$. The separation of front and rear apertures is 15.75 cm. Thus the solid angle subtended (at the rear aperture) by the front aperture is $2.44/(15.75)^2 = 9.84 \times 10^{-3} \text{ sr}$. The area of the rear aperture is $0.541 \times 3.493 = 1.89 \text{ cm}^2$. The geometrical factor is, therefore, $1.89 \times 9.84 \times 10^{-3} = 1.9 \times 10^{-2} \text{ cm}^2 \text{ sr}$. It should be noted that this value is based on a simple model and must be regarded as tentative pending further, more elaborate calculations and a careful evaluation of the actual calibration performed with monoenergetic beams of particles.

It is also of interest to calculate the angular response of the instrument with respect to unidirectional beams of particles. The same model, Figure 6.9(b), is used. The look angle is calculated in two orthogonal planes: the vertical plane (the plane bisecting both analyzer plates) and the horizontal plane.

Figure 6.10 shows a simplified version of the linear model used to deduce the look angle in the vertical plane. First we determine the area of the multiplier which will be illuminated by a beam of particles incident through the entrance aperture at some angle θ with respect to the collimator axis. An expression for that area (A') as a function of θ is easily derived from the geometry of Figure 6.10. The result is, for both positive and negative values of θ :

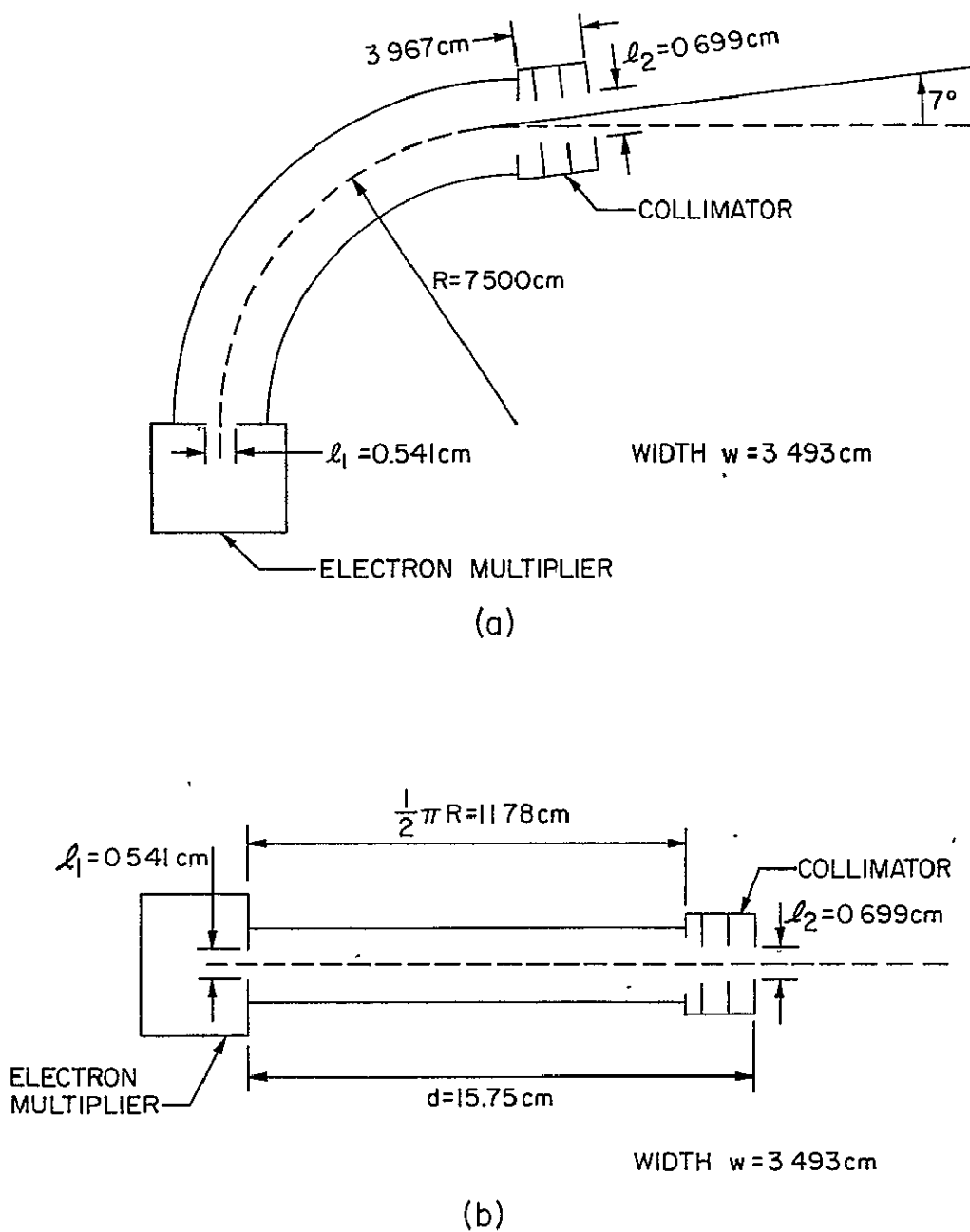


Figure 6.9 A linear approximation to the cylindrical plate electrostatic analyzer. The actual instrument is shown in (a). Shown in (b) is the approximation, used in the calculation of the geometrical factor.

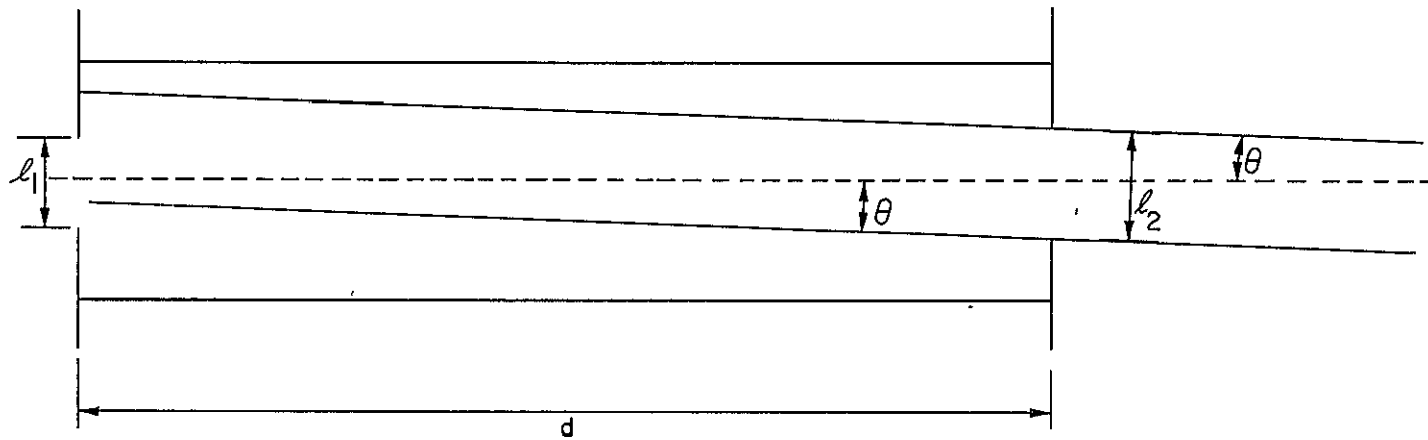


Figure 6.10 The geometry used in the calculation of the solid look-angle. The actual dimensions are those of Figure 6.9(b).

$$\left. \begin{aligned}
 A' &= l_1 w && \text{for } d|\tan\theta| \leq \frac{l_2 - l_1}{2} \\
 A' &= \left[\frac{l_1 + l_2}{2} - d|\tan\theta| \right] w && \text{for } \frac{l_2 - l_1}{2} \leq d|\tan\theta| \leq \frac{l_1 + l_2}{2} \\
 A' &= 0 && \text{for } d|\tan\theta| \geq \frac{l_1 + l_2}{2}
 \end{aligned} \right\} (6.3)$$

This same procedure, when applied to a scan of the particle beam in the horizontal plane, yields:

$$A' = l_1 [w - d|\tan\theta|] \quad (6.4)$$

The quantity A' represents the area of the entrance aperture which is projected onto the exit aperture by the beam of particles. This area, normalized to its maximum value $l_1 w$, is plotted in Figure 6.11 as a function of the angle of incidence θ , for scans of the particle beam in both the vertical and horizontal planes. The maximum value of A' corresponds to full illumination of the exit aperture, which, because of the geometry of the instrument (i.e., $l_2 > l_1$), occurs over a small range of angles in a vertical scan but only at $\theta = 0^\circ$ for a horizontal scan.

The look angle in each of the orthogonal planes is expressed in Figure 6.11 as the full-width at half-maximum. From Figure 6.11(a) the angle (α) in the vertical plane is 2.6° . In the horizontal plane, from Figure 6.11(b), the angle (β) is 12.6° . The geometrical factor can also be derived from these two angles.

Knowledge of the angles in both the vertical and horizontal planes makes possible a calculation of the total solid angle of the instrument, as indicated in Figure 6.12. The formula used, which follows from the definition of solid angle, for sufficiently small values of α and β , is

$$\Omega = \alpha\beta \quad (6.5)$$

where α and β are in radians and Ω is in steradians. Application of equation (6.5) to the linear model above yields, as before,

$$\Omega = 1.0 \times 10^{-2} \text{ sr} \quad (6.6)$$

Although equation (6.5) is an approximate relation, for the small angles α and β involved here the error is negligible.

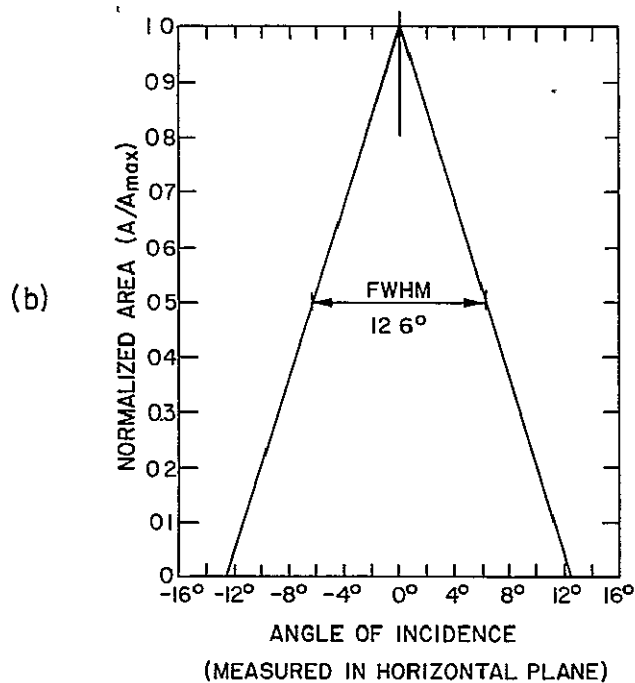
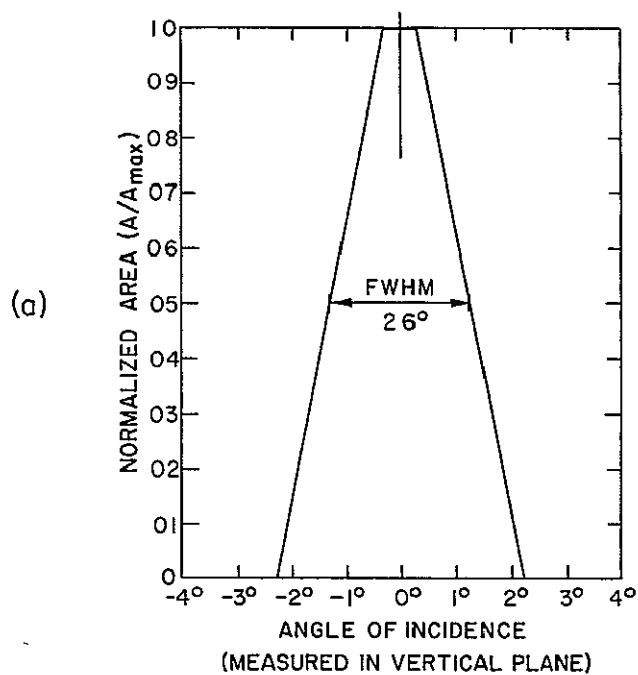


Figure 6.11 Plots of the normalized multiplier (exit aperture) area illuminated by a beam of particles incident through the collimator (entrance aperture) at an angle θ measured with respect to the collimator axis. (a) is a scan in the vertical plane (the bisecting both analyzer plates) and (b) is a scan in the horizontal plane.

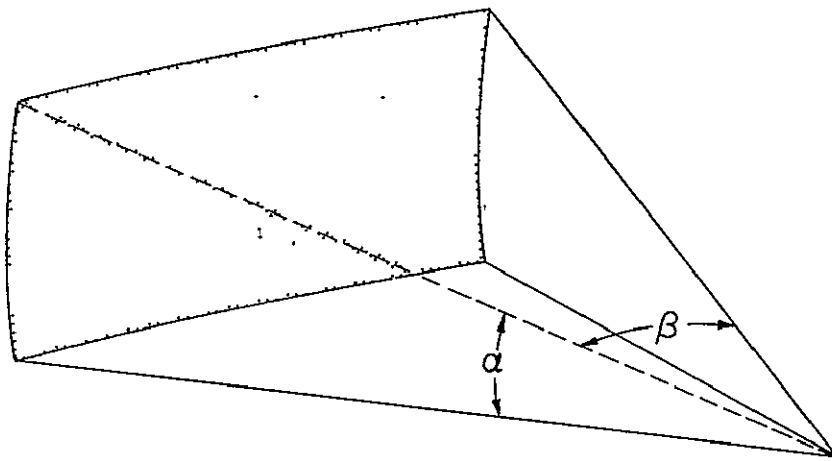


Figure 6.12 Illustrated is the calculation of the solid angle Ω subtended by the orthogonal angles α and β . For sufficiently small values of α and β : $\Omega = \alpha\beta$, where α and β are in radians and Ω is in steradians.

The second factor needed in the calculation of the geometrical factor is the sensitive area of the electron multiplier. Since the MM-1 is a large area multiplier, the sensitive area for this instrument is determined by the area of the exit aperture, Figure 6.9, which is:

$$A = L_1 w = 1.89 \text{ cm}^2 \quad (6.7)$$

The geometrical factor, finally, is the product of the total solid angle of the instrument and the sensitive area of the multiplier,

$$G = A\Omega = 1.9 \times 10^{-2} \text{ cm}^2 \text{ sr} \quad (6.8)$$

6.6 Pulse-Height Distributions

The final calibration experiment performed was to feed output pulses from the electron multiplier to a laboratory pulse-height analyzer. Several different particle types were introduced to the electrostatic analyzer, including H^+ , He^+ , H_2^+ , O^+ and N^+ . Each was adjusted for the same energy (11 keV) and the same count rate (2000 s^{-1}). Pulses were collected and analyzed over an equal time period for each of the particle types. The results are displayed in Figure 6.13. Shown there is a plot of the count rate as a function of pulse height over approximately 150 channels of the pulse-height analyzer. Pulse-height distributions were recorded for H^+ , He^+ , H_2^+ and O^+ ; the distribution for N^+ is identical with that for O^+ and is not included in the figure. The analyzer plate voltage was in each case adjusted for maximum detector response. The bias to the MM-1 electron multiplier was about 3 kV.

The pulse-height distributions of Figure 6.13 all appear to be exponential, but each with a different decay constant. An integration of count rate performed from some threshold pulse-height level out to infinity would yield different total fluxes for different particle types. Thus a pulse-height analysis of the electron multiplier output makes possible the identification of the various types of particles. This pulse-height analysis is performed in the rocket payload as described in Section 5.5.

Figure 6.14 repeats the data of Figure 6.13 for H^+ and O^+ ions, this time plotted using a logarithmic vertical scale to represent the count rate. The pulse-height distributions now appear to be linear, confirming the fact that the distributions of Figure 6.13 are indeed exponential. Particle types can be identified from this logarithmic plot on the basis of the slope of the pulse-height distributions. Pulse-height data obtained from the experiment

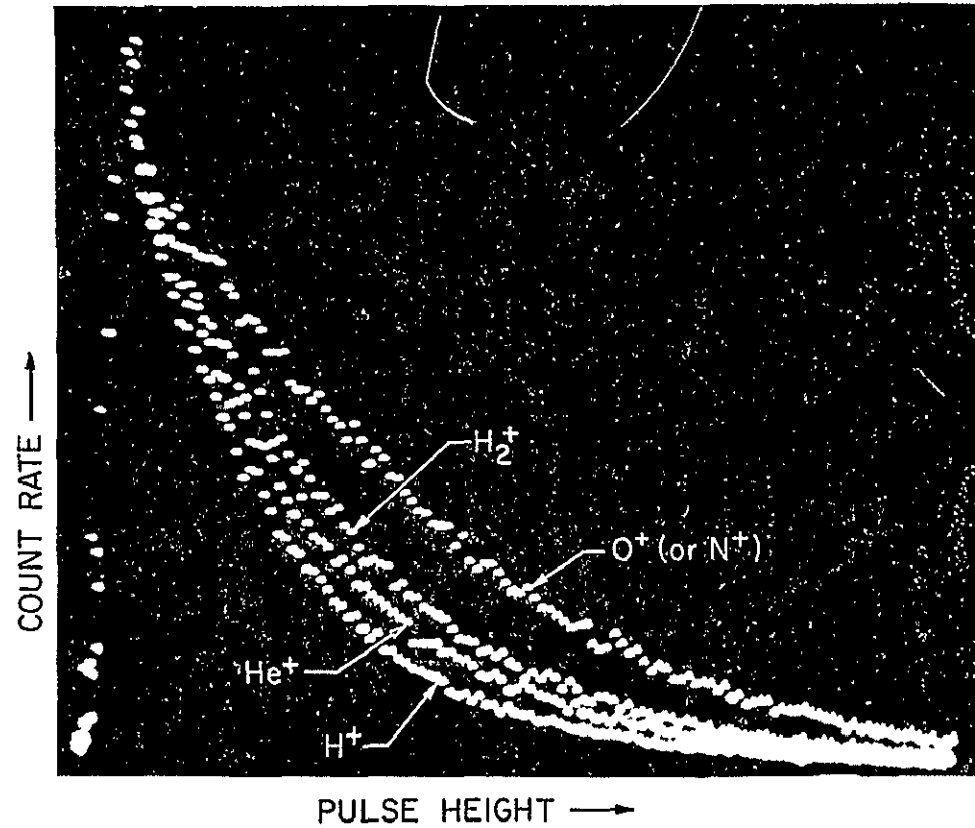


Figure 6.13 Count rate as a function of pulse height for several different particle types. Data were taken over an equal time period for each type, and each was adjusted to the same energy (11 keV) and flux (2000 s^{-1}) levels. Both the vertical and horizontal scales are linear.

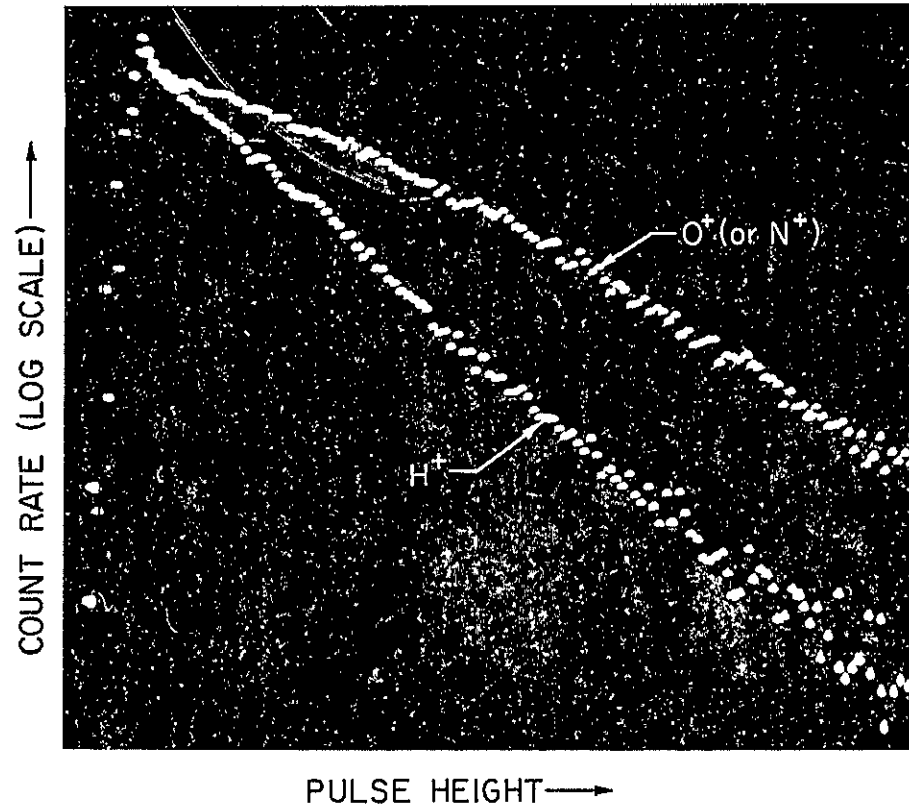


Figure 6.14 Count rate plotted on a log scale as a function of pulse height for H^+ and O^+ ions. These data are taken from Figure 6.13.

during flight need only be plotted in a logarithmic fashion and the slopes compared with those in Figure 6.14 to enable an identification of energetic particle types.

7. SUMMARY, FLIGHT PERFORMANCE AND RECOMMENDATIONS FOR FUTURE WORK

7.1 *Summary*

This report has presented the design and calibration of a rocket-borne low-energy particle spectrometer. The instrument chosen, an electrostatic analyzer, was designed and built to be flown as part of an international intercalibration project: the JASPIC program. The experiment has as its major objective the measurement of 0.5 to 12 keV particle flux in the nighttime midlatitude E region.

Previous observations of energetic particle flux in this region have been outlined. An argument has been presented demonstrating the existence of a nighttime corpuscular ionization source. A lack of data from previous experiments concerning the low energy portion of the energetic particle spectrum has provided impetus for the present instrument development.

A complete description of the design and construction of the electrostatic analyzer has been presented, constituting the major portion of this report. In addition, a full description has been provided of a number of pre-flight calibration tests which were performed on the instrument. The results of these tests, contained in Chapter 6, clearly demonstrate the more-than-adequate performance of the device.

7.2 *Flight Performance*

Nike Apache 14.543, which included the electrostatic analyzer in its payload, was launched from Wallops Island at 2315 EST on the night of 19 June 1978. Preliminary data from the flight indicate that all systems functioned well. The magnetic activity for that night was low, with the three-hour planetary magnetic index $K_p = 3-$. The energetic particle spectrum, as observed by the solid-state detectors, exhibited a power law spectral index of -1.5 . Such a hard spectrum yielded very small count rates, especially at the lower energy levels. For energies $E > 15$ keV the integral flux measured with the solid-state detectors did not exceed 24 counts s^{-1} ($\sim 400 \text{ counts cm}^{-2} \text{ s}^{-1} \text{ ster}^{-1}$ at 90° pitch angle). The approximate energy flux ($E > 2$ keV) for this spectrum is $10^{-4} \text{ ergs cm}^{-2} \text{ s}^{-1} \text{ ster}^{-1}$. Count rates recorded by the electrostatic analyzer were also quite low, of the order of 3 counts s^{-1} .

Of major significance in these preliminary results is the fact that the electrostatic analyzer did function as designed in an actual rocket flight.

All systems of the instrument performed satisfactorily. Preliminary analysis of the data indicates that background UV radiation did not seriously limit the threshold of the analyzer, a problem often encountered with these instruments. In addition, in the region of overlap in energy range, count rates recorded by the electrostatic analyzer show agreement with those recorded by the solid-state detectors.

The only significant irregularity encountered with the payload of Nike Apache 14.543 was a series of transient voltage pulses which started at 107 seconds after launch at an altitude of 133 km. Although several payload experiments were affected by the pulses, in no case did they prevent useable data from being obtained. Their effect on the electrostatic analyzer was to cause erratic sequencing of the plate voltage sweep circuit, and hence an irregular plate voltage waveform. The origin of the transient pulses is presently being investigated.

Due to the low geomagnetic activity in June 1978, the second rocket, Nike Apache 14.542, was not launched with the JASPIC program. This launch has been tentatively rescheduled for later in 1978, pending sufficient magnetic activity.

Overall, the JASPIC project has been a success. The project duration was from 3 June to 25 June 1978. During that time a total of eight sounding rockets were launched into various degrees of magnetic activity. Table 7.1 is a summary of the times and conditions of each of the eight launches. These launches together with the additional ground- and air-based observations provided a successful intercomparison of the various experiments. Preliminary data from the several experiments indicate that the direct, simultaneous measurements of soft energetic particle fluxes at nighttime agree with each other to within a factor of from three to ten, when the particle pitch-angle distribution is taken into account. Preliminary conclusions can be made which point to the differing geographic and geomagnetic conditions as the primary cause for the apparent discrepancies of previous observations reported in the literature. A final data evaluation report on the JASPIC program is to be completed by the fall of 1979.

7.3 Recommendations for Future Work

A major constraint on the development of the electrostatic analyzer which has not yet been mentioned has been that of time. The entire development from the initial conception to the first rocket launch covered a span of less than

Table 7.1

Listed are the dates, times and geomagnetic conditions for each of the eight sounding rockets launched as part of the JASPIC program. The duration of the program was from 3 June to 25 June 1978. K_{FR} is measured at Fredericksburg, Virginia; K_p is the planetary index.

Rocket	Date (UT)	Time (UT)	Magnetic Conditions	
			K_{FR}	K_p
Soviet MR-12	11 June 1978	0627	4	5-
Nike Apache 14.539		0632		
Soviet MR-12	20 June 1978	0410	3	3-
Nike Apache 14.543		0415		
Soviet MR-12	24 June 1978	0213	5	5-
Soviet MR-12	26 June 1978	0131	4	4
Nike Tomahawk 18.1019		0208		
Soviet MR-12		0231		

10 months. As a result, some of the finer points in the design may have been overlooked, and a number of calibration tests which might have been desirable have been omitted. However, the successful performance of the first unit in flight shows that the design is satisfactory and the calibration adequate.

Design changes which took place during the development of the plate voltage sweep circuits (Section 5.1) have, due to the time restraints, not yet been reflected in the layout of the printed circuit card for those circuits. The PC cards used on the two instruments built were adapted through the use of jumper wires. A new PC card layout is needed for any future instruments.

High-voltage arcing somewhere within the analyzer plate voltage supply system is a possible cause of the transient pulses which were observed in several places within the payload. As a precaution, a re-evaluation of the physical and electrical construction of the high-voltage circuitry is recommended in an effort to eliminate any possibility of arcing. In any case, a modification to the plate voltage sweep circuit to make it less vulnerable to such transients would be advisable.

The Tecnetics converter used in the electron multiplier high-voltage power supply was found to be quite noisy, even with the additional filtering and magnetic shield which were provided. Redesign of this power supply might serve to lower the threshold and increase the sensitivity of the instrument.

The sensitivity of the analyzer to UV radiation might be further decreased by using a different finish on the interior surfaces of the plates. *Balsiger et al.* [1976] have evaluated several different finishes, including chemically deposited copper sulfide black and electrochemically deposited platinum black, and have considered other methods of reducing scattering in an electrostatic analyzer. Sandblasting of the plate surfaces has also been suggested [*Hoffman et al.*, 1973].

This report has introduced a new instrument valuable to sounding rocket experimenters interested in the measurement of nighttime energetic particle precipitation. Satisfactory performance of the electrostatic analyzer has been clearly demonstrated both in the laboratory and as part of a sounding rocket payload. This experience earns for the analyzer a place among the list of proven rocket-borne experiments. Future use of the electrostatic analyzer for direct measurements of nighttime energetic particle precipitation is highly recommended.

REFERENCES

- Balsiger, H., P. Eberhardt, J. Geiss, A. Ghielmetti, H. P. Walker, and D. T. Young [1976], A satellite-borne ion mass spectrometer for the energy range 0 to 16 keV, *Space Sci. Instrum.*, *2*, 499-521.
- Davis, L. L., L. G. Smith, and H. D. Voss [1979], A rocket-borne data-manipulation experiment using a microprocessor, *Aeron. Rep. No. 84*, Aeron. Lab., Dep. Elec. Eng., Univ. Ill., Urbana.
- Frank, L. A. [1967], Initial observations of low-energy electrons in the earth's magnetosphere with OGO 3, *J. Geophys. Res.*, *72*, 185-195.
- Geller, M. A., L. G. Smith, and H. D. Voss [1975], Analysis of nighttime E-region winds and ionization production, *Radio Sci.*, *10*, 335-345.
- Gough, M. P., and H. L. Collin [1973], Energetic electron precipitation as a source of ionization in the nighttime D region over the midlatitude rocket range, South Uist, *J. Atmos. Terr. Phys.*, *35*, 835-850.
- Hayakawa, S., T. Kato, T. Kohno, T. Murakami, F. Nagase, K. Nishimura, and Y. Tanaka [1973], Existence of geomagnetically trapped electrons at altitudes below the inner radiation belt, *J. Geophys. Res.*, *78*, 2341-2343.
- Hoffman, R. A., J. L. Burch, R. W. Janetzke, J. F. McChesney, S. Y. Way, and D. S. Evans [1973], Low-energy electron experiment for Atmosphere Explorer-C and D, *Radio Sci.*, *8*, 393-400.
- Hughes, A. L., and V. Rojansky [1929], On the analysis of electronic velocities by electrostatic means, *Phys. Rev.*, *34*, 284-290.
- Johnstone, A. D. [1972], The geometrical factor of a cylindrical plate electrostatic analyzer, *Rev. Sci. Instrum.*, *43*, 1030-1040.
- Leung, W., L. G. Smith, and H. D. Voss [1979], A rocket-borne pulse-height analyzer for energetic particle measurements, *Aeron. Rep. No. 83*, Aeron. Lab., Dep. Elec. Eng., Univ. Ill., Urbana.
- Meier, R. R., and P. Mange [1973], Spatial and temporal variations of the Lyman-alpha airglow and related atomic hydrogen distributions, *Planet. Space Sci.*, *21*, 309-327.
- Miller, K. L., and L. G. Smith [1978], Incoherent-scatter radar observations of irregular structure in midlatitude sporadic-E layers, *J. Geophys. Res.*, *83*, 3761-3775.
- Paarmann, L. D., and L. G. Smith [1977], A rocket-borne airglow photometer, *Aeron. Rep. No. 77*, Aeron. Lab., Dep. Elec. Eng., Univ. Ill., Urbana.

- Sanderson, T. R., and J. Henrion [1975], Measurement of the geometrical factor of an electrostatic analyzer-channeltron detector, *Space Sci. Instrum.*, *1*, 351-361.
- Seward, F. D. [1973], The geographical distribution of μ keV electrons above the earth's atmosphere, *Rep. UCRL-51456*, Univ. California, Lawrence Livermore Lab., Livermore.
- Smith, L. G., M. A. Geller, and H. D. Voss [1974], Energetic electrons in the midlatitude nighttime E region, *J. Atmos. Terr. Phys.*, *36*, 1601-1612.
- Strobel, D. F., T. R. Young, R. R. Meier, T. P. Coffey, and A. W. Ali [1974], The nighttime lower ionosphere, *J. Geophys. Res.*, *79*, 3171-3178.
- Voss, H. D., and L. G. Smith [1974], Design and calibration of a rocket-borne electron spectrometer for investigation of particle ionization in the nighttime midlatitude E region, *Aeron. Rep. No. 62*, Aeron. Lab., Dep. Elec. Eng., Univ. Ill., Urbana.
- Voss, H. D., and L. G. Smith [1977], Energetic particles and ionization in the nighttime middle and low latitude ionosphere, *Aeron. Rep. No. 78*, Aeron. Lab., Dep. Elec. Eng., Univ. Ill., Urbana.
- Voss, H. D., and L. G. Smith [1979], Nighttime ionization by energetic particles at Wallops Island in the altitude region 120 to 200 km, *Geophys. Res. Lett.*, February.